Abstract

Molecular Mechanism of Assembly and Secretion of *Geobacter sulfurreducens* Pili and Cytochrome Nanowires for Extracellular Electron Transport

Aldo Ivan Salazar Morales

2023

Type 4 pili (T4P) have been described canonically as appendages capable of providing motility and adhesion to Gram-negative bacteria. However, the environmentally important soil bacteria *Geobacter sulfurreducens* (*Gs*) was proposed to use these filaments as "nanowires" to transfer electrons extracellularly. *Gs* assembles nanowires to meet their metabolic needs by transferring electrons generated in the cytosol to these nanowires to a final electron acceptor through a series of proteins and complexes. This discovery brought a lot of attention to the microbe in an attempt to understand the mechanism and pathway through which *Gs* conducts extracellular electron transfer (EET). Several genetic studies suggested that *Gs* pili were responsible for EET as *pilA-N* mutants showed impaired iron reduction and current production. Our work demonstrated that *Gs* pili are required for the secretion of cytochrome OmcS and OmcZ nanowires that are essential for iron reduction and current production, respectively. This new knowledge questioned the long-standing dogma of the field where *Gs* assemble PilA filaments to transfer electrons and not the nanowire-forming cytochromes OmcS and OmcZ. Therefore, this thesis aimed to carefully

study the physiological role of PilA filaments in EET and reinterpret two decades of prior work.

To better understand the role of PilA filaments in EET we used a combination of cryo-EM and functional assays to characterize PilA filaments. Our work shows that PilA filaments are composed of PilA-N and PilA-C that forms a heterodimer to assemble a filament akin to Type 2 Secretion System (T2SS) endopili (previously called pseudopili) rather than a T4P. Our functional assays showed that *Gs* pili did not exhibit canonical T4P or nanowire behavior, but rather a secretory role for both OmcS and OmcZ nanowires.

Further in-depth analysis of *pilA-N* mutants, where this sequence was altered or replaced by other heterologous sequences, showed a deficiency in iron reduction and current production. Through genetic analysis and biophysical approaches, we were able to demonstrate that the complementation of native *pilA-N* in a *pilA* mutant restores both iron reduction and current production. Our novel approach using Graphene Oxide (GO) and electrostatic force microscopy (EFM) clearly shows at a single-cell level that *Gs* utilizes OmcS nanowires for iron reduction and OmcZ nanowires for current production. Furthermore, *in silico* experiments showed that a theoretical PilA-N filament would be highly unstable and that the presence of PilA-C stabilizes the structure of the filament. These results help to reinterpret close to twenty years of work where alterations to *pilA-N* showed deficiencies in iron reduction and current production. Our studies explain previously observed phenotypes that mischaracterized the role of PilA filaments as a nanowire.

Our work also demonstrates that OmcS heme coordination is essential for nanowire biogenesis and EET. Our $OmcS^{H16A}$ mutant showed that disruption of inter-subunit heme coordination inhibits OmcS nanowire assembly and iron reduction. A better understanding of nanowire assembly will allow for rational engineering of synthetic complexes and tunability to design biomaterials.

In summary, this thesis work has demonstrated the secretory role of PilA filaments in EET. This improved understanding will guide further studies to identify and characterize other components involved in the secretion and assembly of both PilA filaments and nanowires. This would allow us to express the minimal components required to create a chassis for nanowire biogenesis. The assembly of the minimal components in the genetically tractable *E. coli* should also eliminate the need to limit studies to *Gs* which has a long doubling time and requieres anaerobic growing conditions.

Molecular Mechanism of Assembly and Secretion of *Geobacter sulfurreducens* Pili and Cytochrome Nanowires for Extracellular Electron Transport

A Dissertation

Presented to the Faculty of the Graduate School

of

Yale University

In Candidacy for the Degree of

Doctor of Philosophy

by

Aldo Ivan Salazar Morales

Dissertation Director: Nikhil S. Malvankar

May 2023

Table of Contents

Acknowledgements

I would like to express my sincere gratitude to the individuals who have supported and encouraged me throughout my dissertation journey:

First and foremost, I want to thank my dissertation advisor, Nikhil Malvankar, for his guidance, mentorship, and expertise. His constant support and constructive feedback have been invaluable in guiding me through my research and shaping me as a scientist.

I also want to extend my appreciation to my committee members, Yong Xiong and Wei Mi, for their insightful comments, suggestions, and advice, which have helped me improve the quality of my work and navigate through Graduate School.

I am grateful to the members of the Malvankar Lab, both past and present, who have supported me during these past years. I would like to specially thank Catharine Shipps and Cong Shen for their encouragement, support, and stimulating discussions, which have broadened my horizons and enriched my research and personal life. Additionally, I am thankful to our wonderful technicians, Jackie Mendes and Aiwei Sui, for all the help they provided over the years to facilitate all of the experiments presented in this work.

I would also like to extend my sincere thanks to the wonderful friends I made along the way: Chloe Emerson, Cathy García, Cecelia Harold, Kira Marshall, and Nancy Sánchez. You have been a constant source of encouragement and motivation throughout my academic and personal journey, and I am indebted to you for your love and support.

Finalmente, quisiera agradecer a mi familia, en especial a mis padres José Manuel Salazar Romero y Olivia Morales Zaragoza; mi hermana Kimberly Itzel Salazar Morales; y a mis abuelos Andrés Morales Ordaz y Olivia Zaragoza Díaz; sin su apoyo y motivación nada de esto hubiese sido possible.

Abbreviations

AFM	atomic force microscopy
Aro5	*G. sulfurreducens* strains containing the following mutations in *pilA-N*: F24A, Y27A, Y32A, F51A, Y57.
aMD	accelerated molecular dynamics
A26	truncated *pilA-N* at residue Ala 26.
BCA	bicinchoninic acid
CD	circular dichroism
cryo-EM	cryogenic electron microscopy
CTF	contrast transfer function
DIET	direct interspecies electron transfer
DNA	deoxyribonucleic acid
EET	extracellular electron transfer
EFM	electrostatic force microscopy
EPR	electric paramagnetic resonance
ETA	ethanolamine
FSC	Fourier shell correlation
FT	Fourier transform
GO	graphene oxide
Gs	*Geobacter sulfurreducens*
Gs-Pa	*G. sulfurreducens* strains in which *pilA-N* was replaced by *pilA* from *P. aeruginosa.*
Gs-Gu	*G. sulfurreducens* strains in which *pilA-N* was replaced by *pilA* from *G. uraniireducens.*
HALS	highly anisotropic low spin
HS	high spin
HIV	human immunodeficiency virus
IIET	indirect interspecies electron transfer
IM	inner membrane
I-V	current-voltage
LB	Lysogeny Broth
LC-MS/MS	liquid chromatography with tandem mass spectrometry
L16	truncated *pilA-N* at residue Leu 16.
MD	molecular dynamics
MIET	mediated interspecies electron transfer
MM-GBSA	molecular mechanics generalized Born solvation area
NBAF	NB media with Acetate and Fumarate as electron donor and acceptor respectively.
(m)RNA	(messenger) ribonucleic acid

OM	outer membrane
OmcS/OmcZ	outer membrane cytochrome S/Z
PP	periplasm
RMSD	root mean square deviation
RSCC	real-space correlation coefficient
RT-(q)PCR	reverse transcription-(quantitative) polymerase chain reaction
SDS(-PAGE)	sodium dodecyl sulfate(-polyacrylamide gel electrophoresis)
S37	truncated *pilA-N* at residue Ser 37.
SHE	standard hydrogen electrode
T2SS	type II secretion system
T4P	type IV pili
TEM	transmission electron microscopy
Trp	*G. sulfurreducens* strains containing the following mutations in *pilA-N*: F51W, Y57W.
UV-vis	UV-visible
WT	wild-type
XAS	X-ray absorption spectroscopy

List of Figures and Tables

Figures

Main Tables

Equations

1. Introduction

1.1 Role of Extracellular Electron Transfer in Biogeochemical Cycles

Life on our planet is a remarkable testament to the ingenuity and adaptability of living organisms. From the frigid depths of the Arctic to the scorching sands of the Sahara, life has found ways to survive in conditions that would be inhospitable to most humans. One domain of life that exemplifies this resilience is the bacteria, which have evolved a wide range of mechanisms to thrive in diverse environments. A key aspect of bacterial diversity is cellular respiration, the process by which living organisms produce ATP to power all metabolic functions. Through a series of redox reactions, electrons are transferred from an electron donor to an electron acceptor, generating ATP as a result[1].

Bacteria can use a variety of electron acceptors depending on the availability of oxygen in their environment. In aerobic respiration, oxygen serves as the final electron acceptor, leading to the most efficient production of ATP . The respiratory chain of bacteria is composed of several protein complexes, including NADH dehydrogenase, succinate dehydrogenase, cytochrome c oxidase, and ATP synthase, which work together to transport electrons from the substrate to oxygen[1,2]. This generates a proton motive force that drives the synthesis of ATP, the primary source of energy for the organism. In contrast, in anaerobic respiration, bacteria use alternative electron acceptors such as nitrate, sulfate, and metal oxides, resulting in a lower yield of ATP[1,2]. Despite this, anaerobic respiration is a crucial process for many bacteria that live in oxygen-deprived environments.

Bacteria not only can utilize a wide array of substrates to increase biodiversity, but this versatility also drives alterations in the geosphere and shape ecological niches[2]. This diversity provides organisms with the means to utilize substrates and metabolize them into compounds that are usable for other organisms. The wide variety of metabolites in nature creates electrochemical gradients that facilitate extracellular electron transfer (EET), as well as genetic regulation to facilitate the utilization of high energy sources and molecules with a high redox potential to donate their electrons[1,2]. During EET intracellularly-generated electrons are transported by a series of molecules from the cytosol through the cellular membrane into the extracellular space. This process is crucial for biotechnological applications to control metal corrosion, bioremediation, and bioelectrochemical systems[3]. As previously stated, such processes are conducted through a series of redox reactions that facilitate electron flow. Unfortunately, many laboratory studies to characterize EET pathways are mainly based on cells grown on electrodes at a constant potential which masks the true nature of the dynamic control of organisms to adapt to various electron acceptors[4]. Therefore, in this thesis, I saught to evaluate EET on electron acceptors relevant to the environment.

A key biotechnological process for bioenergy is anaerobic digestion. This process converts organic compounds into biogas rich in methane (CH_4) through anaerobic processes like hydrolysis, acidogenesis, acetogenesis, and methanogenesis leaving energy-rich residues suitable for compost[5-7]. These processes can be achieved through indirect interspecies electron transfer (IIET), mediated interspecies electron transfer (MIET), or direct interspecies electron transfer (DIET)[5,7]. DIET is the most recently characterized interaction in which two organisms interchange electrons through a filamentous

appendage, a mix of cytochromes, or a conductive material[5]. It has been shown that *Geobacter metallireducens* can metabolize ethanol into acetate which *G. sulfurreducens* (*Gs*) can then use as an electron donor[8]. Although three *Geobacter spp.* have been shown to partake in DIET (*G. metallireducens, G. sulfurreducens, and G. hydrogenophilus*), *Gs* has gained the most attention as a model organism to study its extracellular appendages that transfer electrons[6]. *Gs* was the first genetically tractable acetate oxidizing Fe(III) reducer and it has gained more attention due to its bioremediation properties[9-11]. *Gs* can use various metal oxides to donate electrons[12-14] and was shown to be able to use an electrode as a final electron acceptor by forming conductive biofilms: which provides excellent applications for living biomaterials[15-17]. *Geobacter spp.* are found in anoxic environments like marine sediments where metal reduction plays a key role due to their syntrophic growth with methanogens[3]. Cytochromes play a key role in EET for *Geobacter spp.* that encode over 100 c-type cytochromes, which may allow them to form multiple pathways to the same electron acceptor or to adapt to different environmental conditions[18]. Although various cytochromes involved in EET in *Gs* have been characterized, little is still known about the minimum components required for *Gs* to carry out this important biogeochemical process.

1.2 *Geobacter sulfurreducens* and its Nanowires

Geobacter sulfurreducens is Gram-negative soil bacterium that has been used as a model organism to study EET due to the available genetic tools and sequenced genome[9]. *Gs* is characterized by its ability to reduce various insoluble metal oxides such as Mn(IV), Fe(III), and Co(III), processes that are relevant in various geochemical cycles[12-14,19]. Some

Geobacter spp. can also oxidize aromatic hydrocarbons and precipitate Ur(IV) from contaminated water bodies, which has led to the development of various bioremediation strategies using these microbes[12-14,19].

Gs gained recognition due to its capacity to reduce metal oxides in various environments like aquatic sediments, contaminated aquifers, and uranium-contaminated areas where metal-reducers are abundant[20]. Early biochemical studies demonstrated the participation of c-type cytochromes in Fe(III) reduction[18]. Among these cytochromes, the periplasmic cytochrome (Ppc) family OmcB, and the PilA-N filaments called "e-pili" nanowires were found to be involved in EET. These appendages are thought to increase bacterial surface area to gain access to electron acceptors located micrometers away from the cell. More than two decades ago, studies showed the presence of filaments when *Gs* were given insoluble electron acceptors, but not in the presence of soluble electron acceptors[21]. Subsequent phylogenetic analysis showed that the gene *GSU1496* annotated as *pilA-N,* encodes for a Type 4-like pilin which is nearly a third shorter than other T4P[21]. Deletion of *pilA-N* caused deficiencies in iron reduction and current production[21]. These studies provided the first evidence that *Gs* pili are involved in EET. Traditionally, type IV pili (T4P) provide cells with the ability to move, adhere to surfaces, or secrete proteins to the extracellular environment[22-26], but *Gs* showed no twitching motility and deletion of *pilT,* ATPase required for pilus retraction, had no effect on iron reduction[21]. However, *Gs* pili lack any metal cofactors, which makes it difficult to explain the high conductivity measured in the filaments. These results are the origin of the controversy in the field, where the role of PilA filaments in EET has been highly debated over the years.

To truly appreciate recent advances in the field, the history and foundations of the field must be addressed to reinterpret current and past data. As previously mentioned, *Gs* were isolated and characterized over three decades ago. The interest to study *Gs* grew due to their ability to assemble nanowires (thought to be e-pili for over ten years), to increase their biovolume and access metal oxides that are micrometers away from the cell[21]. The first study to show the relevance of nanowires in chemotaxis and extracellular electron transfer was conducted by Childers *et al.*[9]. In this work, motility assays demonstrated the role of both flagella and pili-like filaments in *G. metallireducens* as a means of motility to scavenge for metal oxides once electron acceptors were depleted from the vicinity. Genetic analysis showed that a close relative, *Gs* also encoded *pilA (pilA-N)*-related genes to assemble a T4P, which at the time was believed to grant *Gs* with the canonical features of these systems[9,22-26]. Thus a genetic system was developed to disrupt and mutate *Gs* genome to further study the role of these appendages in EET[27] which allowed for one of the biggest breakthroughs in the field, EET mediated by nanowires[21]. As explained above, Reguera *et al.* showed that *pilA-N* is essential for EET using insoluble electron acceptors as strains lacking this gene showed a severe deficiency in both current production and Fe(III) reduction[21]. Although various studies showed the importance of cytochromes in Fe(III) reduction like OmcB[12,18,28], MacA[20], PpcA[12,29], OmcS[30] or OmcZ[17,31], cytochromes were not known to form filaments. Therefore, PilA filaments were believed to be the key in the EET process.

Despite the knowledge of some of the components involved in EET, their regulation and interactions were still unknown. Genetic analysis from Juárez *et al.* showed that the *pilA-N* operon is regulated by a Two-Component System (TCS)[32]. A TCS in Gram-

negative bacteria is typically composed of a sensory protein (PilS) and a regulatory protein (PilR) that will mediate the transcription of the *pilA* operon[32-35]. It was shown that a *ΔpilR* strain had deficiencies in iron reduction, and the reduction of soluble electron acceptors was also affected[32]. These results provide the first evidence regarding the role of pili in EET, as a lack of PilA filaments affects nanowire secretion and EET as shown in Chapters 2 and 3. Although it was shown that cytochromes involved in both soluble and insoluble electron acceptor reduction were affected, only pili-related proteins were thought to be essential for Fe(III) reduction.

Following these discoveries, a series of studies characterized PilA-N to better understand the mechanism that allowed *Gs* to transfer electrons to insoluble electron acceptors via nanowires. Immunogold TEM imaging showed OmcS monomers aligned on top of what was believed to be PilA-N filaments[36], leading to the suggestion that OmcS acts as a conduit between PilA-N nanowires and terminal electron acceptor such as Fe(III) oxide. These works were the foundation of a series of genetic analyses where *pilA*-N was mutated or replaced by T4P from other Gram-negative bacteria, further increasing the perception that PilA was the *Gs* nanowire. Conductivity measurements of filament preparations provided futher insights into electron transfer mechanism[37] and subsequent studies aimed to better understand the role of aromatic residues in PilA. First, 5 aromatic amino acids at the C-terminus of PilA-N were mutated into Ala (F24A, Y27A, Y32A, F51A, Y57A) in the Aro5 strain, and their physiological impact was measured. This strain showed a severe defect in both iron reduction and current production while being able to secrete OmcS[38]. Conductivity measurements from filament preparations showed a lower conductivity compared to WT preparations. On the other hand, the introduction of

additional aromatic residues at the C-terminus of PilA created the Trp strain (F51W, Y57W) which yielded a more conductive pilus[39]. When we take a closer look at the mutations, we find that the Trp mutant has a mutation in *pilR* (Fig. 3.12) that affected its regulation which is shown to yield a higher abundance of extracellular OmcS[32] and OmcZ[40]. On the other hand, although aromatic residues play a key role in electron transfer, they are also essential for protein stability. It is possible that the filament itself is not stable enough to withstand the forces require to translocate OmcS and OmcZ from the periplasm to the extracellular environment which will be evaluated in this thesis.

When we look at the genetic evidence that pili are directly responsible for EET, we find studies where *Geobacter spp.* pili and *P. aeruginosa pilA* are heterologously expressed in a *ΔpilA-N* background to study their effect in EET. The expression of *G. uraniirreducens* pili in a *ΔpilA-N* background (*Gs-Gu)* showed growth deficiencies and lower rates of both current and iron reduction potentially attributed to lower concentration of extracellular OmcS[41]. Similarly, the expression of *P. aeruginosa pilA* (*Gs-Pa*) also showed lower iron reduction and current production rates although OmcS could be found extracellularly[42]. On the other hand, the heterologus expression of *G. metallireducens pilA-N* pilin gene yielded a more conductive filament with no apparent physiological effect[43]. These strains show various effects on *Gs* physiology, where *Gs-Gu* and *Gs-Pa* introduce pili that are longer than *Gs* native pili, which could affect the interaction between pili and the nanowire secretion machinery. Additionally, the sequence used to make *Gs-Gu* is annotated as a pseudogene which might not encode a pilin protein. Contrary to this, *G.metallireducens*

pili did not affect the physiology which might be due to a shorter peptide sequence that might not disrupt the native system.

As we can see, although all these strains have various modifications to the pilin sequence, one common factor I found in this thesis is that secretion of OmcS is affected when PilA is absent or altered. Recent studies from our lab showed that the *Gs* nanowires are not composed of PilA filaments, but of OmcS[44] and OmcZ[40,45] cytochromes. The cryo-EM structures show the assembly of both OmcS and OmcZ monomers into filaments, which shows for the first time the ability of cytochromes to polymerize. Although the field proposed the model where PilA filaments are coated with cytochromes to facilitate EET, our structures eliminate the need for cytochrome coating. In this work, we will analyze the role of PilA filaments in EET, its assembly, and secretion mechanism that allows *Gs* to transfer electrons to insoluble electron acceptors.

1.3 Thesis Overview

The studies described here describe the role of PilA-N-C filaments in EET, their interactions, and the assembly of nanowires:

Chapter 2 compares the canonical behavior of Type 4 pili to *G. sulfurreducens* pili. A mix of biochemical and phenotypical assays is combined with a cryo-EM structure to show the role of PilA-N-C filaments in EET.

Chapter 3 explores how modifications of *pilA* and related proteins in previous studies have led to the observed differences in the properties of *G. sulfurreducens* in physiologically relevant conditions and electrodes.

Chapter 4 assesses the relevance of the interaction between PilA-N and PilA-C to assemble a functional PilA-N-C filament through a series of *in vivo* and *in silico* approaches to determine a plausible assembly mechanism.

Chapter 5 studies the role of heme axial coordination shown in the OmcS nanowire filament cryo-EM structure that allows monomers to assemble into filaments.

The advances presented here clarify long-standing questions in the field regarding the composition and role of pili filaments in EET. A lot of the past and current data have to be revaluated in the scope of these new findings. One can only hope that this new knowledge helps lead the way to discoveries that help advance the field and lead to novel applications.

2. PilA-N is required for the secretion of nanowire-forming cytochromes

Structure of Geobacter pili reveals secretory rather than nanowire behaviour

Yangqi Gu*, Vishok Srikanth*, **Aldo I. Salazar-Morales**, Ruchi Jain, J. Patrick O'Brien, Sophia M. Yi, Rajesh Kumar Soni, Fadel A. Samatey, Sibel Ebru Yalcin & Nikhil S. Malvankar

* These authors contributed equally.

This chapter is a modified version of a published paper.

DOI: https://doi.org/10.1038/s41586-021-03857-w

2.1 Author Contributions

Y.G. prepared and optimized cryo-EM grids, collected data used to build the atomic model, performed the image analysis, reconstructed the pili filament structure, generated and refined the filament model with help from F.A.S. and V.S., biochemically analyzed filaments, performed AFM, circular dichroism, conductivity measurements, electrode fabrication and negative-staining TEM images. V.S. identified and purified pili filaments. A**.I.S.-M. performed adhesion and twitching motility assays. A.I.S.-M. and R.J. carried out biochemical analyses and genetic experiments.** J.P.O. grew biofilms on electrodes in microbial fuel cell. Y.G., S.M.Y. and R.K.S. carried out mass-spectrometric

analyses. S.E.Y. performed AFM imaging of cell-attached filaments. N.S.M. conceived, designed and supervised the project. Y.G., V.S. and N.S.M. wrote the manuscript with input from all authors.

2.2 Summary

Extracellular electron transfer (EET) by *Geobacter* species via surface appendages called microbial nanowires[21] is important in a wide range of globally-important environmental phenomena[46] and for applications in bioremediation, bioenergy, biofuels and bioelectronics. Since 2005, these nanowires have been thought to be type 4 pili (T4P) composed solely of PilA-N protein[21]. However, structural analyses demonstrated that during EET, rather than pili, cells produce nanowires made up of cytochromes OmcS[46,47] and OmcZ[48]. Here we show that *G. sulfurreducens* binds PilA-N to PilA-C to assemble heterodimeric pili which remain periplasmic under nanowire-producing conditions that require EET[49]. Cryo-electron microscopy revealed that C-terminal residues of PilA-N stabilize its copolymerization with PilA-C via electrostatic and hydrophobic interactions that position PilA-C along the outer surface of the filament. PilA-N-C filaments lack π-stacking of aromatic side chains and show conductivity 20,000-fold lower than OmcZ nanowires. In contrast to surface-displayed T4P, PilA-N-C filaments show structure, function and localization akin to type 2 secretion endopili[50]. Secretion of OmcS and OmcZ nanowires is lost when *pilA*-N is deleted and restored when PilA-N-C filaments are reconstituted. Substitution of *pilA*-N with T4P of other microorganisms also causes loss of secretion of OmcZ nanowires. As all major phyla of prokaryotes employ T4P-like systems,

this novel nanowire translocation machinery may have widespread impact in identifying the evolution and prevalence of diverse electron-transferring microorganisms and in determining the nanowire assembly architecture for designing synthetic protein nanowires.

2.3 Significance Statement

For the last decade, it was believed that PilA-N filaments were responsible for EET in *Geobacter sulfurreducens* and that the cytochrome OmcS played a supportive role in the process. Our recent findings have helped bring clarity to the field, where the conductive appendages have been properly characterized as OmcS and OmcZ filaments respectively. Thus, we hypothesize that the PilA filament plays a role in the secretion of these nanowires. Although cytochrome secretion has been associated with T2SS, the nanowire secretion machinery is still poorly understood. Therefore, the successful completion of this proposal will elucidate both the components of the secretion machinery and the interactions between these proteins that allow for EET. Furthermore, the proper characterization of these proteins will allow us to design mutants that will aid in the mapping of the electron pathway throughout the respiration process.

2.4 Introduction

Geobacter sulfurreducens has been studied for its capacity to transfer electrons extracellularly over micrometer distances using nanowires[21,37-39,41,51]. These studies wrongfully characterize PilA-N proteins as *Gs* nanowires based on point mutations, heterologous expression, and imaging. Due to *pilA-N*'s genetic similarity to other Type 4

pili (T4P), it was generally believed that *Geobacter* pilins were distinctively different from other T4P as they were believed to be the responsible for extracellular electron transfer (EET) and not their canonical functions such as attachment, biofilm formation, and motility[22-26].

The hypothesis of PilA-N filaments functioning as nanowires[21] is open to question[52] because : 1) the deletion of *pilA-N* also inhibits the extracellular translocation of OmcS[53,54] and OmcZ[54], which form nanowires essential for extracellular electron transfer to iron oxide and electrodes respectively[52]; 2) the presence of PilA-N in a filament of wild-type (WT) cells has not been established, only inferred from indirect evidence such as the presence of PilA-N monomer in filament preparations that also contain OmcS nanowires; 3) conduction along the length of a purified PilA-N filament has not been demonstrated; and 4) theoretical studies did not find significant conductivity in a hypothetical PilA-N filament structure except when aromatic residues were assumed within 3-4 Å of each other[52].

Although these claims have created doubt in the field regarding the composition of nanowires, our lab solved the structure of *Gs* nanowires using Cryo-EM. Our findings demonstrated that nanowires were composed of a 6-heme cytochrome (OmcS)[44] essential for iron reduction and an 8-heme cytochrome (OmcZ)[40,55] essential for current production rather than the predicted T4P PilA-N protein. These multi-heme cytochrome filaments show similar conductivity compared to previously reported PilA-N filaments suggesting that the previously studied filaments were the OmcS filaments[21,51]. Despite the multitude

of studies analyzing *G. sulfurreducens* intrinsic properties to transfer electrons extracellularly[21,30,32,37-39,41,44,51,56-58], the components, interactions, and mechanism through which PilA-N is involved in EET remain poorly understood.

In this work, our laboratory was able to solve the structure of *Gs* pili. The Cryo-EM structure revealed a heterodimeric subunit composed of the helical core protein (PilA-N) that interacts with a downstream-encoded protein, PilA-C, that forms a globular domain to assemble the filament[59]. Furthermore, the structure shows that PilA-N-C filaments do not have cofactors or aromatic residues within a 3.5 Å distance, which would not facilitate electron transfer as shown by the difference in conductance between PilA-N-C filaments and OmcS and OmcZ nanowires[40,46]. Additionally, I was able to characterize the role of PilA-N-C filaments in EET. My studies showed that, unlike other T4P, *Gs* pili do not provide the cell with mechanical properties such as movement or attachment. Furthermore, I was able to determine that PilA filaments are involved in EET. Strains where PilA-N was mutated or where other T4P are heterologously expressed hindered the cells' ability to reduce Fe (III) and produce current. Here, I show that PilA filaments are involved in the secretion of both OmcS and OmcZ nanowires accounting for their respective physiological deficiencies in iron reduction and current production. *Gs* shows an interesting similarity to the Type 2 Secretion System (T2SS) where the endopili remain intracellular and are known to export cargo, including cytochromes, from the periplasm to the extracellular environment[60-62].

2.5 Results

2.5.1. Splitting *pilA* into *pilA-N* and *pilA-C*

The *G. sulfurreducens* genome contains two neighboring genes related to *pilA*[54] (Fig. 2.1a). The first gene is annotated as *pilA-N* (GSU1496) because it encodes a 61-amino acid protein showing high amino acid sequence identity to the N-terminal α-helix of previously reported Type 4 pilin proteins but lacks the C-terminal globular domain found in T4 pilins[54] (Supplementary Data Fig. 1). Immediately downstream of *pilA-N* is a gene annotated as *pilA-C* (GSU1497) because it was thought to be the C-terminal globular domain missing from PilA-N[54] (Fig. 2.1a). PilA-N was hypothesized to be the only protein within *G. sulfurreducens* pili[21] due to the lack of sequence similarity among PilA-C and the globular domain of type 4 pilin proteins, even though all globular domains of T4P show low sequence conservation (Supplementary Data Fig. 1), but high structural conservation, extending to the predicted structure of PilA-C[63]. Gene fission of pilins is widespread in *Desulfuromonadales* species including *Geobacteraceae* and other iron-reducing bacteria[63]. Our phylogenetic analysis of a fused PilA-N and PilA-C sequence showed an independent line of descent along with PilA-N-C subunits of other *Geobacter* species, indicating that *Geobacter* PilA-N-C are evolutionarily distant from both T4P and endopili of type 2 secretion systems (T2SS) (Fig. 2.1b, Supplementary Data Fig. 1).

2.5.2. Discovery and identification of pili

We grew *G. sulfurreducens* WT cells using anodes of microbial fuel cells as sole electron acceptors[64]. These conditions require extracellular electron transport over

hundreds of cell lengths and therefore represent an ideal nanowire-producing condition[49,52]. Purified filament preparations from WT cells grown under these nanowire-producing conditions failed to show either PilA-N or PilA-C using immunoblotting (Supplementary Data Table 1), in agreement with our previous cryo-electron microscopy (cryo-EM) analyses that did not find any T4P-like filaments[46,48]. We further analyzed subcellular fractions of WT cells with anti-PilA-N antibodies and found that PilA-N is mainly associated with the inner membrane but is absent from the extracellular fractions. PilA-C is also similarly membrane-associated and absent from the extracellular fractions of WT cells[65] (Fig. 2.1c). Control experiments using antibodies against the cytoplasmic protein GroEL confirmed that there is little or no cross-contamination in these subcellular fractions as only cytoplasmic fractions showed GroEL (Supplementary Data Fig. 2). These studies suggested that *G. sulfurreducens* PilA-N and PilA-C are ultimately anchored to the inner membrane, akin to T2SS endopili that form a membrane-associated filament structure to secrete proteins via elongation/retraction cycles[50]. Similar to the overexpression of endopilins causing the filaments to extend beyond the outer membrane[50,66,67], we hypothesized that *G. sulfurreducens* filaments may extend outside the cell surface if PilA-N and PilA-C proteins were present at levels higher than that observed in WT. Both Δ*omcS* and Δ*omcZ* cells, lacking nanowire-forming cytochromes, showed an elevated abundance of PilA-N and PilA-C, and indeed we found pili-like filaments on the surface of these cells by negative-stain transmission electron microscopy (TEM) (Fig. 2.1d-g, Extended Data Fig. 1c-d). Overexpressing PilA-N and PilA-C from a plasmid in WT *G. sulfurreducens* also yielded extracellular pilus-like filaments (Fig. 2.3) with a smooth morphology distinct from the sinusoidal morphology of cytochrome nanowires[46,48] (Figs. 2.1f-g, 2.2a-b). In

contrast to cytochrome nanowires[46,48] or T4P[68] which need to be removed from cells via vortexing or blending, these pili-like filaments were loosely attached to cells, akin to endopili[67], and were shed in the media. Therefore, cell-free supernatant of Δ*omcS* cells was concentrated to purify PilA-N-C filaments (Extended Data Fig. 1).

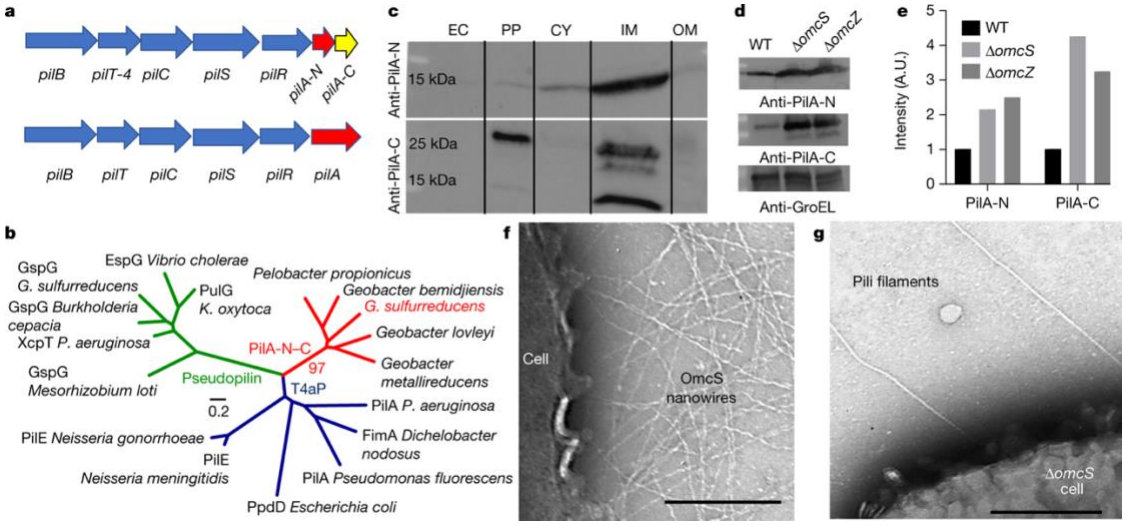

Figure 2.1: Discovery and identification of *G. sulfurreducens* pili.

a, Genomic organization of type 4 pili (T4P) biosynthesis genes in *G. sulfurreducens* (top) and *Myxococcus xanthus* (bottom). **b**, Phylogenetic distance tree derived from amino acid sequence alignments, showing the relationship of *Geobacter* PilA-N-Cpili and type 4a pilins (T4aP, blue branches) and endopilins (green branches) of other bacteria. See Supplementary Fig. 1 for details. **c**, Immunoblot of subcellular fractionation for PilA-N (about 6.5 kDa) and PilA-C (about 11 kDa) in wild-type cells. EC, extracellular; PP, periplasm; CY, cytoplasm; IM, inner membrane, OM, outer membrane. For gel source data, see Supplementary Fig. 4. **d**, **e**, Immunoblot for PilA-N and PilA-C in cell lysates (**d**) with quantification (**e**). Control, the cytoplasmic protein GroEL. For gel source data, see Supplementary Fig. 15. WT, wild type. **f**, Negative-stain TEM image of wild-type *G. sulfurreducens* cell showed only OmcS filaments on the cell surface. **g**, Pili-like filaments emanated from *ΔomcS* cell. Scale bars, 100 nm (**f**), 200 nm (**g**).

Adapted from Gu & Srikanth *et al.*,[59].

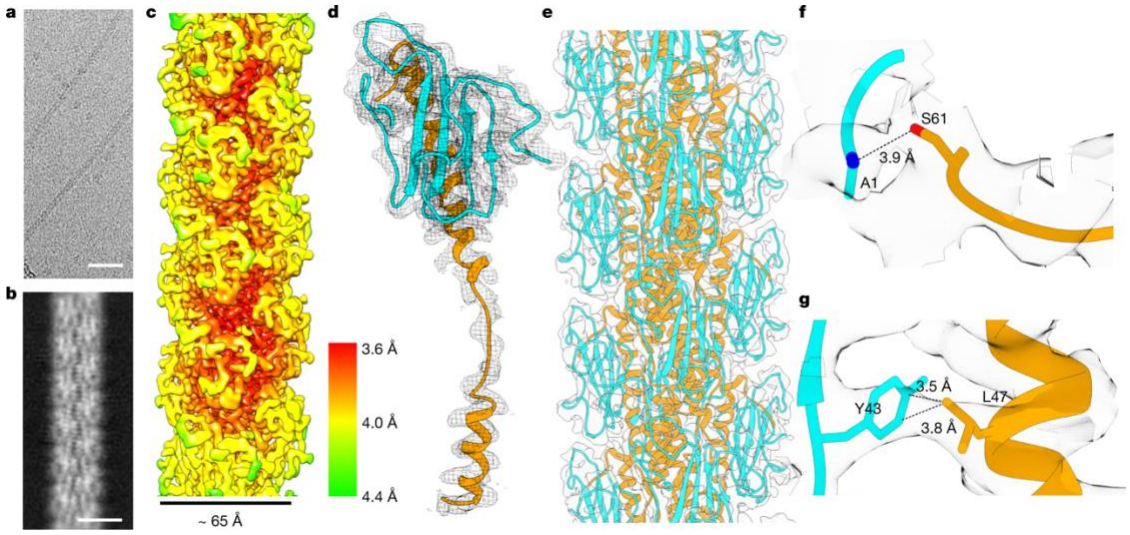

Figure 2.2: PilA-N recruits PilA-C to form a heterodimer that polymerizes into a filament.

a–c, Cryo-EM micrograph (**a**), two-dimensional average (**b**) and resolution distribution of a density map (**c**) of a PilA-N–C filament. Scale bars, 30 nm (**a**), 5 nm (**b**). **d**, **e**, PilA-N (orange) and PilA-C (cyan) form a heterodimer (**d**) that polymerizes into a filament (**e**). **f**, Charge interactions between S61 of PilA-N and A1 of PilA-C. **g**, Hydrophobic interactions between PilA-N and PilA-C.

Adapted from Gu & Srikanth *et al.*,[59].

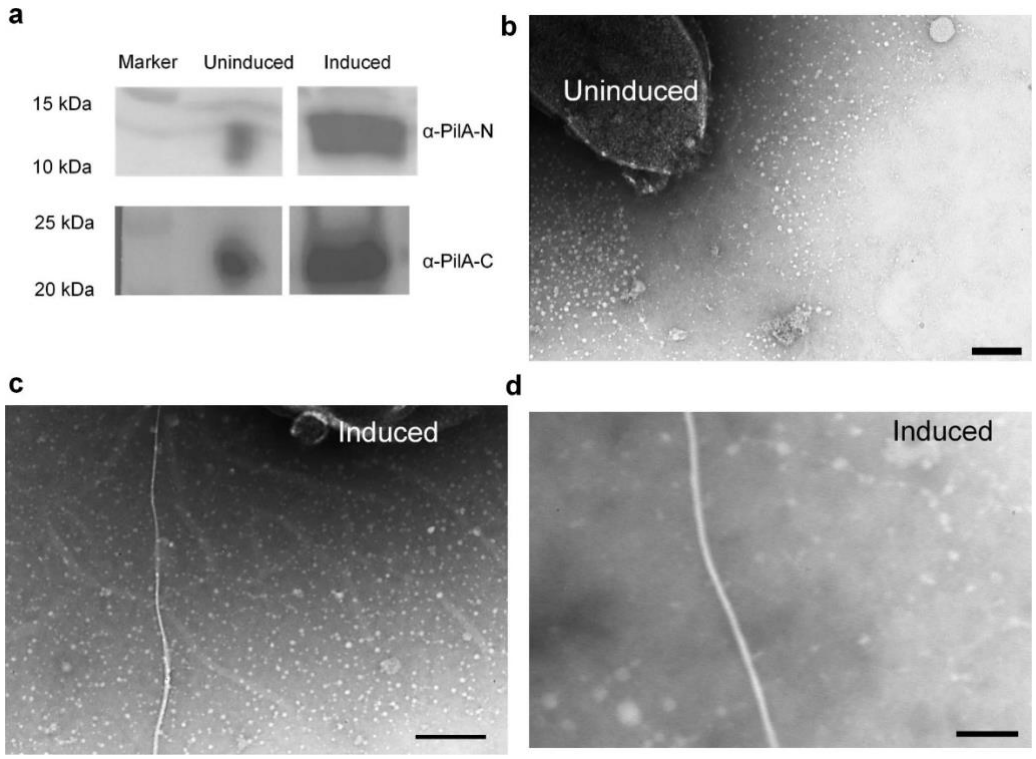

Figure 2.3 : Overexpressing PilA-N and PilA-C in wild-type *G. sulfurreducens* yielded pili-like filaments on the bacterial surface.

a, Immunoblot of whole-cell lysate showing overexpression of PilA-N and PilA-C under induced conditions. For gel source data, see Supplementary Fig. 8. b, c, Negative-stain TEM images of wild-type cells under uninduced (b) and induced (c) conditions. d, Zoomed image of pili-like filament shown in c. Scale bars, 200 nm (b, c), 50 nm (d).

Adapted from Gu & Srikanth *et al.*,[59].

2.5.3. PilA-N–C filaments are endopilins

G. sulfurreducens PilA-N-C filaments lack several hallmarks of T4P structure[69] and instead show similarity to the structure of type 2 secretion system (T2SS) endopili[70] (Fig. 2.4a-b). Firstly, a salt bridge between N-terminal F1 and E5 of neighboring subunits is highly conserved among all T4P and is crucial for their stability and assembly[69] (Fig. 2.4b). However, this salt bridge is absent in *G. sulfurreducens* PilA-N-C filaments. Instead, the N-terminal amine at F1 interacts with E5 from the same subunit to neutralize the buried charge. Adjacent PilA-N subunits are primarily stabilized by hydrophobic interactions (Extended Data Fig. 7b) , as has been observed in the endopili from *Klebsiella oxytoca*[70]. Secondly, the α-β loop in the globular head domain, which is involved in the subunit-subunit interactions in assembled T4P filaments[69], is absent in the PilA-N-C filament. Thirdly, the D-region in the globular head domain contains a disulphide bridge that is essential for assembly of some T4P filaments[69] but is notably absent in endopili[70] and in PilA-N-C (Fig. 2.4a). The lack of disulphide bridges, combined with the observation that PilA-N-C filaments are easily detached under the conditions where they extend from the cell, suggested that the biological function of PilA-N-C filaments is not as a durable, extracellular structure like T4P, but rather as a comparatively fragile, periplasmic assembly akin to type 2 secretion endopili [70]. Purified PilA-N-C filaments further exhibit melting of secondary structure features, denaturation, and disassembly at much lower temperatures than T4P[71] (Extended Data Fig. 8). PilA-N-C filaments are very loosely attached to cells and readily dissociated into pilin subunits under the buffer conditions widely used to purify T4[69], or upon the addition of mild detergents such as deoxycholate. All these studies demonstrate substantially lower stability of PilA-N-C compared to T4P filaments.

Likely due to this reduced stability, *G. sulfurreducens* PilA-N-C pili do not show any behaviors consistent with typical T4P functions such as adhesion and twitching motility (Extended Data Fig. 7), even under the artificial conditions which result in their display on the cell surface. WT, Δ*omcS*, and Δ*omcZ* mutant strains showed very low attachment to glass, comparable to Δ*pilA-N* cells (Fig. 2.4c). Replacing *G. sulfurreducens pilA-N* with T4P-forming *P. aeruginosa pilA* [72] increased the attachment by 100-fold (Fig. 2.4c). *G. sulfurreducens* strains displayed negligible twitching motility compared to *P. aeruginosa* (Fig. 2.4d) and were comparable to *P. aeruginosa* Δ*pilA*. These data are therefore more consistent with WT *G. sulfurreducens* expressing periplasmic endopili rather than surface-displayed T4P filaments.

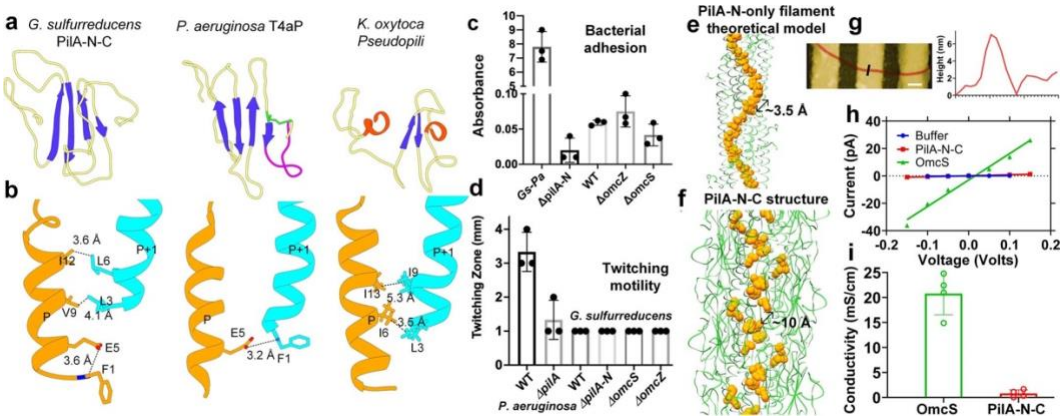

Figure 2.4*: Geobacter sulfurreducens* PilA-N–C pilus is structurally similar to a T2SS pseudopilus and does not show structure or functions of T4aP.

a, The globular domain of the PilA-N–C pilin protomer lacks hallmarks of T4P (PDB code 5XVY): disulfide bridge (green), four β-strands motif (blue) and D-region (magenta), consistent with endopili (PDB code 5O2Y). **b**, Hydrophobic interactions are the main interactions between PilA-N chains, similar to endopili, whereas T4P are additionally stabilized via intersubunit electrostatic interactions between F1 and E5. **c**, **d**, Comparison of bacterial adhesion to glass (**c**) and twitching motility (**d**). Error bars, s.d. (n = 3). **e**, **f**, Core aromatic residues in the theoretical model of PilA-N filament (**e**) and cryo-EM structure of PilA-N–C filament (**f**). **g**, AFM image of a PilA-N–C filament (red) bridging gold electrodes and corresponding height profile at location shown by a black line. Scale bar, 200 nm. **h**, **i**, Current–voltage curve (**h**) and corresponding conductivity comparison (**i**) for individual PilA-N–C filament versus OmcS nanowire. Error bars, s.d. (n = 4 biological replicates).

Adapted from Gu & Srikanth *et al.*,[59].

2.5.4. Nanowire secretion requires PilA-N–C pili

The lack of either nanowire or typical T4P functions suggests that the biological role of PilA-N-C filaments is not compatible with previous descriptions of *Geobacter* T4P function. In addition to classical T2SS, *G. sulfurreducens* also contain incomplete T2SS, lacking typical components of the machinery[50]. Deletion of the T2SS endopilin gene for the incomplete T2SS was not found to affect the translocation of outer-surface cytochromes[73]. Furthermore, other species that use classical T2SS for extracellular translocation of *c*-type cytochromes[62], do not show any secretion defect in the absence of pili[74]. In *G. sulfurreducens*, deletion of *pilA-N* does inhibit the extracellular translocation of OmcS and OmcZ[53,54], underscoring the involvement of pili in the secretion of nanowire-forming cytochromes. Our subcellular localization experiments revealed that both OmcS and OmcZ are present in the extracellular fraction of WT cells but remain in the periplasm for *ΔpilA-N* cells (Fig. 2.5a). These results suggested a translocation defect for OmcS and OmcZ in *ΔpilA-N*. Consistent with these studies, TEM showed OmcS nanowires on the surface on WT cells (Fig. 2.1f) but not on the surface of *ΔpilA-N* cells (Fig. 2.5b). Notably, *in-trans* expression of an episomal copy of WT *pilA-N* and *pilA*-C in *ΔpilA-N* (hereafter, *ΔpilA-N/pilA-N-C*) reassembled the PilA-N-C filaments on the bacterial surface and restored the secretion for both OmcS and OmcZ nanowires (Extended Data Fig. 10). As the primarily periplasmic localization (Fig. 2.1c) and the filament structure (Fig. 2.4a) of the PilA-N-C are similar to T2SS endopili, these cytochrome localization studies further suggest that PilA-N-C filaments could be functioning similar to endopili by translocating the OmcS and OmcZ nanowires from the periplasm to the outer cell surface.

To further evaluate the function of the PilA-N-C filament, we analyzed the localization of cytochromes in mutant *G. sulfurreducens* strains in which the chromosomal *pilA-N* gene was replaced by *pilA* of *P. aeruginosa*[75] (Fig. 2.5c-d). This strain cannot transport electrons extracellularly to iron oxides or to electrodes in microbial fuel cells[75]. Our TEM images showed T4P-like filaments in *Gs-Pa* (Fig. 2.5d). However, we found that filament preparations from electrode-grown *Gs-Pa* cells did not show the extracellular form of OmcZ ($OmcZ_S$) that assembles into nanowires [48] and only showed the periplasmic form of OmcZ ($OmcZ_L$), confirming that the cells were able to produce OmcZ but could not secrete it (Fig. 2.5c). This lack of $OmcZ_S$ could explain why these strains cannot transfer electrons to electrodes as $OmcZ_S$ is essential for electricity production[48,52]. In contrast, OmcS was translocated extracellularly by Gs-Pa[75], similarly to a strain in which *pilA-N* and *pilA-C* genes were fused[76]. Our studies thus show that the unique PilA-N-C filaments are essential for the translocation of OmcZ nanowires and are capable of secreting cytochromes without being displayed on the cell surface in a manner analogous to T2SS endopili[50,66,67]. The translocation of OmcS can be rescued as long as a T4P is present, likely because of similar secretory role for T4P[77].

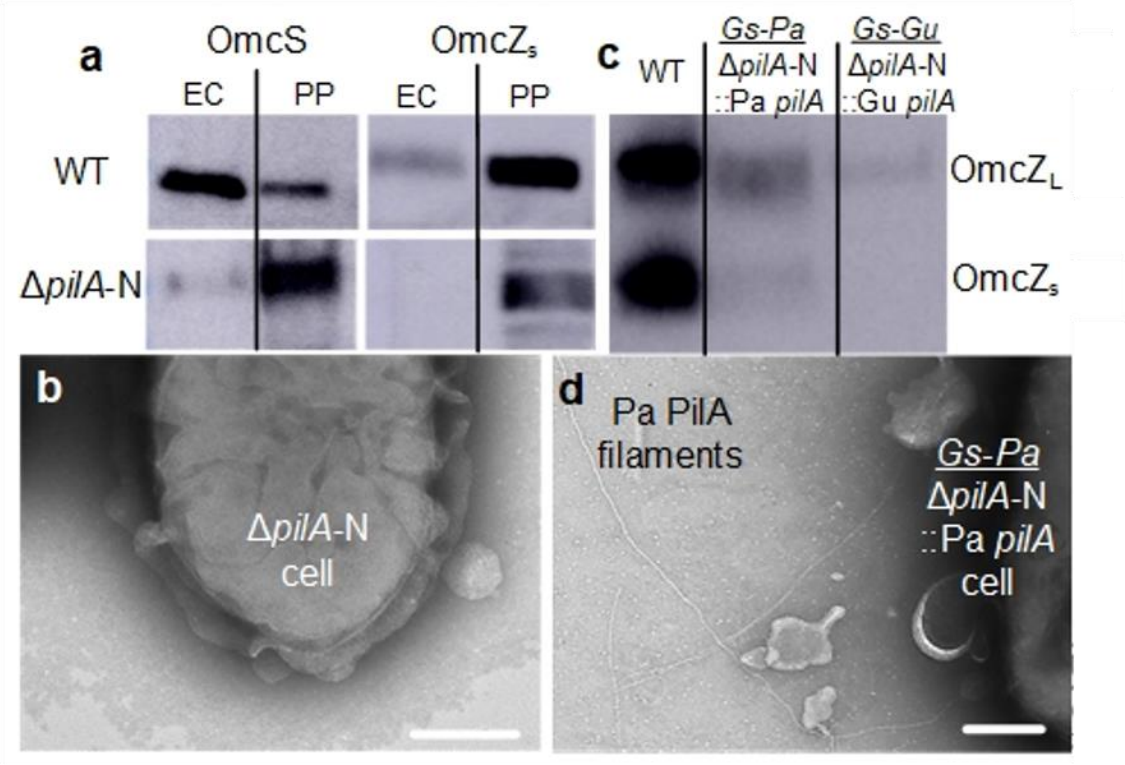

Figure 2.5: Geobacter sulfurreducens PilA-N–C pili are involved in the translocation of OmcS and OmcZ nanowires.

a, Subcellular fractionation showed the lack of secretion of OmcS and $OmcZ_s$ in the *ΔpilA-N* strain. b, Negative stain TEM images showed that the *ΔpilA-N* strain lacked OmcS filaments. Scale bar, 200 nm. c, Lack of nanowire-forming $OmcZ_s$ in filament preparations of *G. sulfurreducens* strains in which *pilA*-N was replaced with *pilA* of *P. aeruginosa* or *G. uraniireducens*. d, TEM image of Δ*pilA-N* cell expressing Pa *pilA.* Scale bar, 200 nm. Adapted from Gu & Srikanth *et al.*,[59].

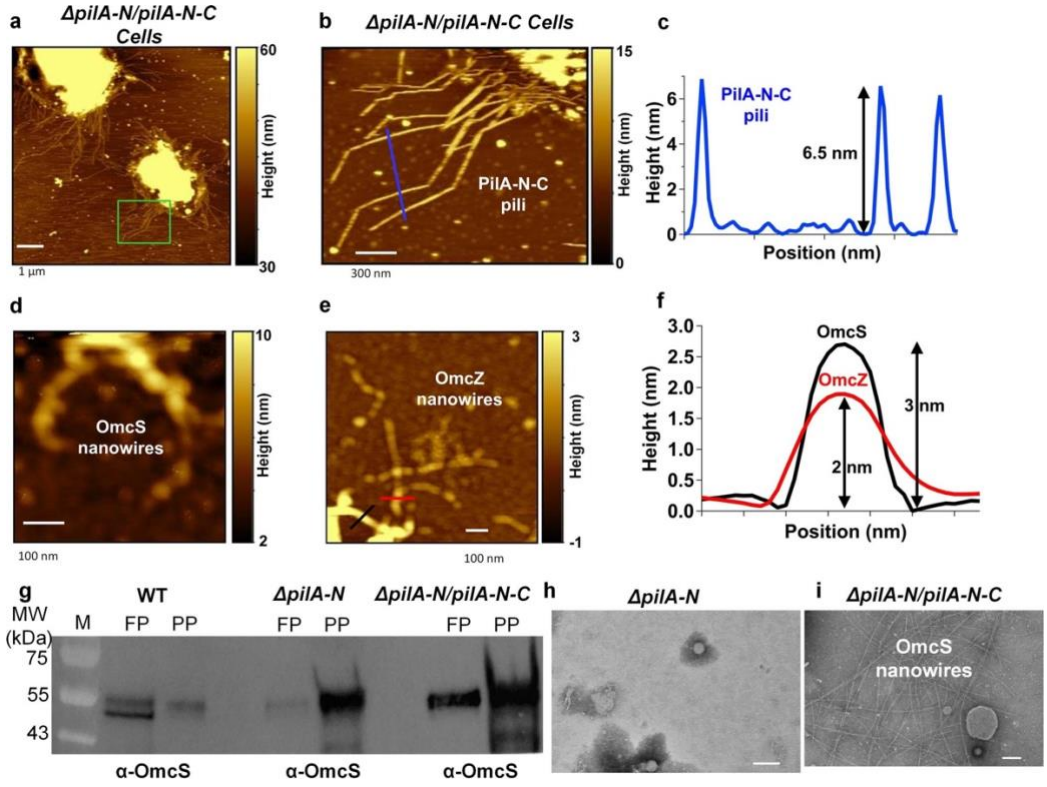

Figure 2.6: Expression of PilA-N–C filaments restores the secretion of OmcS and OmcZ nanowires in *ΔpilA-N* cells.

a, AFM images of *ΔpilA-N*/*pilA-N-C* cell showed pili on the surface of the cell. **b**, Zoomed-in image of *ΔpilA-N*/*pilA-N-C* cell. **c**, Height analysis of the pili consistent with PilA-N–C filament. **d**, **e**, *ΔpilA-N*/*pilA-N-C* cell showed the secretion of OmcS (**d**) and OmcZ (**d**) nanowires. Scale bars, 1 μm (**a**), 300 nm (**b**), 100 nm (**d**, **e**). **f**, Height analysis of filaments at locations shown in **e** showed the diameter consistent with OmcS and OmcZ filaments. **g**, Immunoblotting with OmcS antibody showing the restoration of secretion defect in OmcS nanowires in *ΔpilA-N*/*pilA-N-C* cells. FP, filament preparation; PP, periplasmic fraction; M, marker. For gel source data, see Supplementary Fig. 16. **h**, **i**, TEM image of filament preparation from *ΔpilA-N* showing no filament (**h**) and OmcS filaments from *ΔpilA-*

N/pilA-N-C (**i**). Scale bars, 200 nm (**h**, **i**). *ΔpilA-N/pilA-N-C*: in-trans expression of an episomal copy of wild-type *pilA-N* and *pilA-C* in *ΔpilA-N*.

Adapted from Gu & Srikanth *et al.*,[59].

2.6 Discussion

The high structural stability of T4P allows bacteria to move, uptake DNA, initiate biofilm formation, and secrete proteins while withstanding a force of >100pN[22-26]. Traditional T4P stabilize their subunits through a salt bridge that forms between F1 and E5 from the adjacent subunits[26,78] to form an extended stem primarily composed of PilA proteins and a short stem primed with minor pilins[60]. The absence of said priming complex has been shown to reduce or eliminate the features of T4P[60]. As shown in Figure 2.2 d-g and Figure 2.4b, PilA-N-C filaments stabilize their subunits through F1 and E5 stabilization within the same subunit as opposed to adjacent subunits. Furthermore, the C terminus of PilA-N serves as a scaffold for PilA-C to wrap itself around and stabilize the core of the filament as shown in Extended Data Figure 4. These properties are more akin to those observed in T2SS endopili. These filaments are composed of major endopilins and primed with a complex composed of minor endopilins that will allow the complex to export proteins, adhesins, toxins, cytochromes[60,61]. These features propose an interesting simile between the peculiarity of *Gs* pili and those of other T2SS and T4P that might help us understand the role of pili in EET.

As we established the composition of *Gs* pili, we were keen to further understand previous data supporting the claim that PilA-N was the nanowire. First, we performed a subcellular fractionation that allowed us to localize PilA-N and PilA-C monomers intracellularly, but not extracellularly as shown in Figure 2.1c. It is possible that their reduced stability does not provide *Gs* the capacity to use these appendages for motility or attachment as shown in Figure 2.4c-d, as canonical T4P are extracellular appendages due

to their mechano-sensing properties[22-26]. Interestingly, as we compared the subcellular localization of both OmcS and OmcZ nanowires in WT vs. *ΔpilA-N* we observed a translocation deficiency as both nanowires remain intracellular in the absence of PilA-N. Additionally, upon expression of the native PilA-N and PilA-C proteins, the translocation phenotype was restored as seen in Figure 2.6g. Overexpression of this protein in WT cells resulted in an extracellular filament as observed in *ΔomcS* and *ΔomcZ* strains where these proteins are overexpressed. This feature is a property of T2SS endopili as an increase in subunit levels results in an extracellular filament called Hyper Pseudopilus (HPP) characterized by an uncontrolled elongation of the filament[79,80].

These results demonstrate that *Gs* nanowires are composed of nanowire-forming cytochromes and not PilA-N filaments as previously thought. Our studies have shown that *Gs* pili are more akin to T2SS as they are involved in the secretion of cytochromes. Although we have established the role of PilA-N in EET, we still need to understand the mechanism and interactions that give rise to these phenotypes. To address these questions, we will purify PilA-NC filaments and probe their interaction with OmcS and OmcZ, as well as with some structural proteins from both T2SS and T4P through SPR and pulldown experiments to elucidate a possible mechanism whereby PilA-N-C filaments translocate nanowires.

2.7 Materials and Methods

2.7.1. Bacterial strains and growth conditions.

Geobacter sulfurreducens wild-type strain PCA (designated DL-1) (ATCC 51573) [27], the *pilA-N* knock out strain (designated as Δ*pilA-N*)[37], *omcS* knock-out mutant strain[30] (designated as Δ*omcS*), the *omcZ* knock-out mutant strain[31] (designated as Δ*omcZ*), *G. sulfurreducens* strains in which *pilA-N* was replaced by *pilA* of either *P. aeruginosa*[81] (designated as DL1-PA or *Gs-Pa*) or *G. uraniireducens* [82] (designated DL1-Uranii or *Gs-Gu*), *Pseudomonas aeruginosa* WT strain PAO1, and *Pseudomonas aeruginosa* strain Δ*pilA*, were obtained from our laboratory culture collection. *G. sulfurreducens* cultures were maintained at 30 °C or at 25 °C under strictly anaerobic conditions in growth medium supplemented with acetate (10 mM) as the electron donor and fumarate (40 mM) as the electron acceptor. As described previously[44], the *G. sulfurreducens* cells were grown in sterilized and degassed NBAF medium[83], which contained the following: 0.04 g/L calcium chloride dihydrate, 0.1 g /L, magnesium sulfate heptahydrate, 1.8 g/L sodium bicarbonate, 0.5 g/L sodium carbonate, 0.42 g/L potassium phosphate monobasic, 0.22 g/L potassium phosphate dibasic, 0.2 g/L ammonium chloride, 0.38 g/L potassium chloride, 0.36 g/L sodium chloride, and vitamins and minerals as listed in O'Brien *et al.*[83]. 1 mM cysteine was added as an oxygen scavenger. *G. sulfurreducens* cells were grown under nanowires-producing conditions as previously described[21], or grown using anodes of microbial fuel cells as sole electron acceptors[83]. The latter conditions require extracellular electron transport over hundreds of cell lengths and are therefore ideal nanowire-producing conditions that require long-range electron transport[37].

2.7.2. PilA-N–C overexpression

GSU1496 and GSU1497 were synthesized (Genscript) and cloned into pRK2-Geo2i[84]. Transformation was performed as described previously[84]. WT cells were cultured as previously described[84] and supplemented with kanamycin (200 μg/mL) and vanillate to a final concentration of 500 μM.

2.7.3. Sequence alignment and phylogenetic analysis

Amino acid sequences of pilins were obtained from UniProt and NCBI databases. For PilA-N–C pilin sequences, the truncated pilins (PilA-N or homologs) were manually fused with PilA-C proteins, excluding the signal peptides (based on the annotation from UniProt). Multiple sequence alignments of pilins were generated in MEGA X[85] using the MUSCLE algorithm. The aligned file was used as an input for maximum likelihood approach phylogenetic analysis using the PhyML 3.0[86], an online service provided by ATGC. The substitution model was automatically selected using Smart Model Selection [87] and the Akaike Information Criterion [87] was used to evaluate the model. Distance and branching order were constructed via the BioNJ algorithm and optimized via nearest-neighbor interchange. The bootstrap analysis was performed to evaluate the reproducibility, and the values were determined from 100 replicates. Final figures were generated using the ggtree [88] package implemented in R[89].

2.7.4. PilA-N–C filament and OmcS/OmcZ cytochrome nanowire purification and biochemical characterization

Both Δ*omcS* and Δ*omcZ* cultures were grown until stationary phase, and then centrifuged at 8,000 x *g* for 20 minutes to separate cells from the media. The supernatant was then passed through a 0.22 um filter, to remove the remaining cells, and concentrated with a 100 kDa cut-off Amicon concentrator (MilliporeSigma). The sample was then diluted in PBS and centrifuged at 100,000 x *g* for one hour. The pellet was resuspended in 20 mM Sorensen's buffer at pH 7.2 and used for cryo-EM.

For mass spectrometry, the sample was incubated with 2.5% styrene maleic acid (SMA) copolymer solution at room temperature and gently agitated on an orbital shaker. The sample was then centrifuged again at 100,000 x *g* and the pellet was collected and resuspended in 20 mM Tris-HCl at pH 7.4. The sample was further purified using a gel filtration column packed with Sephacryl S-500 HR resin (Cytiva). Elution fractions were evaluated with negative-stain transmission electron microscopy and polyacrylamide gel electrophoretic separation. The final purified filament-containing sample was used for mass spectrometry analysis.

In contrast to PilA-N–C filaments that were purified from the cell-free supernatant, both OmcS and OmcZ nanowires were purified by blending the cells as described previously[40,44].

2.7.5. Cell and protein normalization for comparative expression studies

Bacterial strains were grown to late exponential or stationary phase unless specified. For filament preparations, samples were normalized to the initial wet weight of the bacterial pellet. Equal volumes ($1/20^{th}$ of the final filament preparation protein) was loaded on the gels for comparison. Additional care was taken to collect the samples at a similar growth phase and optical density when comparing different strains.

2.7.6. SDS-PAGE

Samples were boiled in 1X SDS sample buffer that included β-mercaptoethanol for 12 minutes. The samples were run on a 16% tricine protein gel (Thermo Fisher Scientific) initially at constant voltage of 30 V for 2 hours before changing to 190 V for 30 minutes, at 4°C. Precision Plus Protein Prestained molecular weight standards (Bio-Rad) and Low Range Protein Ladder (Thermo Scientific) were used to compare the molecular weight of cytochromes in the filament preparations. Gels were stained with Coomassie R-250 stain for 1 hour (Thermo Scientific), and de-stained in deionized water overnight.

2.7.7. Immunoblotting

Polyclonal anti-PilA-N, anti-PilA-C, anti-OmcS and anti-OmcZ antibodies were produced by LifeTein by immunizing two rabbits with synthetic peptide sequences containing a targeted epitope on the native protein, and then affinity-purifying the serum against that peptide sequence. The antibodies were used at a dilution of 1:5000 for

immunoblotting. Filament samples were normalized to the initial cell mass of the starting material.

2.7.8. Mass spectrometry

For LC-MS/MS analysis of filaments, all the bands visible in SDS-PAGE were extracted from protein gels and digested with trypsin. Proteomic analysis of the cleaved peptides was performed by the Proteomics Mass Spectrometry Facilities at Yale University and Columbia University.

In-gel digestion. As described previously[90], filament samples were separated on 4-12% gradient SDS-PAGE, and stained with SimplyBlue (Thermo Fisher Scientific). Protein gel slices were excised and subjected to *in-gel* digestion. Gel slices were washed with 1:1 (acetonitrile: 100 mM ammonium bicarbonate) for 30 minutes; gel slices were then dehydrated with 100% acetonitrile for 10 minutes until gel slices had shrunk, at which point excess acetonitrile was removed, and slices were then dried in a speed-vac for 10 minutes using no heat. Gel slices were reduced with 5 mM DTT for 30 minutes at 56 °C in an air thermostat, the tube was chilled down to room temperature, and the sample was alkylated with 11 mM IAA for 30 minutes in the dark. Gel slices were then washed with 100 mM ammonium bicarbonate and 100 % acetonitrile for 10 minutes each. Excess acetonitrile was removed and dried in a speed-vac for 10 minutes with no heat, and gel slices were then rehydrated in a solution of 25 ng/µl trypsin in 50 mM ammonium bicarbonate, on ice, for 30 minutes. Digestions were performed overnight at 37 °C in an air thermostat. Digested peptides were collected and further extracted from gel slices in

extraction buffer (1:2 vol/vol) 5% formic acid/acetonitrile) with high-speed shaking in an air thermostat. Supernatant from both extractions were combined and dried down in a speed-vac. Peptides were dissolved in 3% acetonitrile/0.1% formic acid.

LC-MS/MS analysis. A Thermo Scientific™ UltiMate™ 3000 RSLCnano system and Thermo Scientific EASY Spray™ source with a Thermo Scientific™ Acclaim™ PepMap™100 2 cm x 75 μm trap column and Thermo Scientific™ EASY-Spray™ PepMap™ RSLC C18 50 cm x 75 μm ID column were used to separate desalted peptides with a 5-30% acetonitrile gradient in 0.1% formic acid over 100 minutes at a flow rate of 250 nL/min. The column temperature was maintained at a constant 50 ˚C during all experiments.

A Thermo Scientific™ Orbitrap Fusion™ Tribrid™ mass spectrometer was used for peptide MS/MS analysis. Survey scans of peptide precursors were performed from 400 to 1500 *m/z* at 120K FWHM resolution (at 200 *m/z*) with a 2 x 10^5 ion count target and a maximum injection time of 50 ms. The instrument was set to run in top speed mode with 3-second cycles for the survey and the MS/MS scans. After a survey scan, tandem MS was performed on the most abundant precursors exhibiting a charge state from 2 to 6 of greater than 5 x 10^3 intensity by isolating them in the quadrupole at 1.6 Th. CID fragmentation was applied with 35% collision energy, and resulting fragments were detected using the rapid scan rate in the ion trap. The AGC target for MS/MS was set to 1 x 10^4 and the maximum injection time limited to 45 ms. The dynamic exclusion was set to 45 seconds with a 10ppm mass tolerance around the precursor and its isotopes. Monoisotopic precursor selection was enabled.

Data analysis. Raw mass spectrometric data were analyzed using the MaxQuant environment[91] v.1.6.1.0, employing Andromeda for the database searches using default settings with a few modifications. The default was used for first search tolerance and main search tolerance: 20 ppm and 6 ppm, respectively. MaxQuant was set up to search with the reference *Geobacter sulfurreducens* database downloaded from UniProt. MaxQuant performed the search based on trypsin digestion with up to 2 missed cleavages. Peptide, site, and protein FDR were all set to 1%. The following modifications were used as variable modifications for protein identifications and quantification: oxidation of methionine, acetylation of the protein N-terminus, and deamination of asparagine or glutamine. Results obtained from the MaxQuant output combined folder were loaded into Scaffold (Proteome Software) for data visualization. Spectral counts were used for analysis to compare the samples.

2.7.9. Cryo-EM data collection and image processing

The PilA-N–C filament sample (3.5 µL) was applied to 400 mesh C-flat grids and plunge-frozen by a Vitrobot Mark IV (FEI). Frozen grids were imaged on a Titan Krios operating at 300 kV equipped with a K2 summit detector (Gatan). Micrographs were recorded with super resolution mode at 0.822 Å/pixel, with a total dose of ~62 $e^-/Å^2$ fractioned into 27 frames. A defocus range of 0.8 µm – 2.5 µm was used to collect ~7560 images in total. All movies were first motion-corrected with MotionCorr implemented in RELION 3[92], summing a total dose of ~20 e^- by using frames 2-10. The contrast transfer function [93] of motion-corrected images was estimated by GCTF v1.08[93]. Filament segments were manually picked with RELION, and all the helices were further segmented into

~280,000 particles using a box size of 400 Å and inter-box distance at 31.5 Å including 3 asymmetric subunits to save computational time. After 2D classification, ~160,000 particles were selected for further data processing. Averaged power spectra and the power spectra of the class average were analyzed to determine the helical symmetry with SPRING [94]. The helical symmetry was first deduced from Fourier-Bessel indexing and then compared with a simulated power spectrum. After trial and error, a helical rise of 10.5 Å and twist of 89.0° were imposed for the final reconstruction. All of the ~160,000 particles were used to generate a consensus map in RELION [95] using the iterative helical real space reconstruction algorithm [96]. A simulated helical lattice (relion_helix_toolbox) [95] with the deduced helical symmetry was used as a starting reference, since featureless cylinder gave a suboptimal reconstruction. An initial reconstruction at ~4.5 Å was produced and filtered to 10 Å to be used as the reference for 3D classification (K=4, tau=20) to address heterogeneity in the particles. After 3D classification, 100,000 particles were combined for the final refinement and gave rise to a ~4.2 Å reconstruction. After iteratively applied CTF refinement until no further improvement of resolution was achieved, the particles were polished with the Bayesian polishing framework[97] implemented in RELION, which further improved the resolution to ~3.8 Å based on the gold standard FSC.

2.7.10. Bioinformatic analysis

About ~160 C_α atoms were successfully traced from the subunit density and this estimated protein length was used for bioinformatic analysis. The proteome (n=81491) of *G. sulfurreducens* was obtained from NCBI and proteins with a length of 150 – 190 residues were selected (n=3992). All 3992 candidates were further examined using the

TMHHM2 server and only proteins predicted to have a single transmembrane domain were kept for further analysis. Using a Python script, proteins with a predicted TM helix longer than 20 amino acids within the first 60 residues were maintained and 13 potential candidates were used for further analysis.

2.7.11. Model building and refinement

The protomer density was segmented in UCSF Chimera[98] and the C_α backbone trace was manually constructed using Coot[99]. Based on the mass spectrometry and bioinformatic analyses and side chain density visible in the map, PilA-N and PilA-C were determined to be the constituents of the protomer and an all-atom model of the protomer was constructed and then refined using phenix.realspace_refine[100]. This refined protomer model was further extended to into a filament model in Chimera and refined against the filament density map using phenix.realspace_refine. The refined model was finally manually inspected and adjusted in Coot.

2.7.12. Atomic force microscopy

To visualize cells, 10 µL of buffer solution containing cell samples were deposited on mica. The excess buffer was absorbed with filter paper. The sample was air-dried and was mounted on a metal puck (Oxford Instrument, Cypher ES). To visualize individual filaments, 5 µL of buffer solution containing filaments were deposited on a silicon wafer insulated by a 300 nm silicon dioxide dielectric layer with gold electrodes patterned by electron beam as described previously[44]. AFM experiments were performed using soft cantilevers (OMCL-AC240TS-R3, OLYMPUS) with a nominal force constant of 2 N/m

and resonance frequencies of 70 kHz. The free-air amplitude of the tip was calibrated with the Asylum Research software and the spring constant was captured by the thermal vibration method. The sample was imaged with a Cypher ES scanner using intermittent tapping (AC-air topography) mode. AFM showed that gold electrodes were bridged with individual filaments to facilitate conductivity measurements (Figure 2.4G). All AFM image analyses for cells and filaments were performed using Gwyddion[101]. The AFM height cross section has been analyzed using IGOR Pro software (WaveMetrics).

2.7.13. Electrode fabrication

Electrodes made of gold separated by a 300 nm non-conductive gap were designed using electron beam lithography as described previously [44]. Interdigitated electrode devices were designed in Layout Editor, a computer-aided design program. Two layers of resists (50-nm-thick poly(methyl methacrylate) and 60-nm-thick UV-curable resist) were then sequentially spin-coated onto the cleaned substrate. Circuit patterns including nanoelectrodes separated by nano-sized gaps, microscale fan outs, and contact pads were transferred from a quartz mold to the UV resist with nanoimprint lithography in a homemade imprint chamber. The residual UV-resist layer and the poly(methyl methacrylate) underlayer were removed by reactive ion etching with fluorine-based (CHF_3/O_2) and oxygen-based gases respectively.

2.7.14. Conductivity measurement

All direct current measurement was carried out on interdigitated devices with a 300 nm gap. A single filament bridging two electrodes was first identified by AFM and the contact electrode was recorded. The device was then transferred to the stage of a probe station connected to a semiconductor parameter analyzer. A sweeping voltage from -1 V to 1 V was first applied to estimate the range of current response. Then, by selecting the proper sensitivity for current detection, a stepwise voltage was applied with 50 mV increments. Each filament was measured within a proper low voltage range (<0.25 V) to maintain the linear behavior of the current-voltage (I-V) curve. Each measurement was made over a long waiting period to ensure the stability of the current (> 200 s) and a lack of faradic currents or electrochemical leakage as is normally evident in a buffering system. The conductance (G) was extracted by fitting the current-voltage curve with a linear function and was further converted into conductivity (σ) by applying the relationship $\sigma=G(L/\pi r^2)$ where r is the radius of the pilus and L is the distance between two electrodes.

2.7.15. Cell attachment assays

Mid-log cells were inoculated at a 1/100 dilution into 10 mL glass tubes of fresh NBAF media. Cells were incubated for 4 days (until approximately mid-log phase) at 30°C. Cultures were gently inverted 5 times and planktonic cells were decanted. Tubes were washed with Mili-Q water and remaining cells were stained with 10 mL of 0.1% crystal violet for an hour and then washed with Mili-Q water. Crystal violet was dissolved utilizing 10mL of 1% acetic acid for an hour and measured at 580 nm using a NanoDrop 2000c spectrophotometer.

2.7.16. Subcellular fractionation

G. sulfurreducens cells were fractionated using a previously published protocol[102] with the following modifications. 300 mL of late-log phase culture grown in NBAF was pelleted at 6000 x *g* for 15 minutes at 4 °C. The supernatant was filtered through a 0.22 µm filter and concentrated via a 10 kDa cut off Amicon concentrator. The final concentrate was labelled as the extracellular fraction. Other fractions were prepared as described previously[102].

2.7.17. Twitching motility assay

Twitching assays were performed by stab-inoculating *P. aeruginosa* and *G. sulfurreducens strains* in LB agar and NBAF agar plates, respectively[21]. Three colonies were stab-inoculated for each strain, and the diameter of the twitching zone was measured. *P. aeruginosa* strains were incubated overnight at 37 °C and then left at room temperature for 24 hours before removing the agar to measure the twitching zone. *G. sulfurreducens* strains were incubated in strict anaerobic conditions for 7 days at 30 °C before removing the agar.

2.8 Acknowledgments

We thank Lisa Craig, Stephen Lory, and Yong Xiong for discussions; Eric Martz for calling our attention to the "flaps" in PilA-N–C, for the Supplementary Videos, and for the Interactive 3D Visualizations available alongside the online version of this publication;

Derek Lovley, Kengo Inoue, and Barbara Kazmierczak for providing strains; Shenping Wu and Marc Llaguno for help with cryo-EM; and Tukiet Lam and Jean Kanyo for help with mass spectrometry analysis. We thank Tristan Croll for help with ISOLDE. This research was supported by a Career Award at the Scientific Interfaces from the Burroughs Wellcome Fund (to N.S.M.), the National Institutes of Health Director's New Innovator Award (1DP2AI138259-01 to N.S.M.), and an NSF CAREER Award (no. 1749662 to N.S.M.). Research was sponsored by the Defense Advanced Research Project Agency (DARPA) Army Research Office (ARO) and was accomplished under Cooperative Agreement Number W911NF-18-2-0100 (with N.S.M). This research was supported by NSF Graduate Research Fellowship award 2017224445 (to J.P.O.) and NIH Training Grant T32 GM007223, which supported V.S. Research in the Malvankar laboratory is also supported by the Charles H. Hood Foundation Child Health Research Award, and the Hartwell Foundation Individual Biomedical Research Award.

2.9 Supplementary Information

Any supplemental information not performed directly by this author was excluded and can be found in the SI to the published work at this location:

https://doi.org/10.1038/s41586-021-03857-w

3. *pilA-N* mutations affect cytochrome-forming nanowire secretion in *Geobacter sulfurreducens*

Observation of single Geobacter cell transferring electrons via cytochrome nanowires secreted by hybrid Type 4-Type 2 pili

Aldo I. Salazar-Morales[*], Sibel Ebru Yalcin[*], Matthew J. Guberman-Pfeffer, Yangqi Gu, Anthony Coelho, Jerry Ruvalcaba, Ruchi Jain, Vaishakh Kedambaimoole, Neelotpala Kumar, Konandur Rajanna, Deji Akinwande and Nikhil S. Malvankar

* These authors contributed equally.

3.1 Author Contributions

S.E.Y., A.I.S.-M. and N.S.M. conceived and designed the study. S.E.Y. and N.S.M. supervised the project, and co-wrote the manuscript with inputs from all authors. **A.I.S.-M. grew strains, performed biochemical and EET studies, and generated the Aro5:NC, pk:18:*pilY1-1* pk:18:*pilY1-2*, pk:18:*pilQ*, and pk:18:*gspD* strains.** A. C. and J.R. helped with biochemical and EET studies. S.E.Y. prepared samples for AFM, immunogold labelling, EFM, EDX, performed all of the single cell nanoscopic imaging on mica and EET measurements on Graphene Oxide, and analysed the data. S.E.Y also developed the schematic models for biofilm EET through OmcZ nanowires and Fe(III) reduction through OmcS nanowires. M.J.G-P. performed molecular dynamics and

computed the mechanical stability of pili. Y.G. solved the structure of OmcS nanowires from Aro5 and Trp strains. A.C. and J.R. helped with biochemical assays. R.J. analysed whole genome sequencing data. V.K. and N.K. synthesized graphene oxide under the guidance of K.R. and D.A.

3.2 Summary

Microbial extracellular electron transfer (EET) via pili "nanowires" is invoked to explain various globally-important environmental processes and applications. However, this concept has remained highly controversial due to the absence of direct methods to identify filaments used for EET. Correlating genetic and biochemical analysis with electrostatic force microscopy, here we directly visualize and quantify EET at the single-cell level. We find that *Geobacter sulfurreducens* use cytochromes OmcS and OmcZ as nanowires, not pili. Strains with genetically modified pili, purported to change pili conductivity, instead show a severe defect in the secretion of OmcS and OmcZ, which strongly correlates with EET. Deletion of *pilQ*, encoding porin for Type-4 pili, does not affect EET. In contrast, disruptions of *pilY*-1-2, encoding pili cap, or *gspD*, encoding porins for Type-2 secretion endopili, show severe defect in secreting nanowire-forming cytochromes, and thereby EET. Our work demonstrates a new class of hybrid Type-4 and -2 secretion endopili.

3.3 Significance Statement

For close to two decades, the *Geobacter* field has stated that *Gs* e-pili or nanowire is composed of the T4P-like protein PilA-N. Recent work from our lab showed that these

nanowires are composed of cytochrome-forming filaments OmcS[44] and OmcZ[40,45] and that PilA-N has a secretory role rather than being the actual conductive appendage it was once believed to be[9]. In this work, we show for the first time the impact of genetically manipulating *pilA-N* in the context of iron reduction and current production giving a clear explanation of previous results attributing these features to PilA-N[38,39,42,103]. Furthermore, we provide experimental evidence of single-cell imaging showing EET along OmcS and OmcZ nanowires. This results suggest that *Gs* pili are not a nanowire, but rather partakes in a hybrid system combining Type 4- and Type 2 secretion system components to secrete nanowires.

3.4 Introduction

Diverse microbial species[21,104-106] use pili-like filaments as "microbial nanowires" for EET during anaerobic respiration using Fe(III) oxides[21,107] and electrodes[49,108], as well as for direct interspecies electron transfer (DIET)[109,110]. It has been hypothesized that nanowires are made up of Type IV pili (T4P) wherein the aromatic residues would confer conductivity[49]. For example, the pilus-like archaellum of *Methanospirillum hungatei* is proposed to be conductive[105] due to stacked aromatic residues[111]. However, the conductivity was measured across the diameter of individual filaments, not along their length[105], and the physiological role of conductivity is unclear.

To evaluate the role of filaments in EET, we chose *G. sulfurreducens* as a model organism because it produces conductive filaments[49], has a fully sequenced genome, and is a well-developed genetic system[21]. *Geobacter* species are also the most prominent Fe(III)

oxide reducers in soil and sediment environments, and they produce among the highest known current densities in bioelectrochemical systems for pure cultures by forming highly-conductive biofilms that are 100-fold thicker than the cell's length[49]. These species are also models for DIET via nanowires[109] which drive globally important processes that regulate atmospheric methane levels such as the anaerobic oxidation of methane[112] and conversion of CO_2 to CH_4[113]. High nanowire conductivity could explain the ability of these microbes to transfer electrons rapidly at rates too fast for diffusion[112].

A central metabolic requirement for the growth of *Geobacter* is that the cells must transfer electrons to a volume of electron acceptors ~50 times larger than their biovolume in order to replicate[114]. Accounting for measured cellular yields, in both Fe(III)-reducing chemostats and on electrodes, bioenergetic calculations suggest that a single cell must reduce all Fe(III) oxide available in the space extending 2–4 μm in all directions beyond its outer membrane to generate the ATP required for a single cell doubling[114]. *G. sulfurreducens* are not motile[115], they do not produce redox-active shuttle molecules for EET[116], and they require direct physical contact with electron acceptors to respire[21], thus ruling out any diffusion-based EET used by *Pseudomonas*, *Shewanella* and various gut microbes, which becomes ineffective under fluid flow[117].

Bioenergetic calculations further suggest that from a cell resource perspective, constructing a randomly-oriented matrix of conductive proteins is also not feasible because such a matrix would consume nearly 900% of a cell's proteins for a 50 kDa protein[114]. However, if this same 50 kDa protein is aligned less than 1 nm apart from each other to

form a linear chain as a nanowire, 100 such chains extending in all directions would cost less than 3% of the cell's total protein[114], while enabling the required EET to reduce the cell's volume ~50 times.

To transfer electrons to electron acceptors that are many micrometers away, we and others had initially proposed that cells specifically produce conductive T4P, composed solely of PilA-N, in response to growth on insoluble electron acceptors such as Fe(III) oxide[21] and electrodes of bioelectrochemical systems[49]. However, recent structural, functional, and cellular localization studies using cryo-electron microscopy (cryo-EM)[46,48,118-120], multimodal nanoscopic imaging[48], as well as biochemical and genetic analyses[115] revealed that all the surface-displayed filaments during EET are polymers of cytochromes OmcS [46] and OmcZ [48,119,120] rather than PilA-N pili (Fig. 3.1b). The T4P-like filaments, formed by subunits of PilA-N and PilA-C, remain intracellular during EET, and show low conductivity[115,121]. Strains with modified OmcS show filaments of another cytochrome OmcE under non-EET growth conditions[118].

Mass spectrometry and biochemical analysis of purified filaments[48], immunogold-labelling with cytochrome-specific antibodies[48], and use of distinct morphological features such as helical pitch[46] and filament height [48] to correlate with the atomic structure confirmed the identity of conductive filaments as the OmcS and OmcZ cytochromes[46,48,52,122]. These filaments have seamless stacking of hemes, allowing efficient transfer of electrons over the entire micrometer-length of the nanowires[46,48,123] (Fig. 5.1b, inset). Genetic studies have suggested that out of 111 cytochromes in the genome of *G.*

sulfurreducens, only the nanowire-forming cytochromes OmcS and OmcZ are essential for EET to Fe(III) oxide[124], and to anodes of bioelectrochemical systems[125], respectively. Furthermore, both the molecular weight of OmcS and OmcZ (50 kDa), and their micrometer-long highly-conductive structures are consistent with the above-mentioned cellular bioenergetic requirement of EET to reduce electron acceptors in a volume ~50 times that of the cell[114].

However, the physiological roles of pili and cytochrome nanowires in bacterial EET have remained highly controversial due to a lack of direct methods that can determine filament identity during bacterial EET to Fe(III) oxides and electrode[52]. This lack of methods has severely limited studies on bacterial filaments only to their structure determination, prohibiting critical functional and physiological studies[118]. Furthermore, recent articles have strongly questioned the role of cytochrome nanowires and have remained focused on pili-based EET without any direct evidence[126,127]. For example, there is no biochemical evidence that *G. sulfurreducens* performs EET via pili. Pili-like filaments were observed only on the surface of cells that were not performing EET, but were instead grown on soluble electron acceptor fumarate which is reduced intracellularly[128]. The presence of PilA-N monomer in filament preparations is taken as evidence for surface-displayed PilA-N filament[127], but this method is prone to cellular contamination and cannot distinguish between intra vs. extracellular pili [115]. Imaging of antibody-recognizing PilA binding to surface-displayed filaments is limited to the use of artificial tags[129], or performed at a magnification where filaments are not visible[130]. Increasing the abundance of aromatic residues in PilA-N is thought to produce more conductive pili[59]. However, such a mutation

causes higher abundance of OmcZ nanowires that show conductivity and morphology similar to filaments that were previously thought to be pili[48]. Heterologous expression of *pilA*-N in other bacteria was purported to produce PilA-N filaments[128], without any biochemical evidence that the filaments are similar to native pili. Furthermore, conductivity of these synthetic pili was measured only across the diameter[128], and not along the length, making it difficult to evaluate their role in bacterial EET. It has been claimed that 3 nm-diameter filaments in filament preparations are made up of PilA-N[47] whereas studies by multiple groups found that such filaments are made up of DNA instead[115,118] .

Notably, none of the prior studies have shown directly that bacteria perform EET via nanowires due to a lack of methods to identify the composition of filaments used for EET[118]. Here we visualize EET to minerals and electrodes by living bacteria at a single-cell level. We identify the composition and function of individual filaments by correlating biochemical and genetic analyses to EET[46,48,115]. Moreover, we show that alterations to the pili impact the ability of *G. sulfurreducens* to conduct electrons indirectly by disrupting cytochrome nanowire production, rather than by directly disrupting pilus-mediated election transfer. We provide evidence that the secretion defect in *pilA*-N mutants is due to changes in pilus stability or lower abundance of pilus cap called PilY1-2. Disruption of *pilQ*, encoding porin for Type-4 pili, does not affect EET. In contrast, disruption of *gspD*, which encodes porin for Type-2 secretion endopili, show severe defect in secreting nanowire-forming cytochromes, and thereby EET. In addition, we find that *pilA*-N mutants truncate the *pilA* transcriptional regulator called PilR, and overproduce cytochrome nanowires. Our

studies thus determine the distinct physiological roles of various filaments produced by *G. sulfurreducens* during EET to minerals and electrodes.

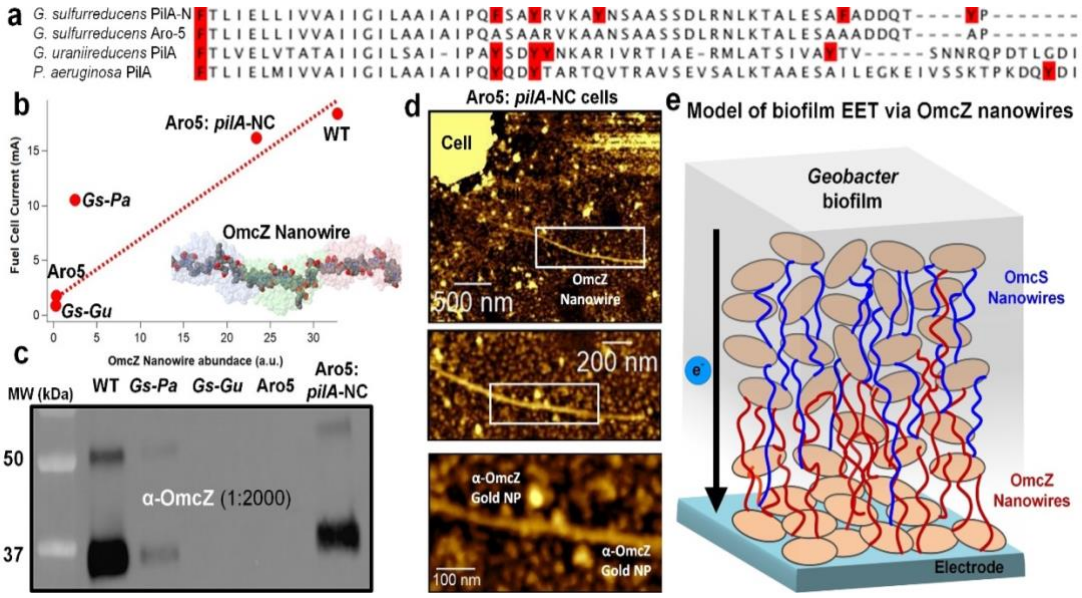

Figure 3.1: Bacteria use OmcZ nanowires to transfer electrons to electrodes.

a, Amino acid sequence alignment for pili used in this study. Red: Aromatic residues. **b,** EET to electrodes is correlated with the abundance of OmcZ nanowires. **Inset:** OmcZ nanowire structure (PDB ID: 7LQ5) **c,** anti-OmcZ immunoblot of filament preparations of *G. sulfurreducens* cells grown on electrodes. **d,** AFM images of anti-OmcZ immunogold-labelled Aro5:NC cells expressing OmcZ nanowires. Areas shown in the square are zoomed in the subsequent images **e,** Model of *G. sulfurreducens* biofilm cells utilizing cytochrome nanowires for EET on electrodes.

3.5 Results

3.5.1. Bacteria use OmcZ nanowires to transfer electrons to electrodes.

A central claim for the pili nanowire hypothesis[127] is that substituting aromatic residues in PilA-N affects EET (Fig. 3.1a-b) and filament conductivity, which was interpreted as due to a change in pili conductivity [131], but filament identity was not confirmed in previous studies. Furthermore, how these mutations affect the secretion of cytochrome nanowires had not been previously examined.

We grew *G. sulfurreducens pilA-N* mutant strains performing EET to electrodes. We found that replacing five aromatic residues in *pilA-N* to alanine (hereafter, Aro5)[131], or replacing *pilA-N* with pilins of *Pseudomonas aeruginosa*[75] (hereafter, *Gs-Pa)* and *G. uraniireducens*[103] (hereafter, *Gs-Gu*), caused defects for *G. sulfurreducens* both in EET to electrodes and secretion of nanowire-forming OmcZ (Fig. 3.1b-c, Extended Data Table 3.1d,f and Table 3.2a,b). Both phenotypes were restored upon complementing with *pilA*-N-C (hereafter, Aro5: *pilA*-NC) (Fig. 3.1b-d). Notably, we found a strong correlation (R^2=0.91) between the current produced by EET to electrodes and the OmcZ nanowires produced by the cells, as assessed by immunoblots of filaments purified from each strain (Fig. 3.1b). Only strain *Gs-Pa* deviated slightly from this relationship, likely due to its ability to attach more strongly to surfaces than other strains[115]. Previous studies failed to find such correlations because OmcZ was quantified from biofilm cell pellets instead of purified filaments[132].

Based on these results, showing that the abundance of OmcZ nanowires regulates EET to electrodes, we developed a model (Fig. 3.1e) also taking into account the highest abundance of OmcZ found near the electrode[133] and the highest metabolic activity by biofilm cells found near the electrodes[134]. Our EET model is independent of monomeric cytochromes or pili, used in previous models[135,136], which are found to be absent from the surface of bacteria growing on electrodes[115,137].

3.5.2. EET imaging reveals bacteria use cytochrome nanowires, not pili.

To understand the mechanism of bacterial EET, we used atomic force microscopy (AFM) to image *G. sulfurreducens* cells producing OmcS and OmcZ nanowires as well as pili in response to different growth conditions[48] or genetic mutations[46]. We found that WT and CL-1 cells produce OmcS nanowires (characteristic 4 nm-height and 20 nm-helical pitch)[46] (Extended Data Fig. 1a-b) as confirmed by the biochemical analysis of filament preparations using SDS-PAGE (Fig. 3.2b) and mass spectrometry (Table 3.3a,e)[138]. In contrast, we found that *ΔomcS* cells produced OmcZ nanowires[48,52] 2.5 nm in height (Fig. 3.7c-d) when grown under conditions that induce OmcZ[48] (Table 3.4c), in agreement with biochemical and immunogold-labeling studies[48] (Fig. 3.7e-f). Mass spectroscopy confirmed that the only filament-forming proteins abundant in *ΔomcS* cells are OmcZ and PilA-N-C pili (Table 3.4c), consistent with *ΔomcS* cells showing PilA-N-C pili on their surfaces (~7 nm-height)[46,52,115] (Extended Data Fig. 2a-c). This finding was further confirmed by other research groups[118]. Mass spectrometry also confirmed that all strains used in our studies do not exhibit OmcE which can also form filaments when OmcS is modified (Table 3.3 and 3.4)[118] .

Contrary to the previous hypothesis that pili serve as nanowires[21], we[115] and others[118] have found that pili remain periplasmic under EET conditions and extend to the cell surface when overexpressed in response to deletions of nanowire-forming cytochromes. Even when displayed on the surface, pili show 20,000-fold and 50-fold lower conductivity than OmcZ and OmcS nanowires respectively (Fig. 3.1g), suggesting that they are unlikely to serve as a conduit for EET[115].

To directly visualize bacterial EET via nanowires, we grew cells using graphene oxide (GO) as the sole electron acceptor (Fig. 3.2a). In its pristine state, GO is a non-conductor[139] (Fig. 3.9). When electrons are transferred by bacteria to the GO surface, it is locally reduced (rGO) and becomes an electrical conductor, allowing electrons to propagate through the reduced surface[139]. Soil bacteria reduce GO via EET[140,141], and rGO can serve as an electrode for bioelectrical systems[142]. However, the underlying EET mechanisms on GO have remained unclear.

We have previously used electrostatic force microscopy (EFM) to monitor the changes in the conductivity of GO upon reduction[139]. Here we use EFM to map the conductive regions of bacterially-reduced GO due to EET via filaments (Fig. 3.2e-g, Fig. 3.9). We initially operate EFM in lift mode that moves the tip ~20 nm away from the surface and measure long range electrostatic forces over the GO surface using a tip voltage maintained at V_{EFM} = +3V (for Fig. 3.2d and f), a voltage typically used for imaging electrons in nanostructures[143]. In the next step, the lift height of the EFM cantilever was lowered closer to the GO surface and the tip voltage was pulsed at an electron injection voltage of V_{INJ} = -10V, a voltage typically used for injecting the electrons periodically

every 2 seconds in GO and shown to cause no measurable damage to GO while maximizing the EFM signal. We injected charges at a single point on GO by gently touching (the injection point is labelled with a blue cross shown with a red arrow in Fig 3.2d and f) and visualized the propagation of injected charges through another EFM scan in the lift mode under the same experimental conditions with the same tip used before charge injection (Fig. 3.2e and g).

We found regions of conductive (white-colored) rGO, hundreds of nm to µm away from the bacterial cell surface (Fig 3.2c, e and g), but only in the vicinity of OmcS and OmcZ nanowires that are attached to cell (Fig. 3.2 and Fig. 3.8). The bare GO surface was not reduced by itself (Fig. 3.9a-f) or with purified nanowires lacking bacteria (Fig. 3.9g-k), suggesting that the reduction of GO occurs only when metabolizing bacteria perform EET to GO via nanowires.

To quantify the density of electrons due to EET, we measured EFM phase shift ($\Delta\Phi$) as a function of different tip biases (V_{EFM}) to separate electron contribution ($\Delta\Phi_Q$) from capacitive contribution ($\Delta\Phi_C$) using the following relation: $\Delta\Phi = \Delta\Phi_Q + \Delta\Phi_C = AV_{EFM} + BV^2_{EFM}$ (see methods for details). Notably, the electron density of reduced GO (Fig. 3.3h) correlated with filament conductivity (Fig. 3.3i). Our results thus show that EET is proportional to filament conductivity and cells use both OmcS and OmcZ nanowires for EET to electrodes.

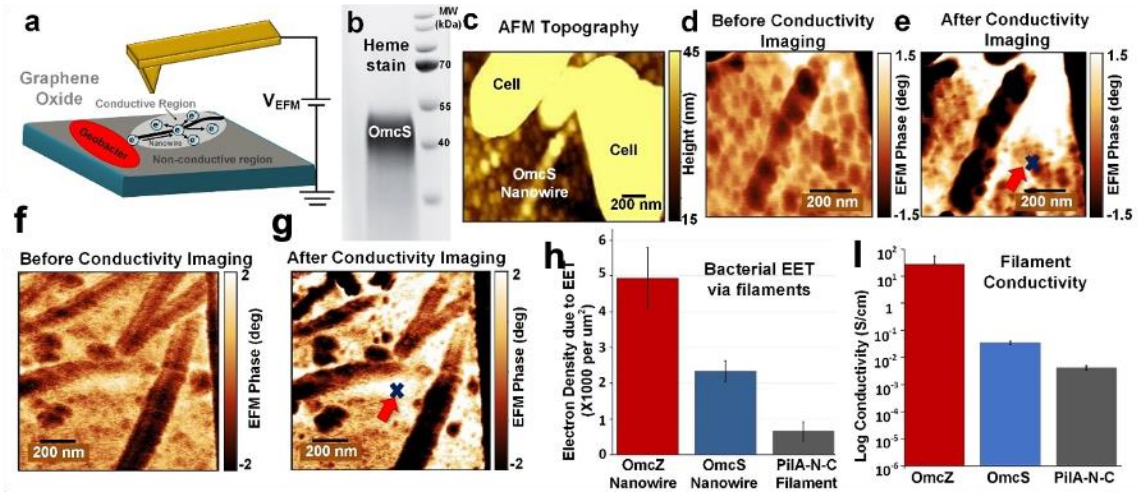

Figure 3.2: Quantitative imaging reveals bacteria using cytochrome nanowires, not pili, to transfer electrons to electrodes.

a, Schematic of Electrostatic Force Microscopy (EFM) for cells reducing Graphene Oxide via EET. **b,** Protein gel of CL1 cells showing a single band of OmcS. **c,** AFM images of *G. sulfurreducens* CL1 cells that overexpress OmcS nanowires[40]. EFM phase images **d,** before **e,** after and similarly **f,** before **g,** after conductivity imaging using charge injection into GO at a location shown by a blue cross and red arrow for OmcS nanowires. (See extended data Fig. 3 for similar imaging for OmcZ nanowires and pili). White represents the conductive region formed by EET **h,** Comparison of electron density per reduced electrode area formed by EET via filaments. Error bars, s.e.m (n=5 for OmcZ and OmcS nanowires, n=4 for pili). **i,** Conductivity of individual filaments. Error bars, s.e.m (n=3).

3.5.3. Bacteria use OmcS nanowires to transfer electrons to Fe(III) oxide.

To evaluate the role of pili filaments and OmcS nanowires in the EET to Fe(III) oxide, we grew *pilA-N* mutant strains using Fe(III) oxide as the terminal electron acceptor. We found that aromatic mutations in *pilA-N* (Aro5), or replacing PilA-N-C with pilins from *G. uraniireducens* (*Gs-Gu*) and *P. aeruginosa* (*Gs-Pa*), cause defects both in EET to Fe(III) oxide and the production of OmcS (Fig. 3.4b), which are restored in the presence of PilA-N-C (Fig. 3.4a,c). Notably, we found a strong correlation (R^2= 0.96) between the amount of OmcS and Fe(III) oxide reduced by cells because of EET (Fig. 3.4c). Based on these results, showing that the abundance of OmcS regulates EET to Fe(III) oxides, we developed a model of EET (Fig. 4d) which eliminates the need for monomeric OmcS or pili used in previous models[135,136], which are found to be absent from the surfaces of bacteria[115,137].

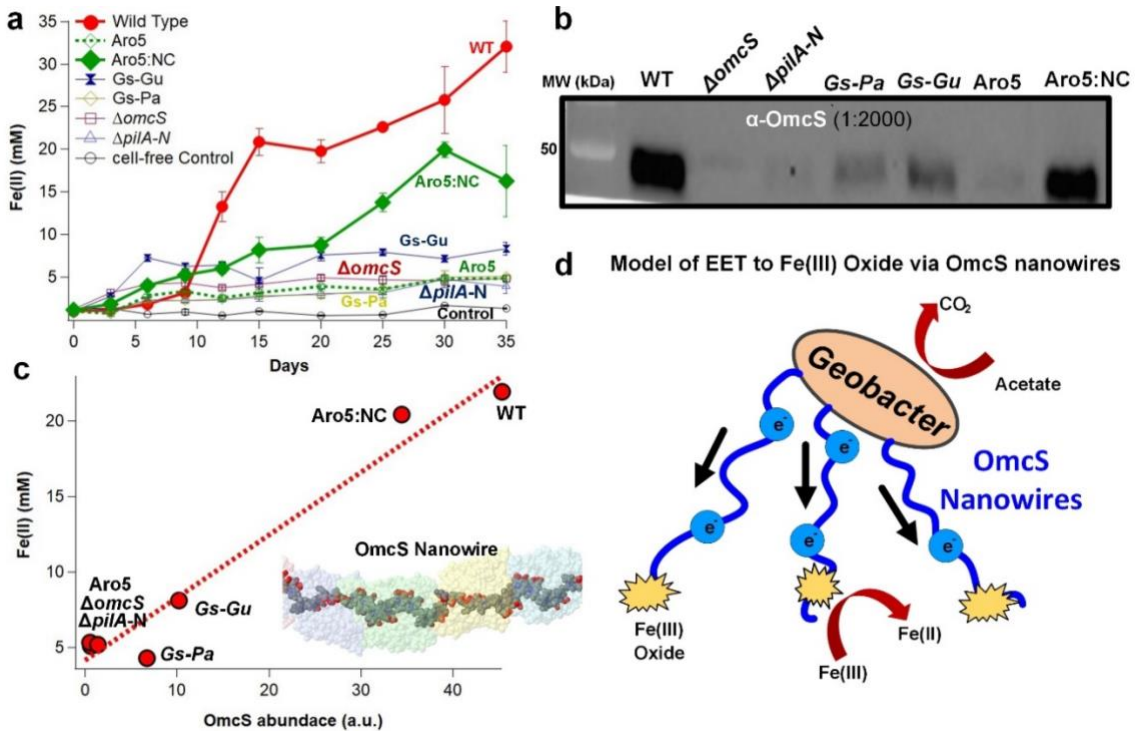

Figure 3.3: Bacteria use OmcS nanowires to transfer electrons to Fe(III) oxide.

a, EET to Fe(III) oxide over days for various strains. Error bars, s.e.m. (n=3) **b,** Anti-OmcS immunoblot of cells grown on Fe(III) oxide. **c,** EET to Fe(III) oxide is correlated with OmcS abundance. **Inset:** OmcS nanowire structure (PDB ID: 6EF8). **d,** Model of EET on Fe(III) oxide.

3.5.4. Cells specifically produce OmcS nanowires to reduce Fe(III) oxide.

To probe the role of filaments in EET, we grew *G. sulfurreducens* using insoluble Fe(III) oxide as the sole electron acceptor as previously described[144,145]. AFM imaging showed the sizes of Fe(III) oxide nanoparticles as expected[146,147] and transmission electron microscopy- energy dispersive X-ray analysis (TEM-EDX) confirmed their iron content (Extended Data Fig. 4).

AFM combined with biochemical analysis revealed that when grown on Fe(III) oxide, cells produced abundant filaments (Fig. 3.5a-d) with a height and a helical pitch that matches the atomic structure of OmcS nanowires[46] (Fig. 3.7a), rather than pili as previously proposed[21]. Bound Fe(III) oxide nanoparticles were interspersed along the length of the nanowires, and did not just accumulate at their ends (Fig. 3.5b), suggesting that electrons might move both axially and laterally through the nanowires. In contrast, very few OmcS nanowires were found during growth with the soluble electron acceptor fumarate (Fig. 3.5f-g), demonstrating that cells specifically produce OmcS nanowires to reduce insoluble Fe(III) oxide because EET via the nanowires is not required for intracellular respiration using soluble fumarate. Mass spectroscopy confirmed that OmcS is the only filament-forming protein abundant in our samples (Table 3.3e). Furthermore, WT cells showed approximately 6 times more efficient reduction of Fe(III) oxides than *ΔomcS*, highlighting the critical role of OmcS nanowires in EET to Fe(III) oxides (Fig. 3.4a).

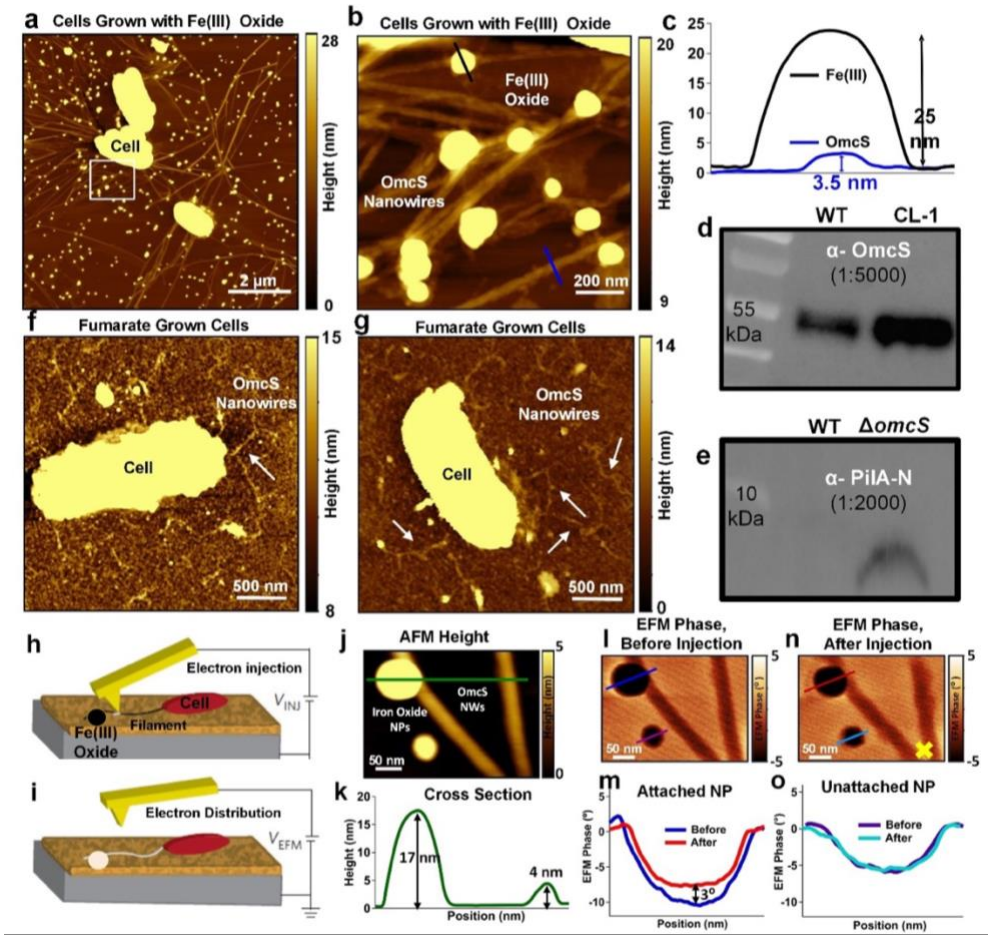

Figure 3.4: Direct imaging reveals that bacteria use OmcS nanowires to transfer electrons to Fe(III) oxide.

AFM image of cells grown on **a-b,** Fe(III) oxide and **f-g,** fumarate. **c,** AFM Height profile of Fe(III) oxide and OmcS nanowires at locations in **b. d,** anti-OmcS and **e,** anti-PilA-N immunoblots of three *G. sulfurreducens* strains grown on Fe(III) oxide. **h-i,** Schematic of EFM. **j-o,** Imaging ET from OmcS nanowire to Fe(III) oxide nanoparticles. Only nanowire-attached nanoparticles show ET. Electrons were injected at a location shown by yellow cross. (V_{EFM}=-3V), yielding a brighter filament image upon charge injection).

3.5.5. Direct imaging of Fe(III) reduction via OmcS nanowires.

To visualize electron transfer from intact OmcS nanowires on bacterial surfaces to Fe(III) oxide nanoparticles, we quantified the change in the charge state from Fe(III) to Fe(II) upon reduction using our previously established EFM-based approach[143] (Fig. 3.5h-i). Similar to imaging charge in bacterial filaments and other nanostructures in previous work[143], we operated EFM in lift mode that moves the tip ~20 nm away from the surface, allowing to measure only long range electrostatic forces to map the initial charge states (before charge injection) of the OmcS nanowire and nanowire-attached Fe(III) oxide nanoparticle using a tip voltage maintained at V_{EFM} = -3V, a voltage typically used for imaging electrons in nanostructures[143]. Next step, the lift height of the EFM cantilever was lowered closer to the nanowires and the tip voltage was pulsed at an electron injection voltage of V_{INJ} = 10V, a voltage typically used for injecting the electrons, every 2 seconds, in bacterial nanowires and shown to cause no measurable damage to nanowires while maximizing the EFM signal[143]. We injected charges at a single point by gently touching the filament (Fig. 3.5n yellow cross) and visualized the propagation of injected charges through another EFM scan in the lift mode under the same experimental conditions with the same tip used before charge injection.

We have previously demonstrated the ability of EFM to image and quantify the electron transfer in *G. sulfurreducens* filaments[143]. However, the identity and physiological role of the filaments is unknown and EET via filaments has not been established. Here we demonstrate that electrons injected into the OmcS nanowires propagate along the nanowire and then accumulate in Fe(III) oxide, as evidenced by the change in the EFM phase shift

in the OmcS nanowire network and the attached Fe(III) oxide, and no change in nanowire topography (Fig. 3.5l-o). Our series of control experiments confirmed that electron transfer is specific to nanowires. For example, there was no significant change in the EFM phase of the isolated nanoparticle nor in the contact with the OmcS nanowire (Fig. 3.5n-o), confirming that the substrate or AFM tip conditions do not influence the EFM response, and the observed response is solely due to electron transfer (see Methods for details). These results show that the OmcS filaments function as nanowires to transfer electrons directly to mineral particles for dissimilatory Fe(III) reduction.

3.5.6. Point mutations in *pilA-N* affect mechanical stability of pili and cause differential secretion of nanowires.

To further understand the OmcZ secretion defect due to *pilA-N* mutations, we grew additional *pilA-N* mutant strains using electrodes as the sole electron acceptors (Fig. 3.11a). Substituting aromatic residues in *pilA*-N affected EET (Figs. 3.2b, 4a), which was previously explained by a change in pili conductivity[131]. However, how these mutations affect the pilus stability, the secretion of cytochrome nanowires, and their structure was not examined.

We found that these mutations affect the computed mechanical stability of pili (Fig. 3.11b-e). Aro5 pili, with the fewest aromatic amino acids, showed the lowest stability, whereas *G. metallireducens* pili, with the highest amount of aromatic amino acids, showed the highest stability among the examined pilins. Our findings are consistent with studies in

other bacteria showing that the stacking of these aromatic residues is critical for the pilus' stability[71].

We further found that the mechanical stability of pili correlates with their ability to secrete OmcZ. Strain Aro5 secreted the lowest amount of OmcZ whereas the strain with *G. metallireducens* pili secreted the highest amount of OmcZ (Extended Data Fig. 5f, Table 1f). Wild-type pili showed stability and OmcZ secretion intermediate to Aro5 and *G. metallireducens* pili.

3.5.7. Truncation in PilR increases OmcZ nanowire production 3-fold.

The strain with the last two aromatic residues in PilA-N substituted by tryptophan (hereafter, Trp)[148] produced more OmcZ filaments (Fig. 3.11f and Table 3.1f). These results are consistent with prior results using mass spectrometry, immunoblotting, and immunogold labeling to demonstrate that Trp pili increase the secretion of OmcZ nanowires by more than 3-fold[48]. However, Trp pili showed computed mechanical stability similar to wild-type pili (Fig. 3.11b-e).

To elucidate the unexpected correlation between pilus stability and cytochrome secretion in G. sulfurreducens, we conducted whole genome sequencing of WT and PilA mutant strains. Our analysis revealed a single point mutation only in the Trp strain, resulting in a deletion in the gene encoding PilR, but no mutations in the *pilA-N* or *pilR* sequence of the WT or Aro5 strains. PilR regulates the expression of genes involved in the synthesis of pili and cytochromes in *Gs* through a DNA binding domain[149]. The mutation in the gene led to a frame shift changing the amino acids starting at position 334, and

introduced a stop codon at position 342, resulting in a truncated PilR lacking the helix-turn-helix domain required for DNA binding (Fig. 3.12). Notably, similar truncation is reported to overexpress nanowire-forming OmcS[109]. Our findings demonstrate that this truncation in PilR leads to an overproduction of OmcZ nanowires in the Trp strain during EET (Fig. 3.11f and Table 3.1f) explaining why it was previously believed that Trp-strain purified filaments showed a higher conductivity compared to WT purified PilA filaments. These experiment suggest a regulatory role of PilR in nanowire secretion in *Gs.*

3.5.8. Point mutations in *pilA-N* have no effect on the cytochrome nanowire structure.

To evaluate whether cytochrome nanowire structure is affected by the *pilA-N* mutations, we used cryo-EM to determine the structure of filaments purified from tryptophan-substituted and Aro5 mutant strains grown under the same EET conditions. The WT OmcS model[46] can be readily docked into the electron density map for filaments from the Trp or Aro5 strains, and the different maps showed no significant differences among the three cryo-EM maps (Fig. 3.11g). These structural comparisons establish that OmcS nanowires maintain the same structure as WT regardless of the mutations of PilA-N. Thus, *pilA-N* mutations alter the structure of the PilA filament that could disrupt the interaction between PilA-N, PilA-C and other accesory proteins required for pilus assembly. Additionally, OmcZ nanowire production and, therefore EET, is also increased due to the higher abundace of said nanowire in these *pilA-N* mutants, but they do not alter OmcS nanowire structure. Importantly, identical nanowire structures with similar conductivity

produced by these mutant strains suggest that prior studies measured cytochrome filaments rather than pili.

3.5.9. Cap protein PiY1-2 is required for the secretion of OmcZ nanowires and thereby EET.

Genetically modified pili showed mechanical stability proportional to the abundance of aromatic residues (Fig. 3.11a-e). Except for the strain with tryptophan-substituted pili, the mechanical stability of pili correlated with the abundance of OmcZ nanowires secreted by the strains (Fig. 3.11b). These results suggested that mechanical properties of pili are important for the secretion of cytochrome nanowires.

Based on this analysis, heterologously expressed pili from *P. aeruginosa* and *G. uraniireducens* are expected to show higher mechanical stability than *G. sulfurreducens* pili[115]. Despite higher stability, these pili failed to secrete OmcZ (Fig. 3.2c) and OmcS (Fig. 3.4b).

To understand the cause underlying this secretion defect, we used imaging, mass spectrometry, and immunoblotting to analyze the role of PilY1 which caps T4P and is known to interact directly with minor pilins[150-152]. PilY1 is required for interaction of pili with other proteins during bacterial adhesion and surface sensing[150-152]. The *G. sulfurreducens* genome shows two sets of minor pilin genes, with each gene cluster encoding for a unique PilY1 protein, annotated as PilY1-1 (GSU 1066) and PilY1-2 (GSU 2038). The second minor pilin gene cluster is close to that encoding the T4P assembly

components PilMNOPQ, and exists in the same transcript as revealed by RT-PCR[153]. Using mass spectrometry, we found that PilY1-2 was produced by wild- type cells along with the proteins forming T4P assembly components as well as the minor pilin PilW-2 (Table 3.5a). We further found that PilY1-2 becomes more abundant when pili are displayed on the surface of *G. sulfurreducens* Δ*omcS* cells (Fig. 3.6a-d, Table 3.5b). In contrast, we found that heterologous expression of the pilin genes of *P. aeruginosa* (*Gs-Pa*) and *G. uraniireducens* (*Gs-Gu*) into *G. sulfurreducens* also leads to abundant surface-displayed pili as visualized by both TEM (Fig. 3.6a-c) and AFM (Fig. 3.13) in agreement with previous immunogold-labeling studies[75]. Despite this pili abundance, PilY1-2 was far less abundant in these strains (Fig.3.6d, Table 3.4).

To directly evaluate the role of PilY1-2 in nanowire secretion and EET, we disrupted both *pilY1-1* and *pilY1-2* in Δ*omcS* strain that shows pili on the surface (Fig. 3.5a). Only the disruption of *pilY1-2* suppressed the secretion of OmcZ nanowires and thereby, EET (Fig. 3.5e-f).

These results collectively suggest that PilY1-2 could be serving as a cap for *G. sulfurreducens* PilA-NC pili (Fig. 3.6e). The lower abundance of PilY1-2 in heterologous pili in strains *Gs-Pa* and *Gs-Gu* could also explain to why these strains exhibit a deficiency in secretion of nanowire-forming cytochromes OmcZ (Fig. 3.2c) and OmcS (Fig. 3.4b) during EET as the cap protein might not be able to bind to the filament and recognize the nanowire monomers for their proper translocation and assembly.

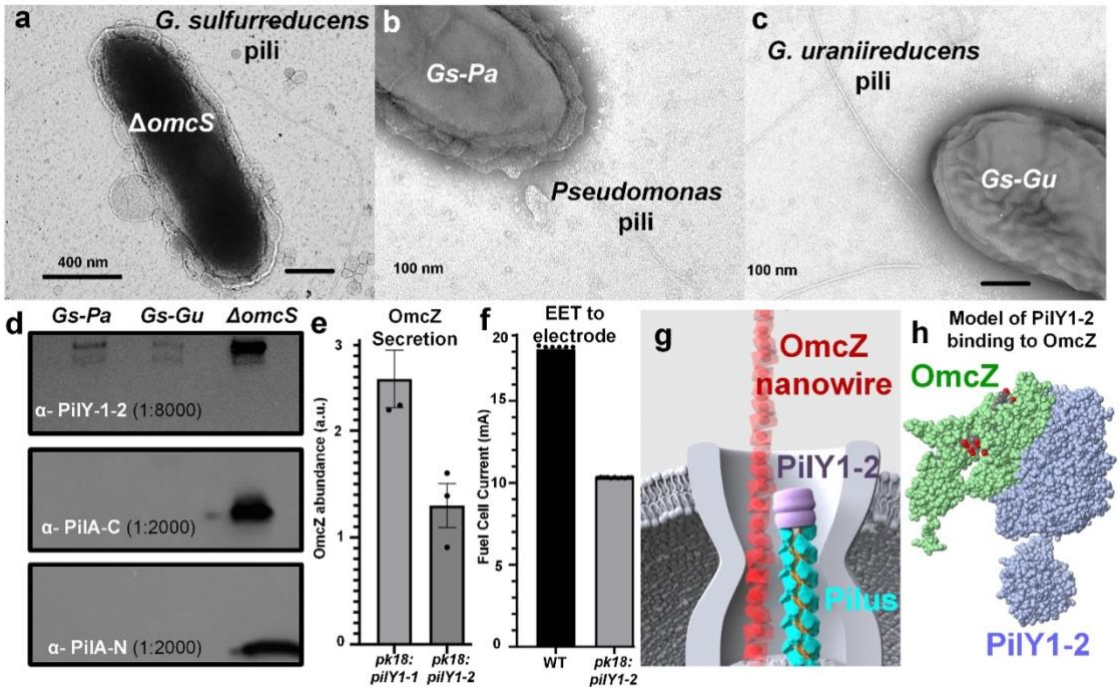

Figure 3.5: Pilli cap protein PilY1-2 is required for bacterial secretion of OmcZ nanowires, and thereby EET to electrodes

TEM images of *G. sulfurreducens* cells producing **a,** PilA-N-C pili **b,** *P. aeruginosa* pili and **c,** *G. uraniireducens* pili. **d,** Immunoblot of purified pili filaments with anti-PilY-1-2, anti-PilA-N and anti-PilA-C antibodies. Disruption of *pilY1-2* suppresses **e,** secretion of OmcZ nanowires and **f,** EET to electrode. **g,** Model of pili using PilY-1-2 cap for secretion of cytochrome nanowires. **h,** AlphaFold model of PilY1-2 (blue) binding to OmcZ (green). Hemes are in red. (See SI for the PDB file).

3.5.10. GspD porin for Type 2 secretion endopili, but not the PilQ porin for Type 4 pili, is required for the secretion of OmcZ nanowires and thereby EET.

Disruption of *pilQ*, a porin for type 4 pili[77], did not suppress bacterial EET, substantially (Fig. 3.6a, Fig. 3.7c), further suggesting that surface-displayed type 4 pili are not required for bacterial EET. Thus, our studies show that *G. sulfurreducens* do not produce type 4 pili and these pili do not serve as nanowires. Surprisingly, disruption of *pilQ* had no effect on secretion of OmcZ nanowires (Fig. 3.6b), suggesting that nanowires also do not use Type 4 pili system for their secretion.

In contrast, disruption of *gspD* (Fig. 3.7b), a porin for type 2 secretion endopili[154] (also called pseudopili), along with *gspEF,* suppressed both bacterial EET (Fig. 3.6a) and OmcZ secretion (Fig. 3.6b, Fig. 3.7c). The known diameter of GspD porin is 7.5 nm, which is sufficiently large to accommodate both PilA-N-C pili (~ 6 nm) and cytochrome nanowires (~2.5-4 nm). On the other hand, our *gspG* disruption strains, T2SS endopili, showed no OmcZ nanowire secretion defect (Fig. 3.7b). This suggest that the T2SS endopili is not involved in the translocation of OmcZ nanowires.

These studies suggest that *G. sulfurreducens* pili are a new class hybrid Type 4-Type-2 secretion endopili that use Type 4 pilus machinery for assembly but Type 2 pilus machinery for nanowire secretion. These findings are consistent with *G. sulfurreducens* pili showing the unique heterodimeric structure, localization, stability and function akin to Type 2 secretion endopili[115]. These results are also consistent with phylogenetic analysis indicating that *G. sulfurreducens* pili are intermediate between Type-4 and Type-2 pili[115].

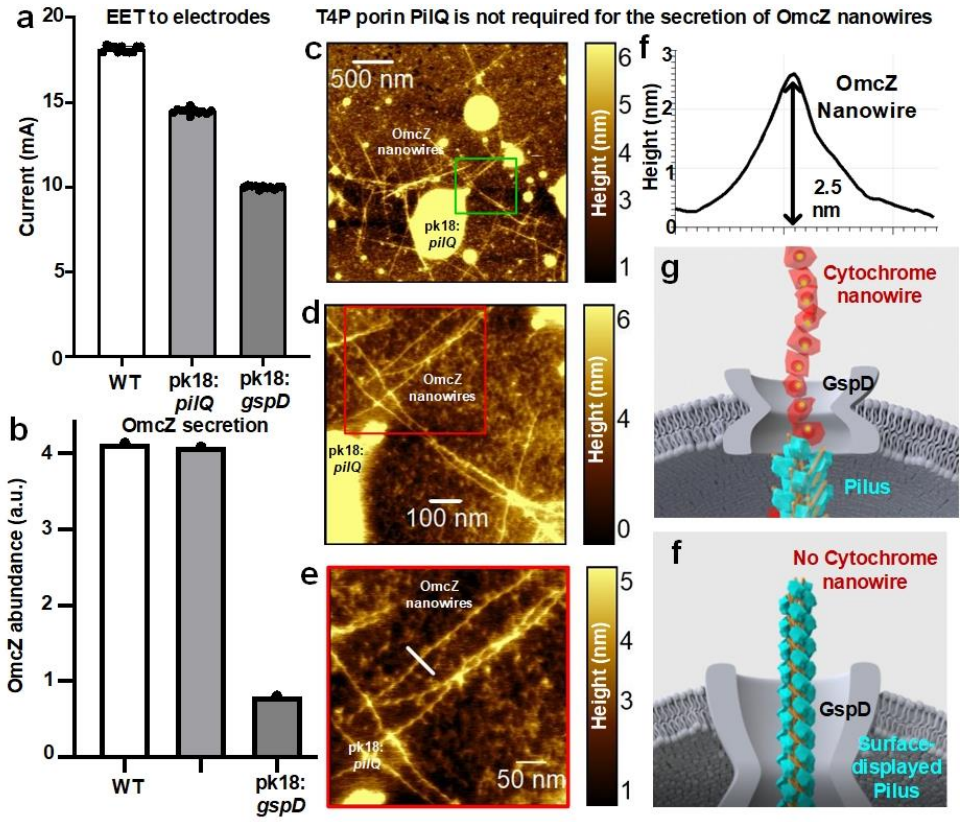

Figure 3.6: GspD porin for Type 2 secretion endopili, but not the PilQ porin for Type 4 pili, is required for the secretion of cytochrome nanowires and thereby EET. Disruption of *gspD*, but not *pilQ*, suppresses **a,** EET to electrode due to defect in secretion of **b,** OmcZ nanowires. **c-e,** AFM images of *pilQ*-disrupted cells producing OmcZ nanowires with corresponding enlarged images at locations show in squares. **f,** AFM height profile of OmcZ nanowires at location marked in in **e**. Model of pili using type-2 secretion system porin GspD for **e,** secretion of cytochrome nanowires and **f,** extension to cell surface in the absence of cytochrome nanowires.

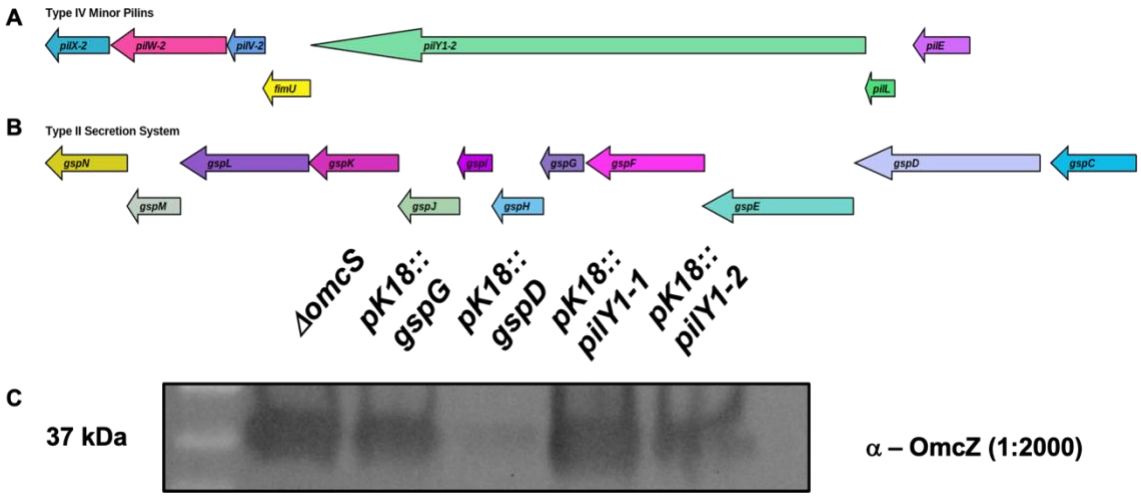

Figure 3.7 : Gel showing *pilY*1-2 and *gspD* are required for OmcZ secretion.

Genomic organization of **a,** *pilY*1-2 in Type-4 pili and **b,** *gspD* in Type-2 secretion endopili **c,** OmcZ immunoblot showing lack of OmcZ secretion in strains lacking *pilY1-2* and *gspD*

3.6 Discussion

In summary, our studies help resolve a long-standing controversy about the identity of microbial nanowires. Correlating genetic and biochemical analysis with EFM imaging at the single-cell level, we provide direct evidence that *G. sulfurreducens* uses OmcS and OmcZ nanowires for EET to Fe(III) oxide or electrodes, rather than pili. Our studies suggest distinct physiological roles for these two nanowires. We find that bacteria use both OmcS and OmcZ nanowires for extracellular electron transfer to electrodes, highlighting the importance of cytochrome nanowires in electricity production. These findings explain previous genetic studies where current production deficiencies were linked to pili and not cytochrome-forming nanowires. Deletion of *omcS* inhibits electricity production during the early stages of biofilm growth[49,155], while deletion of *omcZ* precludes the formation of thick, high-current-density biofilms[125]. Furthermore, in wild-type biofilms, OmcZ accumulates near the electrode whereas OmcS is distributed throughout the biofilm[156].

Based on all these findings, we tested a new model that OmcS nanowires are involved in biofilm growth during early stages whereas OmcZ nanowires help bacteria form 100 µm-thick biofilms due to their high conductivity[52] (Fig. 3.1e). In previous studies, the role of OmcS as nanowires was overlooked because Δ*omcS* biofilms were conductive[49], and produced high current densities in microbial fuel cells when grown over prolonged periods[49,157]. Our research suggests that cells may compensate for the loss of OmcS nanowires during the later stages of thick biofilm growth by producing more OmcZ nanowires in response to the electric field present in current-producing *G. sulfurreducens* biofilms[48]. This electric field is maximal near the biofilm-electrode interface and decreases

away from the electrode[158]. Therefore, OmcZ expression will be maximal at the interface. This may explain the maximum accumulation of OmcZ[133] and the highest metabolic activity[134] observed near the biofilm-electrode interface.

OmcS is also essential for Fe(III) oxide reduction[124] and DIET between *Geobacter* co-cultures[53,109], with cells connected via filaments that can be labeled by OmcS antibodies. Analysis of such anti-OmcS-labeled filaments revealed a structure similar to OmcS nanowires[46]. *G. sulfurreducens* may use OmcS nanowires to transfer electrons to Fe(III) oxide and to accept electrons from *G. metallireducens*[52]. The imaging methods presented here will help in identifying the electrical connections and pathways for interspecies electron transfer.

For EET, *Shewanella* uses monomeric multiheme cytochromes with a region of positive charge that is complementary to the negatively-charged Fe(III) oxide surface[159]. In contrast, the OmcS nanowires allow Fe(III) oxide nanoparticles to bind throughout the nanowire surface (Fig. 3.4b). We observed bacterial EET both at the ends of the nanowires and in directions perpendicular to nanowires (Fig. 3.2e-f), suggesting that nanowires are capable of moving electrons both axially and laterally to maximize the reduced electrode area (Fig. 3.2e-f). This ability of nanowires to transfer electrons both axially and laterally could help bacteria increase their surface area to meet the metabolic need of accessing ~50 times their biovolume [114].

The range of microorganisms capable of EET and the variety of EET functions other than respiration, such as biomass degradation[160] and live electronics[122], likely extend

well beyond those of microbes found in soil and methane-producing environments. Microbial electrical connections may have functions other than energy exchange, possibly including interactions of microbes with plants, and pathogens with hosts. If better understood, microbial electrical connections could be harnessed for additional applications in bioenergy and biofuels, and to improve the predictive modeling of carbon cycling in diverse environments. As these imaging methods are label-free and do not depend on a specific microorganism, we expect that they will aid in future rapid and broader assessments of EET via nanowires throughout the microbial world.

3.7 Materials and Methods

3.7.1. Bacterial strains and growth conditions

The following strains used in this study were obtained from our laboratory culture collection. *Geobacter sulfurreducens* wild-type (WT) strain PCA (designated DL-1) (ATCC 51573)[161], *omcS* knock-out mutant strain[124] (designated as Δ*omcS*), strain CL-1 that overexpresses OmcS[156], *pilA-N* knock-out mutant strain [162] (designated *ΔpilA-N*), *ΔpilA-N* expressing *P. aeruginosa* pili[42] (designated *Gs-Pa*), *ΔpilA-N* expressing *G. uraniireducens* pili[41] (designated *Gs-Gu*), *pilA*-N expressing *G. metallireducens* pili (strain MP)[163], and DL-1 strains with modified aromatic residues in PilA-N where five aromatic residues are substituted to alanine[38] (designated Aro5), and tryptophan-substituted strain (W51W57, designated as Trp)[148]. All gene disruption strains were constructed using a plasmid disruption protocol as previously described[120,164]. Briefly, an external plasmid pK18mobsacB was introduced to disrupt the gene of interest. The central

region of gene of interest was cloned to the plasmid by the forward and the reverse primers (Table 3.2). The constructed plasmid was first introduced into *E. coli* S17 strain[120] using EcoRI (PD F) and HindIII (PD R) to digest and T4 ligase to ligate, which further conjugated with *G. sulfurreducens* CL1 or Δ*omcS* strain. All *G. sulfurreducens* colonies grew anaerobically on NBAF agar plate under 30 °C. A single-step recombination occurred between plasmid gene and the gene of interest with the constant supply of 200 μg/ml kanamycin, to disrupt the gene of interest. Successful disruption was confirmed by PCR.

Table 3.1: Bacterial strains used in this study.

Strain Name	**Reference**
Wild-type (WT) strain PCA (designated DL-1) (ATCC 51573)	[161]
omcS knock-out mutant strain (designated as Δ*omcS*)	[124]
strain CL-1 that overexpresses OmcS,	[156]
pilA-N knock-out mutant strain (designated *ΔpilA-N*)	[162]
ΔpilA-N expressing *P. aeruginosa* pili (designated *Gs-Pa*)	[42]
ΔpilA-N expressing *G. uraniireducens* pili (designated *Gs-Gu*)	[41]
ΔpilA-N expressing *G. metallireducens* pili (strain MP)	[163]
DL-1 strains with modified aromatic residues in PilA-N (designated Aro5)	[38]
Tryptophan-substituted strain (W51W57, designated as Trp).	[148]
E. coli S17.1	[120]
ΔomcS :pk18: pilY1-1	This study
ΔomcS :pk18: pilY1-2	This study
CL-1 *:pk18: pilQ*	This study
CL-1 *:pk18: gspD*	This study

Table 3.2: Primers for construction of plasmid disrupted strains

Name	Sequence (5’ – 3’)
gspD PD F	cggaattccGAATTCGTCCTGGACGAGCGGGTGAAGG
gspD PD R	ccaagcttAAGCTTCCCTGCGCTTGATGTTGCGGTA
pilY1-1 PD F	cggaattccGAATTCCACTGGCAGCGGTCTCGCAG
pilY1-1 PD R	ccaagcttAAGCTTCGAGGTCAGGTCGCCGCAGTTT
pilY1-2 PD F	cggaattccGAATTCGCCGCAACCATGAACGATTACTGCAT
pilY1-2 PD R	ccaagcttAAGCTTACCGATCAGGTTGACCGACTTGTCAAC

pilQ PD F	cggaattccGAATTCGAGGGTGCCCGTGTCGTACTGTC
pilQ PD R	ccaagcttAAGCTTGCAAGGCGGAAGAACTTGAAGTCCTTGA

The cultures were maintained at 30°C or at 25°C under strictly anaerobic conditions in growth medium supplemented with acetate (10 mM) as the electron donor and fumarate (40 mM) as the electron acceptor. As described previously[46], the *G. sulfurreducens* cells were grown in sterilized and deoxygenated NBAF medium[64], and 1L NBAF medium containing the following: 0.04 g/L calcium chloride dihydrate, 0.1 g /L magnesium sulphate heptahydrate, 1.8 g/L sodium bicarbonate, 0.5 g/L sodium carbonate, 0.42 g/L potassium phosphate monobasic, 0.22 g/L potassium phosphate dibasic, 0.2 g/L ammonium chloride, 0.38 g/L potassium chloride, 0.36 g/L sodium chloride, vitamins and minerals[64]. 1 mM cysteine was added as an oxygen scavenger. NBAF agar plates were prepared as previously described [144] with the addition of 1.5% agar and 0.1% tryptone. The cells were grown under nanowire-producing conditions as previously described[21], or by growing cells using anodes of microbial fuel cells as sole electron acceptors, which also necessitates nanowire production due to its inherent requirement of EET over hundreds of cell lengths[49]. All strains were stored at -80°C as 15% DMSO stocks for *G. sulfurreducens*.

Cells were first grown with fumarate before transferring in the mid-exponential phase (OD_{600} = 0.5) and into iron oxide media using freshly precipitated β-FeO(OH) (akageneite) (110 mM) as the final electron acceptor, as previously described[145]. A non-chelated mineral mix was prepared as described previously[144], without nitrilotriacetic acid (NTA). 2g/L sodium bicarbonate was used to buffer the media. 0.1 mL of the cultures were removed at regular intervals and dissolved overnight in 0.5N HCl. The Fe(III) concentration was measured with a ferrozine assay[21].

3.7.2. PilA-N-C complementation.

Aro5 *pilA-N-C* complementation was performed as previously described[144]. pRK2-Geo2i expressing *pilA-N* and *pilA-C*[59] was used to transform strain Aro5[46]. Cells were cultured as previously described with 200 μg/mL kanamycin for selection and 50 μg/mL for expression. Cells were induced with 50 μM vanillate for protein expression.

3.7.3. Cell and protein normalization.

Whole cell lysates were normalized using a BCA Protein Assay Kit (Pierce #23225). Filament preparations were normalized to cell weight. For iron oxide grown cells, 20 μL of cell lysate was loaded into the SDS-PAGE gel.

3.7.4. SDS-PAGE.

For SDS-PAGE analysis, samples were boiled for 10 minutes in 2x SDS loading buffer with β-mercaptoethanol. Samples were run for 35 minutes at 190 V in a 4-20% gradient Tricine protein gel (Thermo Fisher Scientific) Precision Plus Protein Prestained molecular weight standards (BioRad) were used to compare the molecular weight of the targeted proteins.

3.7.5. Western blot analysis.

Polyclonal anti-PilA-N (Cys-RNLKTALESAFADDQTYPPES), anti-OmcS (Cys-KNSGSYQNSNDPTAWGA), anti-OmcZ (Cys-DSPNAANLGTVKPGL), and anti-PilY1-2(C-IVTNANIKPQKRIIHIREK) were raised as previously described by LifeTein[46]. Antibodies were used at a 1:2000 dilution unless otherwise specified.

3.7.6. *G. sulfurreducens* filament preparation and characterization.

As described previously[46,48], filaments were separated from bacteria and extracted via centrifugation [148], and maintained in a 150 mM ethanolamine buffer at pH 10.5 in a manner similar to structural studies on bacterial filaments[68]. Cells were gently scraped from the electrode surface using a plastic spatula and isotonic wash buffer (4.35×10^{-3} M $NaH_2PO_4 \cdot H_2O$, 1.34×10^{-3} M KCl, 85.56×10^{-3} M NaCl, 1.22×10^{-3} M $MgSO_4 \cdot 7H_2O$, and 0.07×10^{-3} M $CaCl_2 \cdot 2H_2O$), then collected by centrifugation and re-suspended in 150×10^{-3} M ethanolamine (pH 10.5). Filaments were mechanically sheared from the cell surface using either vortexing for 1 min or a Waring Commercial Blender (Cat. No. 7011S) at low speed for 1 min, and then cells were removed by centrifugation at 13,000 X g before collecting filaments with an overnight 12.5% ammonium sulfate precipitation and subsequent centrifugation at 13,000 g for 60 minutes. Collected filaments were re-suspended in ethanolamine buffer and further purified by centrifugation at 23,000 g to remove debris, and a second 12.5% ammonium sulfate precipitation with centrifugation at 13,000 g[148]. The final filament preparation was re-suspended in a 200 µl ethanolamine buffer. Filament preparations were further passed through 0.2 µm filters to remove any

residual cells and stored at 4 °C. Cell-free filament preparations were first imaged with transmission electron microscopy to ensure sample quality.

3.7.7. Transmission electron microscopy (TEM) imaging.

Cell cultures were bloated onto previously plasma-cleaned carbon-film copper grids. Grids were negatively stained with a 1% PTA solution.

3.7.8. AFM sample preparation.

Prior to all measurements, filaments were imaged with AFM, and height measurements were performed to confirm the presence of individual filaments and to confirm their identity. For EFM and KPFM, a 20 µl buffer containing filaments was drop casted onto the mica or template-stripped gold surface (Platypus, AU.1000.SWTSG) that had been plasma cleaned for 10 minutes under medium plasma exposure, and washed with DI water.

3.7.9. AFM of nanowire- and pili-producing cells and purified filaments.

AFM experiments for height measurements were performed using soft cantilevers (AC240TSA-R3, Oxford Instrument Co.) with a nominal force constant of 2 N/m and resonance frequencies of 70 kHz. The free-air amplitude of the tip was calibrated with the Asylum Research software and the spring constant was captured by the thermal vibration method. Samples were imaged with a Cypher ES scanner using the intermittent tapping

(AC-air topography) mode. All nanowire height analyses and statistics were performed using Gwyddion[165] and IGOR Pro software (WaveMetrics Inc.). AFM images were processed using either the Gwyddion package[165] or Asylum Research software.

AFM and EFM experiments were performed using soft cantilevers (ASYELEC-01, Oxford Instrument Co.) with a nominal force constant of 2 N/m and resonance frequencies of 70 KHz. The tip was coated with Pt/Ir. The free-air amplitude of the tip was calibrated with Asylum Research software and the spring constant was captured by the thermal vibration method.

3.7.10. Synthesis of Graphene Oxide (GO).

GO was synthesized by a modified Hummer's method[166]. A known quantity (2 g) of natural graphite powder (99%, flake size 80–120 μm, Superior graphite, USA) was added to concentrated H_2SO_4 (60 mL) and placed in an ice bath. Under vigorous stirring, KMnO4 (6.0 g) was added slowly to limit the excess heating caused due to the exothermic reaction. The reaction mixture was continuously agitated for 40 min. Then, 100 mL of DI water was added, and the solution was stirred for 30 min. Another 200 mL of DI water was added and followed by a slow addition of 30 mL H_2O_2 (30%). Afterward, the solution was washed couple several times with HCl (100mL) and DI water to remove the metal ions and unoxidized graphite. The resulting mixture was sonicated for 30 min to exfoliate layers into GO. The solution was then centrifuged to remove unexfoliated layers, and was filtered and dried to obtain GO powder.

3.7.11. Electrostatic Force Microscopy (EFM).

To visualize charge propagation into GO and Fe(III) oxide and to quantify the density of mobile electrons, EFM measurements were performed as described previously [143] in a non-contact mode using a two pass technique in which the first scan provides topography whereas the second scan provides the map of electrostatic forces. To avoid any contribution from the sample topography, lift height was calibrated as described previously and oscillation amplitude was reduced to $1/10^{th}$ of the amplitude used in the surface scan[143]. This method has been demonstrated to eliminate any topographic contribution to the EFM signal[143]. For all EFM imaging, a lift height of 20 nm above the sample was used to maximize the EFM signal and avoid the topography contribution. EFM images at V_{EFM} = 0V did not yield any EFM phase signal, confirming the validity of this approach[143]. Comparison of filament topography before and after charge injection yielded similar results, confirming no change in the tip resonance frequency upon injection. All images were compared using the identical first order flattening to the raw data to remove the sample tilt and avoid any artifacts. No other image processing was applied. All EFM experiments were performed under identical environmental conditions to ensure proper comparison.

3.7.12. Electrostatic Force Microscopy (EFM) on graphene oxide (GO).

The sample was prepared by depositing graphene oxide (GO) flakes suspended in deionized water on a freshly cleaved mica surface. After washing thrice with deionized water to remove large GO particles, cells were deposited on GO and allowed to grow on

the surface overnight in an anaerobic environment. Extraneous cells and debris were washed away with deionized water. Before performing EFM, bacteria adhered to the GO flakes were visualized by imaging the topography with AFM.

EFM experiments were performed with an Asylum Cypher ES atomic force microscope following a previously described procedure[167,168]. EFM images were acquired before and after charge injection on the GO surface using tip voltages of ±3 V. To observe charge propagation in *G. sulfurreducens* filaments, charge injection experiments were performed in a manner similar to that previously employed[143], except the charges were injected into GO for conductivity mapping and not into the filament. We located individual filaments from the AFM topography. We mapped the initial charge distribution near filaments using EFM. We performed charge injection into GO using local approach-retract curves by biasing the EFM cantilever at an injection voltage V_{INJ} = +10 V with respect to the substrate. In this method, the distance between the biased EFM tip and the substrate is swept with an approach duration of 2 seconds and a retract duration of 5 seconds for a total duration of 60 seconds. We monitored the mechanical contact between the tip and the GO by measuring the cantilever deflection during the charge injection process which corresponds to a force of ~150 nN applied for 2 seconds. We kept this tip-GO contact force identical for all charge injection experiments.

3.7.13. Mobile electron density measurements.

The quantitative charge densities on the GO surface were extracted in a manner similar to the measurements on 2D materials such as pentacene[169] as described

previously[143]. We separated the coulombic ($\Delta\Phi_Q$) and capacitive contribution ($\Delta\Phi_C$) to the EFM phase shift ($\Delta\Phi$) by fitting the equation $\Delta\Phi = \Delta\Phi_Q + \Delta\Phi_C = AV_{EFM} + BV^2_{EFM}$ to the measured EFM phase shift. We used the ratio $R = (\Delta\Phi_Q)/(\Delta\Phi_C)$ to compute the charge density in filaments before and after injection. Prior work showed that the ratio R remains valid for calculating charge density from arbitrary sample and tip shapes by introducing two correction factors: the sample shape factor, $g \sim 5$ for multilayer 2D materials such as GO, and the tip shape factor, α, as 1.5 for a standard conical tip[169-171]. By extracting the parameters A and B with the following equation and using the relation $Q = e \cdot \sigma \cdot S$ where e is the electronic charge (1.6×10^{-19} C), σ is the surface charge density, and S is the area of capacitance between the tip and substrate, the charge density can be computed as:

Equation 1: Conductivity

$$\frac{A}{B} = -\frac{g}{\alpha}\frac{\sigma \cdot e \cdot z}{\varepsilon_R \cdot \varepsilon_0}$$

where z is the tip-substrate distance (20 nm), ε_R, is the dielectric constant for filament (4 as measured for proteins)[172,173], and ε_0 is the vacuum permittivity. The measured substrate potential was negligible in our measurements[169-171] because no DC bias was applied. For all quantitative measurements on each filament, the same tip was employed with the same measured spring constant and quality factor.

3.7.14. Computation of the mechanical stability of pili.

Molecular Dynamics Simulation. System setup and parameterization*:* Starting from the wild-type *G. sulfurreducens* PilA-NC filament[115] (PDB 6NEF), we constructed models of the experimentally constructed mutants Aro5 (F24A, Y27A, Y32A, F51A, Y57A)[131] and TRP (F51W, Y57W)[148]. We also constructed, by homology, the pilus filament of *G. metallireducens* (Metalli) by mutating 13 residues of the *G. sulfurreducens* PilA-N subunit (S25A, V29Q, Y32F, S37E, L43T, A46N, A50Y, F51Y, A52S, D53E, D54H, T56F, P59N) and deleting the terminal 2 residues from each PilA-N subunit[163]. The *G. metallireducens* pilus was modeled similar to the pilus of *G. sulfurreducens*. Each pili model was composed of 8 PilA-N and 8 PilA-C subunits.

Using tLEaP in the AmberTools20 package[174], hydrogen atoms were added to the pili models assuming standard protonation of titratable residues for circumneutral pH (deprotonated Asp and Glu, singly protonated His on N_ϵ, protonated Lys, Arg, Cys, and Tyr). Each structure was placed at the center of a box of explicit water with at least a 15 Å buffer region to the boundary of the box. A sufficient number of counterions were added to achieve charge neutrality. Standard proteinogenic residues were modelled with the AMBER FF14SB force field[175]. The TIP3P water model[176], and the monovalent ion parameters[177] were used to model the solution state.

Pre-production simulations. Each solvated pilus was subjected to 20,000 steps of steepest descent, followed by 80,000 steps of conjugate gradient minimization. A 10 kcal/(mol Å^2) restraint was applied to the heavy atoms of the protein backbone during the minimization. The system was subsequently heated from 0 to 300 K at a rate of 0.3 K/ps in the NVT ensemble and held at the final temperature for 1.0 ns. The restraints on the

protein backbone were reduced to 1.0 kcal/(mol Å^2) for the heating stage, except for residues 6-14, 67-74, and 128-140. An additional 99 kcal/(mol Å^2) restraint force was applied to these residues to mimic the physical constraint that would be provided by their burial in a bacterial cell membrane, as suggested from the *Orientations of Proteins in Membranes* webserver (https://opm.phar.umich.edu). All the restraints (except those mimicking membrane anchoring) were further reduced to 0.1 kcal/(mol Å^2) for a subsequent 2 ns simulation at 300 K in the NVT ensemble. The restraints mimicking membrane anchoring were increased by 0.9 kcal/(mol Å^2) so that the force applied to the selected residues was a constant 100 kcal/(mol Å^2) in all stages of the dynamical simulations. Finally, the density of the system was equilibrated over an 8 ns simulation in the NPT ensemble at 1.0 bar and 300 K. All NVT and NPT simulations (including the production-stage trajectories described below) employed periodic boundary conditions, the Particle Mesh Ewald[178] treatment of electrostatic interactions with a direct sum cut-off of 10.0 Å, the SHAKE algorithm[179] to rigidify bonds to hydrogen atoms, a Langevin thermostat with a collision frequency of 2 ps^{-1}, and an integration timestep for the Langevin equation of motion of 2.0 fs. Pressure in NPT simulations was regulated with a Monte Carlo barostat having a relaxation time of 1.0 ps. PMEMD in its CPU and GPU[180] implementations in the Amber20 package[174] was used to perform the minimization and dynamical simulations, respectively.

Production-stage simulations. The dynamics of the various pili were propagated with conventional (i.e., unbiased) MD in the NVT ensemble for 181 ns (Aro5 and WT), 155 ns (TRP), and 144 ns (*G. metallireducens*). A harmonic restraining force of 100

kcal/(mol Å^2) was applied to residues 6-14, 67-74, and 128-140 to mimic the physical constraint that would be provided by their burial in a lipid bilayer.

Relative Stability Analysis. The sum of van der Waals and Coulombic interactions among a bundle of four PilA-N subunits at the center of each filament was computed for all frames, sampled every 20 ps over the last 30 ns of each production stage simulation. For this analysis, we used the pairwise keyword in CPPTRAJ[181], which computes the pairwise non-bonded interaction energies for the selected atoms. The total non-bonded interaction energy was taken as a relative measure of the PilA-N–PilA-N interaction strength. This quantity has been proposed to be a key factor in filament stability[182].

3.7.15. Cryo-EM reconstruction of OmcS nanowires.

The structure of OmcS nanowires from the Aro5 and Trp strains was solved as described previously[46]. Briefly, the OmcS nanowires were first purified from the biofilm of strains Aro5 and Trp under the electricity-producing conditions similar to those used for wild-type biofilms. The cryo-EM sample was prepared using the same blotting condition as previously described[46]. For each sample, ~4,000 images were collected by the Titan Krios microscope equipped with a K2 summit camera and energy filter from Yale University's West Campus Imaging Core. The raw movies were first motion corrected by MotionCor 2.1[183] and ~100,000 particles were picked manually. A round of 2D classification was applied to filter particles suitable for reconstruction. These particles were combined directly to generate the 3D volume using helical reconstruction implemented in RELION[184] 2.1. The reconstructed maps were at the similar resolution. The OmcS

nanowire map from the wild-type and the map for OmcS nanowires of tryptophan-substituted and Aro5 strain showed the resolution of 3.4 Å and 3.2 Å respectively. The OmcS structure (6EF8) can be readily docked into the density without any noticeable need for refinement or structural change. To generate the difference map, the maps were first manually aligned in Chimera 1.15 and then the "vop subtract" command was used to generate the difference map. All final figures were rendered in Chimera[185].

3.8 Acknowledgements

We thank O. Francetic for helpful discussions, D. Lovley and K. Inoue for strains, Vishok Srikanth and Catharine Shipps for purifying and analyzing OmcS, and Sophia Yi for mass spectrometry and biochemical analysis. We also thank M. Rooks (YINQE) for TEM-EDX, S. Wu of Yale Cryo-EM resource facility, J. Nikolaus of Yale West Campus Imaging core for facilitating AFM imaging, and Yale Center for Genomic Analysis for whole genome sequencing. This work was supported by National Institutes of Health Director's New Innovator award (1DP2AI138259-01 to N.S.M.), NSF CAREER award (no. 1749662 to N.S.M.) and NSF-ANR award (no. 2210473 to N.S.M.). We also thank the MS & Proteomics Resource at Yale University funded in part by the Yale School of Medicine and NIH (S10OD02365101A1, S10OD019967, and S10OD018034). The funders had no role in study design, data collection and analysis, decision to publish, or preparation of the manuscript.

3.9 Supplementary

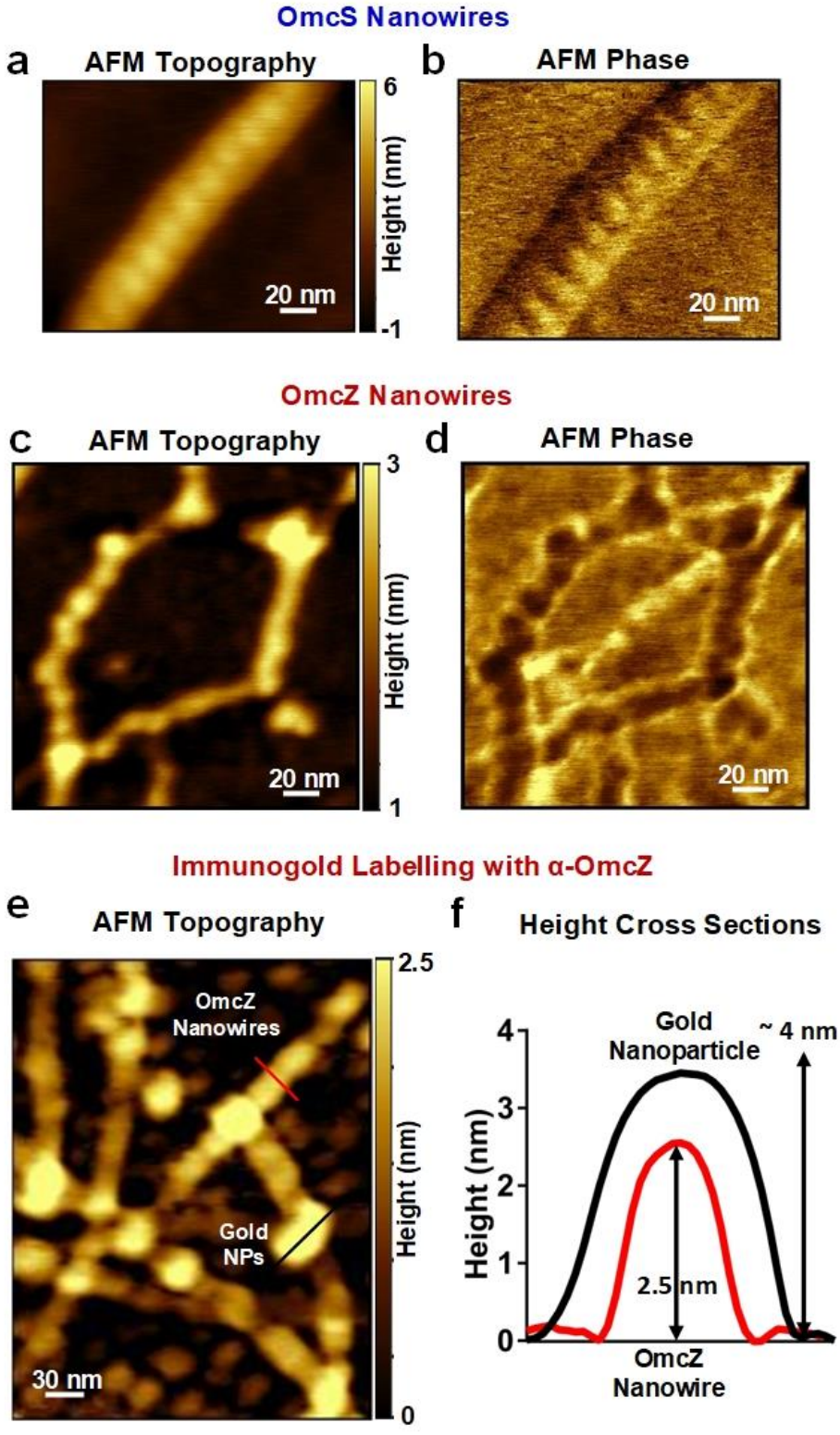

Figure 3.8: AFM imaging of filaments matches with their atomic structure.

a-b, Axial periodicity of 20 nm in OmcS is consistent with its helical pitch. **c-d,** OmcZ filament with morphology consistent with the cryo-EM structural analysis. **e-f,** Immunogold labeling with anti-OmcZ confirm filament identity as OmcZ nanowires.

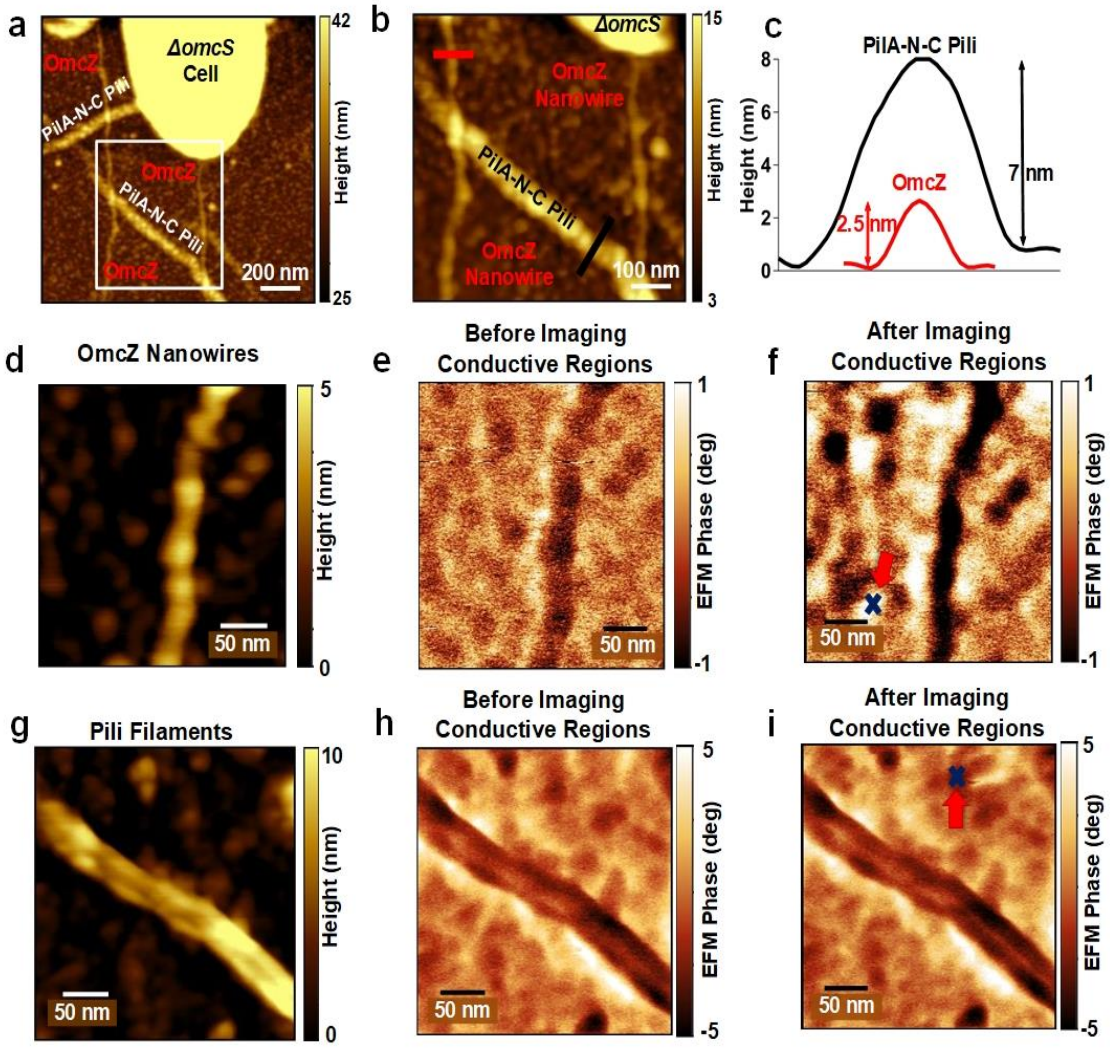

Figure 3.9: Direct imaging reveals bacteria use cytochrome nanowires to transfer electrons to electrodes rather than pili.

a, d, AFM images of *G. sulfurreducens* cells expressing OmcZ and PilA-N-C filaments respectively. EFM phase images **b, e,** before and **c, f,** after conductivity imaging using change injection into GO at a location shown by a cross and red arrow for OmcZ nanowires and PilA-N-C filaments respectively.

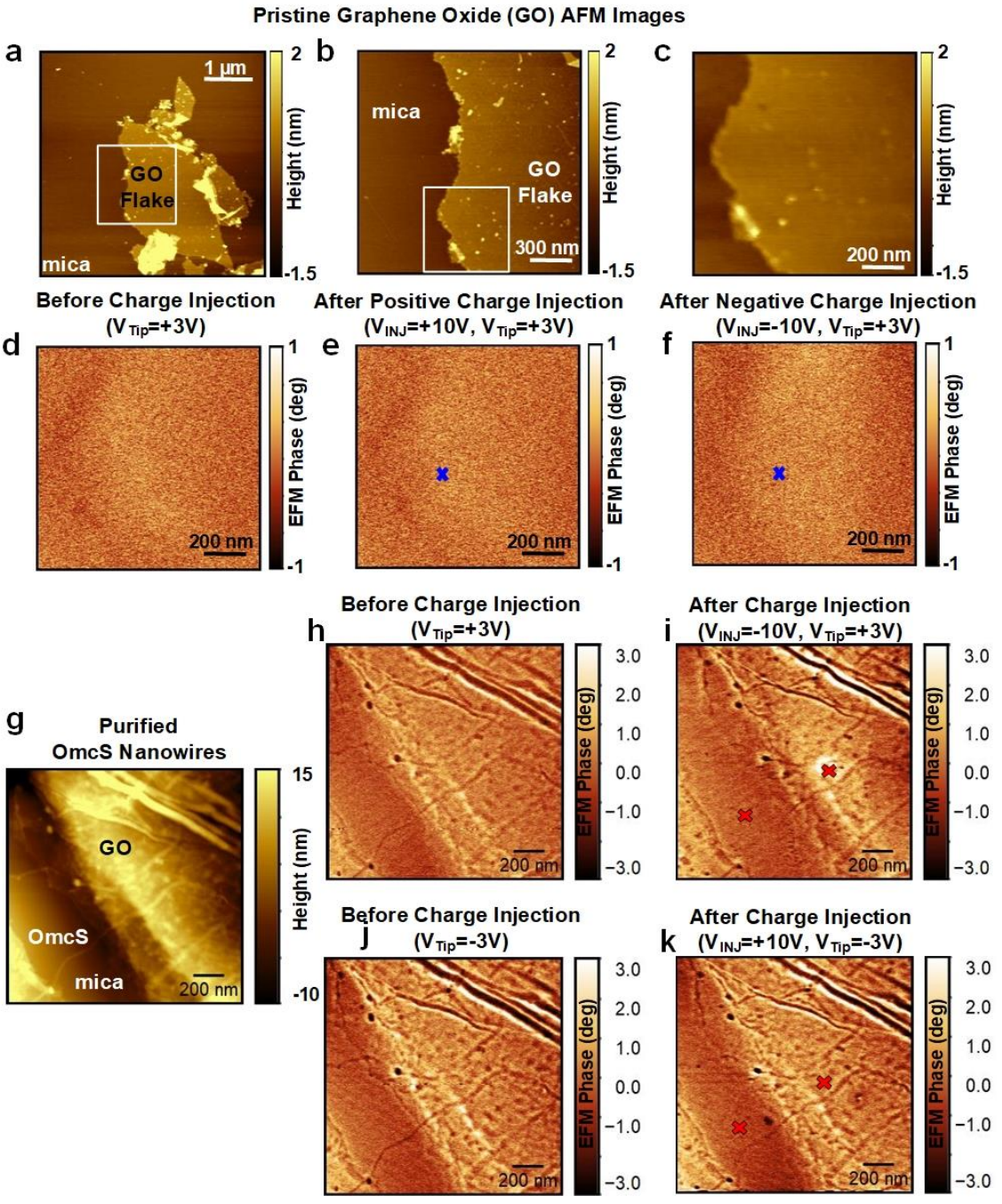
Pristine Graphene Oxide (GO) AFM Images
a
1 μm
GO
Flake
mica
Height (nm)
2
-1.5
b
mica
GO
Flake
300 nm
c
200 nm
Before Charge Injection
(V Tip=+3V)
After Positive Charge Injection
(V INJ=+10V, V Tip=+3V)
After Negative Charge Injection
(V INJ=-10V, V Tip=+3V)
d
e
f
EFM Phase (deg)
1
-1
200 nm
g
Purified
OmcS Nanowires
GO
OmcS
mica
200 nm
15
-10
Height (nm)
h
Before Charge Injection
(V Tip=+3V)
i
After Charge Injection
(V INJ=-10V, V Tip=+3V)
j
Before Charge Injection
(V Tip=-3V)
k
After Charge Injection
(V INJ=+10V, V Tip=-3V)
3.0
2.0
1.0
0.0
−1.0
−3.0

Figure 3.10: Lack of electron transfer to GO in the absence of bacteria.

a-c, AFM topography and EFM phase images of GO. d, before and e-f, after charge injection with positive and negative voltages respectively. b and c are enlarged images at locations shown in a, b respectively. g, AFM topography and EFM phase images of purified OmcS nanowires placed on GO. h-i, before and j-k, after charge injection.

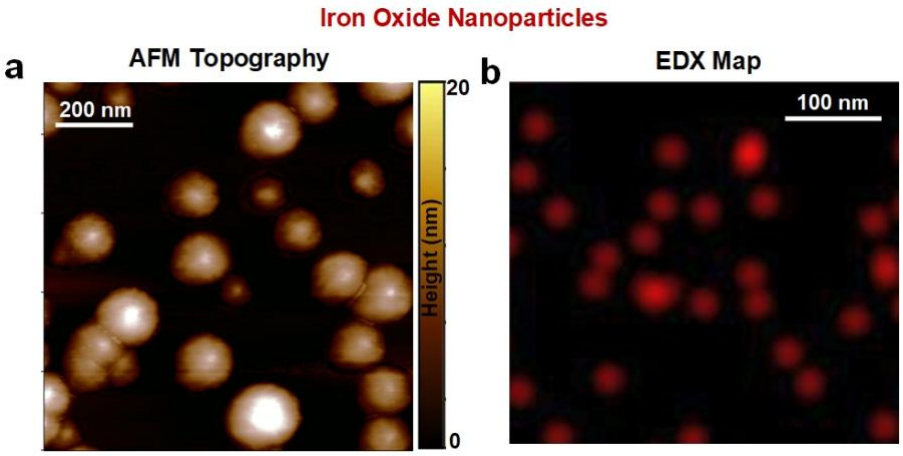

Figure 3.11: AFM and TEM-EDX imaging of iron oxide nanoparticles confirm iron composition.

a, AFM topography image of nanoparticles. Scale bar, 200 nm. **b,**TEM-EDX image of nanoparticles showing red color indicative of elemental iron. Scale bar, 100 nm.

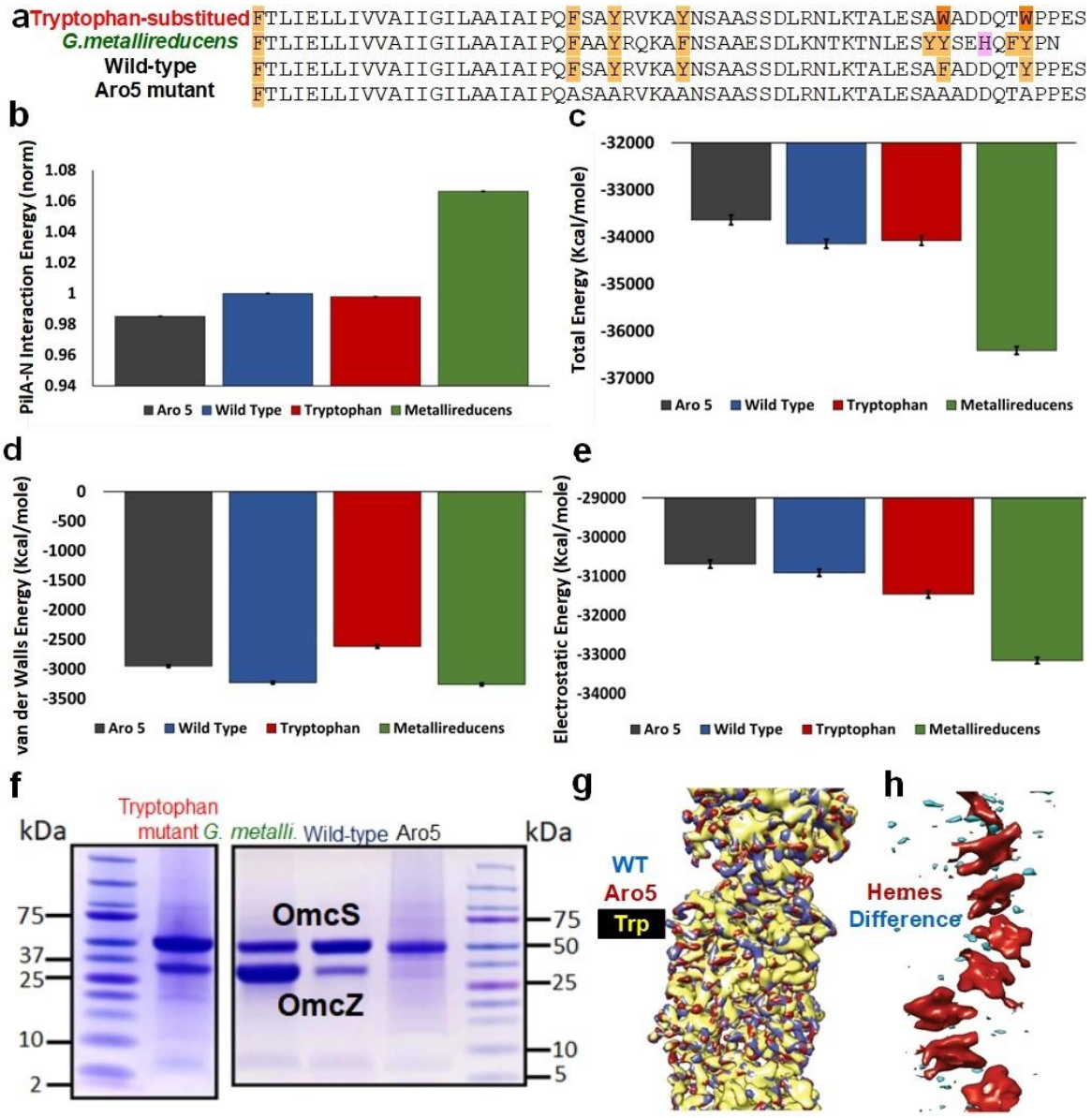

Figure 3.12: Mutations in aromatic residues in PilA-N change pili stability and affect secretion of nanowire-forming OmcS and OmcZ.

a, Amino acid sequence of different point mutants in *pilA*-N. Computed mechanical stability of pili as change in **b,** PilA-N interaction energy, **c,** total energy, **d,** van der Waals energy and **e,** electrostatic energy. **f,** SDS-PAGE gel showing different abundance of cytochromes secreted by different *pilA* aromatic mutant stains. **g,** Overlay of cryo-EM

maps obtained from wild-type (purple), tryptophan-substituted (TRP) (yellow) and Aro5 (red). **h,** Difference map (cyan) of the cryo-EM maps shown in **g** revealed no significant difference in the underlying structures. The hemes are rendered in red.

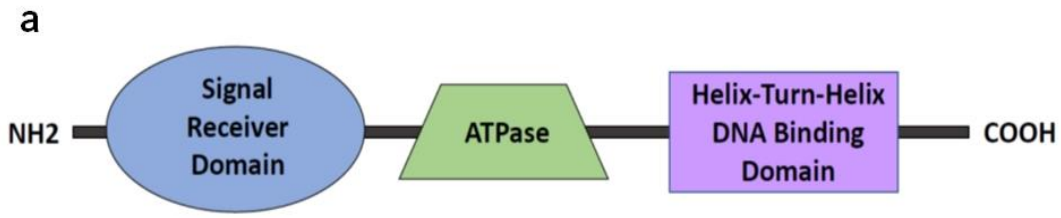

b

PilR of Wild-type Strain

MEIHVLVVDDELSMREFLAILLDREGYTVDQAASAEEALACLERKTYDLVISDVKMPGLDG
ITLLGRIKEMTPDTAVLLMTAFSTAEQAVEAMKLGAYDYIAKPFKVEEVKILARNALEKRDL
KRENLRLRQEVQERYSFSGLIGKSKKMREVYSLIEKVAPSTANVLILGESGTGKELVARAI
HYNSQRKGKPFVAVNCGAIPETLMESEFFGHKKGAFTGAVGDRAGLFEQAEGGTLFLDE
IGEVPLQLQAKLLRAIQEKEFRRVGGTLDQKADVRLVAASNRDLEEQVKEGSFREDLFYR
LNVVQVKMPPLRERGDDIPILVEHFYKKYV**QPPYSDRI**ITQGALKLLMSYGFPGNVRELEN
LVERCSVLGNREISEECLPPQLHAGKRPECGAVTECELPEEGMDLEAYLDGIEKRILLQAL
ERSGGVKKKAAELLKLTFRSFRYRLAKFGMDEE*

PilR of Trp strain

MEIHVLVVDDELSMREFLAILLDREGYTVDQAASAEEALACLERKTYDLVISDVKMPGLDG
ITLLGRIKEMTPDTAVLLMTAFSTAEQAVEAMKLGAYDYIAKPFKVEEVKILARNALEKRDL
KRENLRLRQEVQERYSFSGLIGKSKKMREVYSLIEKVAPSTANVLILGESGTGKELVARAI
HYNSQRKGKPFVAVNCGAIPETLMESEFFGHKKGAFTGAVGDRAGLFEQAEGGTLFLDE
IGEVPLQLQAKLLRAIQEKEFRRVGGTLDQKADVRLVAASNRDLEEQVKEGSFREDLFYR
LNVVQVKMPPLRERGDDIPILVEHFYKKYV**NPPTATAS***

Figure 3.13: Mutation in *pilR* of Trp strain.

a, PilR protein domains. **b,** A single nucleotide deletion in *G. sulfurreducens* from the Trp strain results in a frame shift (blue), mutations starting at amino acid 334 and premature stop codon (red) at amino acid 342, inhibiting the expression of the HTH domain of the PilR protein (shown in red in **a**).

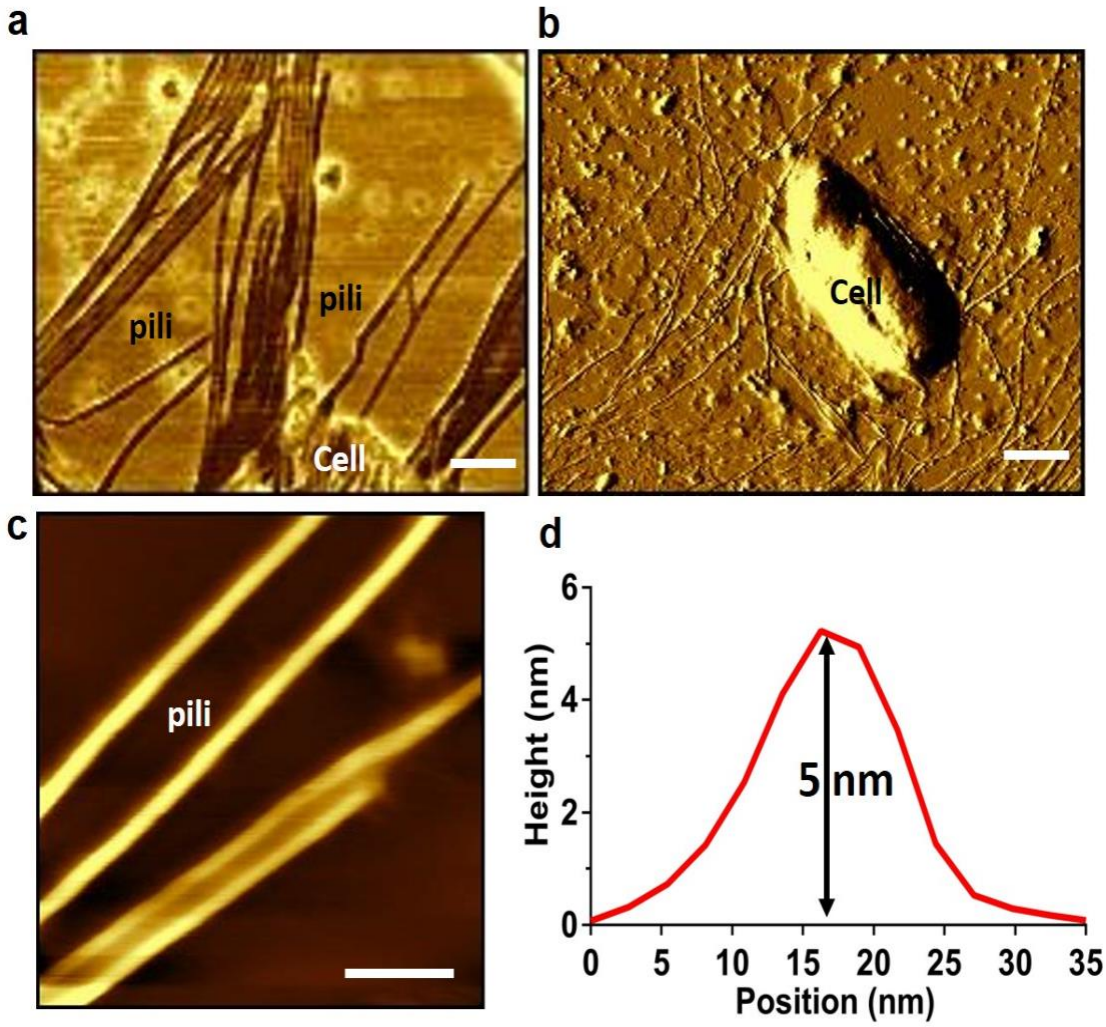

Figure 3.14: AFM images of cell-attached filaments for various strains used for EET to electrodes and Fe(III) oxide.

a, Phase image of *Gs-Pa* strain showing T4P pili of *P. aeruginosa*. **b,** Amplitude image of *Gs-Gu* strain showing pili-like filaments of *G. uraniireducens.* **c,** Zoomed height image and **d,** corresponding height profile of pili of *G. uraniireducens.* Scale bars, a, 100 nm, b, 500 nm, and c, 50 nm.

a *G. sulfurreducens* with wild-type (WT) *pilA*-N

Protein Name	MW (kDa)	Coverage (%)	Top 3 Intensity (x10^8)
OmcS	45	51	99.1
OmpJ	49	74	27.3
PilA-C	13	56	13.8
PilA-N	7	48	7.7
GltA	50	54	7.3
KorB	30	40	5.1
FrdA	71	24	4.6
OmcT	46	32	4.3
Tuf1	43	43	4.2
GSU2733	45	52	3.8
GSU3403	49	53	3.6
GSU3305	10	71	3.5
GSU0360	49	30	3.4
KorA	41	21	2.8
OmcZ	49	16	2.7

b *G. metallireducens pilA*-N (*Gs-Gm*)

Protein Name	MW (kDa)	Coverage (%)	Top 3 Intensity (x10^8)
GSU3242	8	46	209
OmcS	45	47	133
GSU2887	92	33	64.1
OmcZ	49	23	47.8
RpsC	24	63	11.3
Tuf1	43	59	8.7
RpsD	24	61	8.2
GSU1876	17	36	7.9
RplB	30	48	7
IscR-1	17	66	6.7
GSU2429	39	64	6.5

c Trptophan-subtituted *pilA*-N (Trp)

Protein Name	MW (kDa)	Coverage (%)	Top 3 Intensity (x10^8)
GSU2887	92	39	307
OmcS	45	50	197
GSU3242	8	46	149
GSU0872	16	67	143
OmcZ	49	17	140
GSU3300	107	12	60.3
GSU1876	17	62	57.7
GSU0800	29	63	49.2
LivK-1	40	77	45.3
FrdA	71	63	40
GSU3306	55	65	38.2
Tuf1	43	64	36.4
OmcC	81	27	33.7
GltA	50	56	30.4
GSU3305	10	63	29.1
LivK-2	40	65	28.3
RpsE	17	71	25.6

d *pilA*-N with 5 aromatic mutations (Aro5)

Protein Name	MW (kDa)	Coverage (%)	Top 3 Intensity (x10^8)
OmcS	45	52	963
OmcT	46	46	36.1
GSU0360	46	58	8.1
GltA	50	48	7.9
GSU3242	8	38	6.8
Mdh	34	59	6.6
DcuB	47	8	3.8
Tuf1	43	43	3.3
FrdA	71	31	3.2
RpoB	153	22	3.2
KorA	41	52	3
FrdC	24	4	2.2

e OmcS-overexpressing strain (CL-1)

Protein Name	MW (kDa)	Coverage (%)	Top 3 Intensity (x10^8)
OmcS	45	53	704
HybL	62	71	176
GSU2493	32	82	134
OmpB	140	56	99
GSU3547	24	83	72
Mdh	34	68	69
GltA	50	62	65.2
DegP	50	81	61.8
GSU2495	70	26	61.2
GSU0800	29	62	45.7
LivK-1	40	74	42.1
GSU2429	39	78	38.8
Tuf1	43	65	35

f

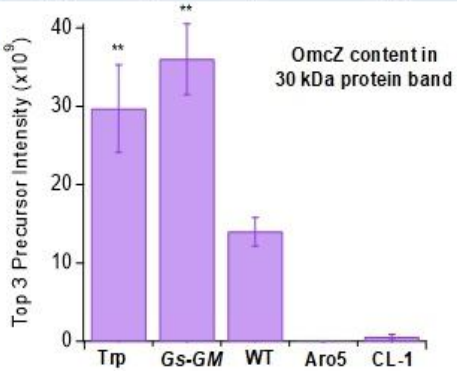

Table 3.3: Mutations in aromatic residues in PilA-N change pili stability and affect secretion of nanowire-forming OmcS and OmcZ as revealed by mass spectrometry of *G. sulfurreducens.*

a, WT, b, Trp, c, *Gs-Gm*, d, Aro5 and e, CL-1. OmcS and OmcZ proteins are highlighted in yellow. Except CL-1 which was grown on fumarate, all other strains were grown using electrodes as the electron acceptor. None of the strains show OmcE. f, Comparison of nanowire-forming OmcZ in 30 kDa protein band of the same samples used in a-e.

a ***Gs-Pa***

Protein Name	MW (kDa)	Coverage(%)	iBAQ (x10^8)
GSU3242	8	42	494
GSU0800	29	69	157
GSU3547	24	82	92.4
GSU3406	27	73	69.4
LivK-1	40	78	64.6
OmpB	140	62	52
GSU3305	10	58	49.7
GSU0210	35	72	48.4
GSU1333	17	57	47
GSU2429	39	75	41.8
LivK-2	40	73	37.5
GSU2496	65	69	34.3
GSU1395	9	11	33.5
GSU2005	42	70	26.2

b ***Gs-Gu***

Protein Name	MW (kDa)	Coverage(%)	iBAQ (x10^8)
GSU0720	17	23	106
MetY-1	47	29	106
GSU2811 (cytc)	53	32	86.3
GSU0360	46	26	78.4
GdhA	49	28	76.8
GSU0716	30	13	70
PckG	70	14	69.5
GSU3242	8	21	63.6
GSU3305	10	35	59
OmpB	140	14	44.5
Hup	10	34	40.8
MetK	43	25	39.6

c ***ΔomcS***

Protein Name	MW (kDa)	Coverage(%)	iBAQ (x10^8)
GSU3547	24	82	697
OmpB	140	66	316
PilA-N	7	49	173
GSU1395	9	11	86.3
GSU3305	10	67	75.1
PilA-C	13	46	60.3
OmcZ	49	22	58.4
GSU1945	107	39	47.3
GSU3317	37	71	33.8
HybA	33	54	32.9
GSU1844	75	23	32.6
GSU1538 (cyt c)	45	61	18
GSU3402	10	57	17.1
GSU1018	19	60	15.7
GSU1948	39	33	13.8
GSU1251	210	35	13.3
GSU2429	39	72	10.7
GSU1079	25	42	10.6
DegP	50	74	9.5
GSU3242	8	42	9.3

Table 3.4: Heterologous expression of pili from *P. aeruginosa* (*Gs-Pa*) and *G. uraniireducens* (*Gs-Gu*) inhibit secretion of nanowire-forming OmcS and OmcZ as revealed by solution mass spectrometry of *G. sulfurreducens* strains.

a, *Gs-Pa*, **b,** *Gs-Gu*, **c,** Δ*omcS* produces proteins forming pili filaments and OmcZ nanowires. Except Δ*omcS* which was grown on fumarate, all other strains were grown using electrodes. None of the strains show OmcE.

a PilY-1-2 along with Pili assembly in WT cells

Score*	Expectation	Protein Name	MW	% Coverage	EMPAI
5832	0	OmcS	45360	69	82.21
1753	0	OmpJ	48852	81.8	20.82
1740	0	GltA	49849	76.6	28.92
1709	0	FrdA	70788	62.3	10.96
1499	0	Mdh	33654	63.1	20.67
1272	2.30E-124	AcnB	91081	51.1	4.05
1149	4.10E-112	RpoB	152412	27	1.28
1093	1.70E-106	GSU0613	50522	49.3	6.3
1055	1.10E-102	Por	129500	36.9	1.64
1049	4.10E-102	PilA-N	6569	55.7	16.3
1000	3.70E-97	Unknown (GSU2733)	45316	60.8	10.29
867	6.30E-84	RpoC	155728	25.8	0.94
827	7.30E-80	Tuf1	43191	67.9	5.61
795	1.00E-76	Icd	81096	37.8	1.84
794*	1.50E-76	OmcT	45505	44.4	3.25
372	1.90E-34	PilA-C	13068	62.1	5.75
261	3.00E-23	Cyt c (GSU2887)	92184	8.1	0.23
251	3.00E-22	OmcZ	49348	21.6	0.66
235	9.70E-21	PilQ	94164	19.2	0.7
200	3.20E-17	PilC	43534	19	0.54
199	4.20E-17	Cyt c (GSU0591)	31103	18.7	0.35
156	8.30E-13	PilT-1	42753	10.6	0.44
148	5.60E-12	OmcB	77129	6	0.28
146	8.70E-12	PilY1-2	205399	6.5	0.18
145	1.10E-11	GSU2501	46112	17.4	0.5
107	6.80E-8	PilN	21072	34.6	0.81
107	7.40E-8	PilO	22035	24.2	0.53
104	1.40E-7	FrdC	24119	29.5	1.18
102	2.10E-7	GspG	16030	20.4	0.48
97	6.20E-7	PilT-4	40687	14.8	0.36
93	1.8E-6	Cyt c (GSU0274)	70214	11.5	0.43
65	0.0011	FimU	17478	16.1	0.71
64	0.0014	PilW-2	43264	7.6	0.24
63	0.0016	PilP	19412	13.2	0.62
57	0.0075	CydA	49930	5.8	0.13
55	0.012	PilR	51425	4.1	0.13

b PilY-1-2 accompanies surface-displayed pili

Protein Name	MW (kDa)	Coverage(%)	Total spectra
OmpJ	49	68	1009
PilA-C	13	80	496
RW64_10885	50	79	421
OmpB	140	56	401
GSU3547	24	84	398
GSU3403	49	65	374
PilA-N	10	37	292
GSU2733	45	64	214
GSU3401	41	72	206
GSU0360	46	69	198
GSU1252	180	49	133
GSU1251	210	34	133
ICD	81	64	126
PilY1-2	206	45	120

Table 3.5: Identification of PilY1-2.

a, WT cells producing pili assembly proteins PilMNOPQ and **b,** surface-displayed pili. Relevant proteins are highlighted in yellow.

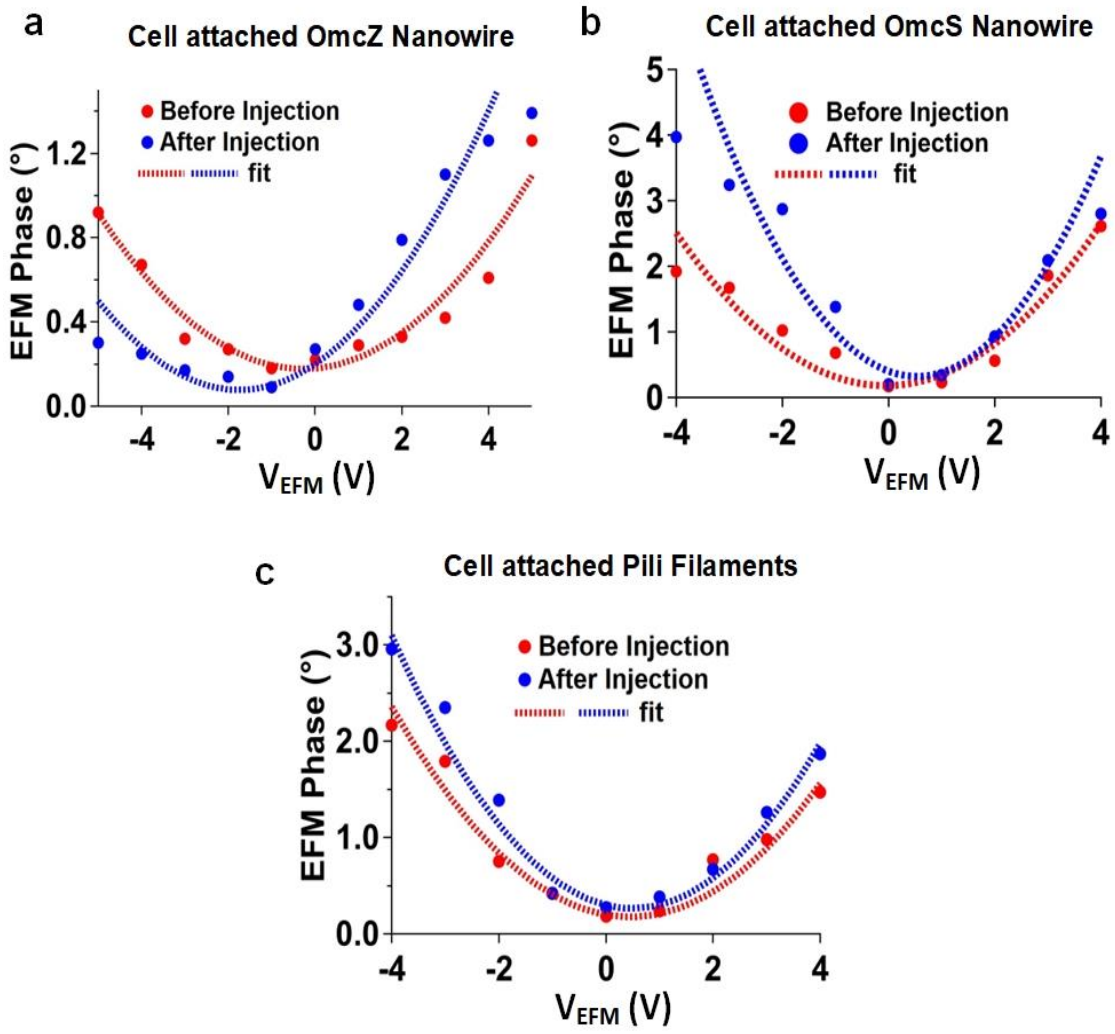

Figure 3.15: Analysis of quantitative electron density due to bacterial EET for OmcZ and OmcS nanowires and pili filaments.

Representative EFM phase shift as a function of EFM tip voltage before and after charge injection into Graphene Oxide (GO) that reveals the reduced GO pathways due to EET. Cell attached **a,** OmcZ nanowire on GO **b,** OmcS nanowire on GO and **c,** Pili filament on GO. Fitting results were obtained using equation $\Delta\Phi = \Delta\Phi_Q + \Delta\Phi_C = AV_{EFM} + BV^2_{EFM}$.

4. Interaction between PilA-N and PilA-C stabilize PilA filaments in *Geobacter sulfurreducens*

PilA-N stability is key for proper assembly of PilA-N-C filaments

Aldo I. Salazar-Morales, Matthew J. Guberman-Pfeffer, Yuri Londer, Jerry Ruvalcaba & Nikhil S. Malvankar

4.1 Author Contributions

A.I.S.-M. and J.R. carried out biochemical analyses and genetic experiments. M.J.G,-P. carried out computational analysis. Y.L. made the PilA-N-C constructs in *E.coli.* A.I.S.-M. and N.S.M conceived, designed and supervised the project.

4.2 Summary

Type 4 Pili are canonically used by Gram-negative bacteria to interact with their surroundings as it allows them to move, attach to surfaces, initiate biofilm formation, uptake extracellular DNA, and act as a virulence factor for some pathogens[22-26]. For the past decade, *Geobacter sulfurreducens* pili have been mischaracterized as a nanowire that allows *Gs* to complete its metabolic functions[21,37-39,41]. Our lab has recently identified nanowires as OmcS[44] and OmcZ[40] filaments and solved the structure which brought insight into the role of *Gs* pili[59] and solved the controversy in the field regarding the identity of

these filaments. Despite these advances in the field, the mechanism and role in stability that PilA-N and PilA-C monomers play to assemble a *Gs* PilA-N-C filament remain poorly understood. Here we used a combination of *in vivo* and *in silico* approaches to demonstrate that PilA-C stabilizes PilA-N to assemble into a filament. Furthermore, 4 Gly residues located in PilA-C likely act as hinges to allow PilA-C to wrap itself around PilA-N to form the heterodimer subunits that assemble into filaments.

4.3 Significance Statement

Geobacter sulfurreducens has been immersed in controversial discussions regarding the identity, composition and function of their pili filaments. Previous work from our lab has addressed these questions but the mechanisms through which these filaments are assembled and stabilized are still poorly understood. This work provides, for the first time, evidence to understand the molecular mechanism that allows the interaction of PilA-N and PilA-C to assemble into the building blocks to form filaments.

4.4 Introduction

Type IV filaments are comprised of thousands of subunits (PilA) capable of polymerizing and depolymerizing from the inner membrane to the extracellular environment. This canonical feature of bacteria grants them the ability to move, attach to surfaces, initiate biofilm formation, uptake extracellular DNA, and function as a virulence factor for some pathogens[22-26]. Type IV pili (T4P) share a conserved N-terminal domain that is anchored to the inner membrane where the proteolytic cleavage to form a mature

pilin and pilin-to-pilin interactions take place[26,162,186]. This region is commonly formed by a helical region with two subdomains: α1-N and α1-C which will serve as an anchor for the globular domain and form the core of the filament[25]. These globular domains at the C termini and the loops that connect both the helical core and the globular domain are far less conserved than their N terminal counterparts[24,25]. Variations in these regions allow for the T4P incredible functional diversity. Although the evolution of these regions is limited by the need of the pilins to maintain their protein-protein interactions during assembly and translocation, sequence diversity show a range of shapes and flexibility encoded in these regions[25]. Despite their thin nature (5-8 nm), these micrometer-long filaments can withstand pulling forces of >100 pN[24,26]. Filaments are assembled through protein-protein interactions between subunits. At the N termini, the F1 residue from one subunit forms a salt bridge with the E5 residue of an adjacent subunit to stabilize the hydrophobic regions of the pilin[187]. At the C termini, disulfide bridges are form between the N terminal α-helix and the globular domain at the C-termini of the protein increasing the stability of the filament[188,189].

Although T4P functions and properties are fairly conserved in bacteria, *Gs* pilus was believed to be distinctively different from othe T4P due to their alleged electroconductive properties in EET[59]. *Gs* pilus encodes for a 61-amino acid protein that shares a high degree of homology to the N-terminus of other T4P but lacks their globular domain[54]. This means that *Gs* pili only encode for the α1-N and α1-C regions present in other T4P, but lack the globular domain that is encoded by PilA-C[25].

It has been proposed that Gs pili use the aromatic residues present at the N-terminus of PilA-N in the α-1 C regions to transfer electrons during EET. Experimental evidence has shown that mutations in this alpha-1 C region and heterologous expression of other T4P directly impact Gs pili conductivity, with current production increasing or decreasing with the aromaticity of the α1-C region[21,37-39,41].

However, these experiments provided no biochemical or structural evidence to support the claim that *Gs* PilA-N pili are the *Gs* electroconductive filaments called nanowires. Liu *et al.* performed immunogold labeling on what was allegedly a PilA-N filament, where OmcS cytochrome monomers were coating the PilA-N filament[42]. This work defined the initial model in the field where PilA filaments serve as a scaffold for OmcS cytochrome monomers to facilitate EET. The disruption of the interaction between these two proteins was then proposed to explain the deficiency in current production and Fe(III) reduction[42]. Recent studies performed in our laboratory have found that: 1) nanowires are polymers of OmcS[44] and OmcZ[40] multi-heme cytochromes; 2) The predicted conductivity of the PilA-N only filament attributed to aromatic stacking is unlikely due to the > 3.5 Å spacing between aromatic residues and its lack of cofactors for electron transfer; 3) *Gs* PilA filament is composed of two proteins, the helical domain PilA-N and the globular domain PilA-C, which assemble into a heterodimer to form a filament that is involved in nanowire secretion[59].

Therefore, to study these phenomena, we have devised various strategies to gain a better understanding of the stability and dynamics of the filament. Here we combined *in*

silico and *in vivo* studies to study the role of PilA-C in pilus stability and dynamics. Our findings have shown that by disrupting the PilA-N and PilA-C interaction, PilA-N is incapable of stabilizing its hydrophobic interactions at the C terminus of the subunit. Furthermore, the computational analysis also demonstrated that PilA-N-C filaments are approximately 3.3-fold more stable than PilA-N filaments. Further MD simulations demonstrated that PilA-C is capable of moving its "flaps" to wrap itself around PilA-N. Gly residues provide the hinges localized in the globular domain of this protein with the required movement to fold themselves around the last 5 residues in the C terminus of the PilA-N subunit. Further studies will be conducted *in vivo* to study the mutation of Gly residues into Ala to test the effect of said interactions in pilus stability, dynamics, and protein-protein interactions to secrete nanowire-forming cytochromes.

4.5 Results

4.5.1. Reconstituting *Geobacter* pili in *P. aeruginosa*

Several studies have claimed to reconstitute *Gs* pili using *Pseudomonas aeruginosa*[190] and *E. coli*[191] as a chassis through the expression of the truncated *pilA-N* gene. However, structural data shows that *Gs* pili are composed of both PilA-N and PilA-C and these filaments lack key features of canonical T4P[59]. Although the work presented by Liu *et al*. shows the successful expression of *Gs* PilA-N filaments[190], our studies replicating their protocol failed to produce the same results (Figure 4.1C-D). Figure 4.1A shows the successful expression of *Gs* PilA-N in PAO1 and PAO1*ΔpilA-N* strains upon induction, but these results probably represent an extracellular heterodimer and not necessarily an assembled filament. Similarly, as discussed in Chapter 2, the expression of PilA-N does not rescue the twitching phenotype in a *ΔpilA* background. Furthermore, the expression of *Gs* PilA-N reduced motility of *P. aeruginosa*, possibily by competing for the pilus assembly machinery[35].

These conflicting results have caused a lot of controversies in the field questioning the role, composition, and interactions of *Gs* pili with extracellular electron acceptors and other proteins. Our current model contrasts with the previous conception where PilA-N filaments are coated with OmcS monomers to facilitate EET. Our model proposes that PilA-N-C filaments are used as a piston to secrete nanowire subunits (OmcS and OmcZ) to the extracellular environment. Although we know that PilA-N-C filaments are involved in nanowire translocation, little is known about the protein-protein interactions between

PilA-N and PilA-C and what role these interactions play in the structural stability of the filament and nanowire secretion.

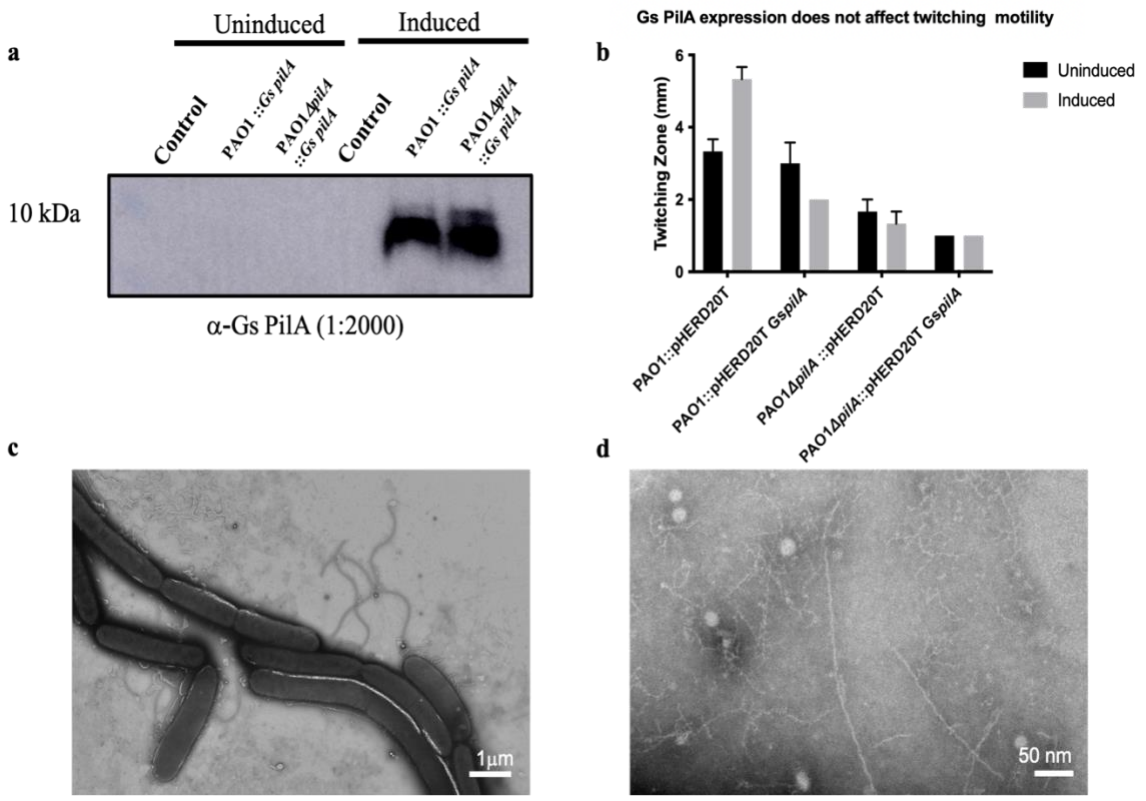

Figure 4.1 Heterologous expression of *Gs PilA* in *P. aeruginosa* (PAO1).

(**a**) Immunoblot of extracellular fractions of PAO1 strains. (**b**) Twitching motility assays show no twitching motility defect. TEM images of PAO1 cells expressing *Gs* PilA-N show *P. aeruginosa*'s flagella (**c**) and zoomed image of *P. aeruginosa* filaments (**d**).

4.5.2. Interaction between PilA-N and PilA-C stabilize PilA Filament

For over a decade, the field has been involved in a controversy regarding the nature and composition of the hypothesized "e-pili". As stated earlier, various works have studied the relevance of PilA-N in the formation of the formerly called e-pili capable of transferring electrons extracellularly[21,37-39,41,190,191], but recent work has shown that e-pili are not composed of PilA-N subunits, but are composed of the nanowire-forming cytochrome OmcS[44] and OmcZ[40,45]. Additionally, *Gs* pili are composed of the helical core PilA-N and the globular domain PilA-C[59]. Although we have explored the role of PilA-N-C filaments in EET, little is known about the protein-protein interaction properties of PilA-N and PilA-C.

To explore these interactions, we performed computational studies on a hypothetical PilA-N filament structure and compared it to the structure of a PilA-N-C filament. To test both filaments, molecular dynamic (MD) simulations were performed on filaments composed of four PilA-N-C heterodimers and four PilA-N monomers to define the minimal block used to determine the stability of the structures computationally. The energetic strength of the PilA-N – PilA-N non-bonded interactions were calculated in the presence and absence of PilA-C where an increase or decrease in energy was taken as a metric of stability or instability respectively (Fig. 4.4). PilA-N chain interactions became more stable in the presence of PilA-C when looked at electrostatic interactions, despite being relatively similar from a van der Waals energetic point of view. Therefore, these results show that the presence of PilA-C increases the stability of PilA-N-C filaments in an approximate 3.3-fold relative to PilA-N filaments as shown in Figure 4.4 F establishing

that a PilA-N-C filament is therefore more stable than a PilA-N filament. Although these studies do not provide irrefutable evidence against a PilA-N filament, they do provide insight into the plausible role of PilA-C in the stabilization of the PilA filament in *Gs.*

To experimentally test the influence of PilA-N and PilA-C in cytochrome secretion we designed three PilA-N constructs to disrupt the interaction between both of these proteins in a *ΔpilA-N*. A histidine tag was added to each of the truncated pilins to perform immunobloting analysis. As previously mentioned in Chapter 2, PilA-N is comprises two alpha-helical regions separated by a melted helix region[59]. The first construct encodes for the first 16 amino acids of the sequence and was labelled PilA-N$^{\Delta 17\text{-}61}$. This construct encodes the first melting region at the N terminus of the protein. The second construct, PilA-N$^{\Delta 27\text{-}61}$, encodes the first 26 amino acids of protein and the first helical structure and melting region. Finally, PilA-N$^{\Delta 38\text{-}61}$, disrupts the second helical structure of the pilin eliminating the docking interactions between PilA-N and PilA-C by expressing only the first 37 amino acids. The helical structure at the N terminus is not only important for the pilus assembly and prepilin translocation from the cytosol into the inner membrane[192], but also regulates the Two-Component System (TCS). This regulatory mechanism controls the synthesis of PilA subunits and other pili-related proteins and functions (Figure 4.2)[32-35].

ΔpilA-N cells expressing one of the three constructs were harvested to assess if nanowires could be secreted. Whole-cell lysates of induced cells were harvested at the late log phase and immunoblotted against PilY1-1 as loading control and against a his-tag for each of the

respective truncations. Filament preparations showed that neither of the constructs could rescue the secretion phenotype, but most importantly, truncated pilins were unstable and potentially degraded as seen in Figure 4.3. Whole-cell lysates show the presence of other pili-related proteins, but the truncated of PilA-N variants were not detected, suggesting that the truncation created an unstable product. These results suggest that the disruption of the interaction between PilA-N and PilA-C is critical for pilus assembly and statbilty

Although these results do not provide a clear and direct insight into the PilA-N and PilA-C interactions, we have experimentally demonstrated that PilA-N filaments are not structurally viable and most likely undergo a degradation process in the periplasm. Future studies will address the effect of point mutations disrupting the interaction between PilA-N and PilA-C and their effect on nanowire secretion.

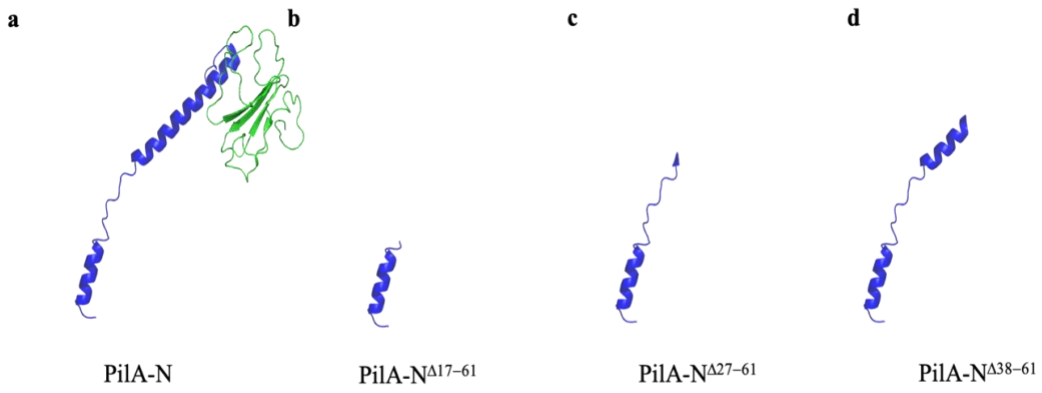

Figure 4.2: Truncated Pilins Diagram.

Geobacter sulfurreducens PilA-Nstructure showing the truncation site on PilA-N to prevent the interaction between PilA-N (blue) and PilA-C (Green). PilA-N strutures highliting the truncation site in PilA-N $^{\Delta 17\text{-}61}$ (**b),** PilA-N$^{\Delta 27\text{-}61}$ (**c**), and PilA-N$^{\Delta 38\text{-}61}$ (**d**). Figures made with Pymol using the PDB structure 6VK9 (PilA-N-C).

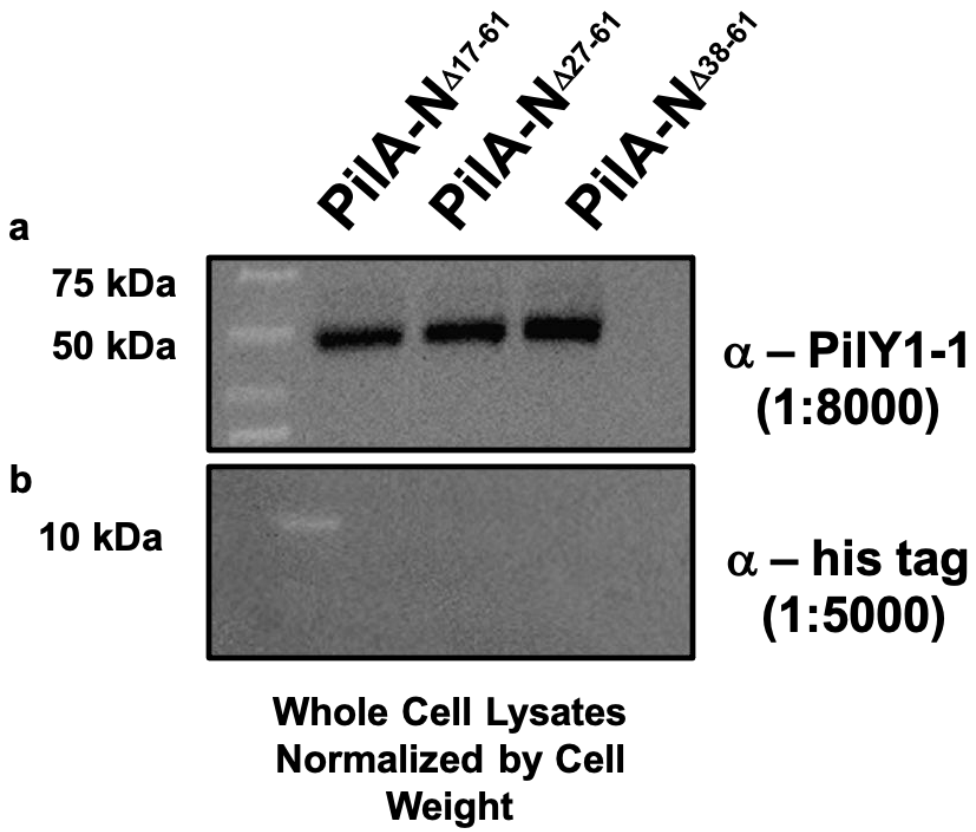

Figure 4.3: PilA-N truncations destabilize the protein.

Immunoblots of whole cell lysates of *ΔpilA-N* strains expressing the truncated pilin constructs shows expression of PilY1-1 (shown as a loading control) (**a**) but no PilA-N (**b**).

4.5.3. Role of glycines in pilus dynamics and stability

The recently resolved structure of PilA-N-C filaments provides insight into the interactions of PilA-N and PilA-C to assemble and stabilize filaments[59]. Once the relevance of PilA-C in the stabilization of PilA-N-C filaments was concluded, we decided to study the mechanism through which PilA-N and PilA-C interact. According to the presented structure, there are extensive contacts between PilA-C and the C-terminal helix of PilA-N. The C-terminal 5-residues of PilA-N protrude from the main helical core of the protein and serve as anchors for the "flaps" from PilA-C (Fig. 4.4A-B). Despite our current understanding regarding the interactions between PilA-N and PilA-C to assemble into filaments, little is known about the role of PilA-C in the structural stability of the pilus and the mechanism through which these two proteins interact with one another.

To determine the role of PilA-C residues in pilus dynamics, MD simulations were conducted on four Gly residues that are integral parts of two of the loops that form the protein's globular domain. Four Gly residues were mutated (G10, G11, G31, and G37) into Ala, and principle component analysis was performed to show independent trajectories and compare eigenmodes to determine the pilus dynamic *in silico*. Results show that approximately 46% of the pilus dynamics come from the hinges in the loops containing G31 and G37 relative to G10 and G11. Figure 4.4 C shows the summed principle component projections for the three lowest eigenmodes averaged over multiple independent MD trajectories relative to wild PilA-C. It can be observed that individual point mutations have a clear reduction in motion compared to PilA-C^{WT}. Similarly, a quadruple mutant (G10A, G11A, G31A, and G37A) also suffers a movement defect in a

range similar to the other 4 single-point mutants which suggest a role of these four residues in pilus dynamics. These computational results not only show that PilA-C plays a role in pilus stability (Figure 4.4D-F), but also that these four residues are key for the protein-protein interactions that give rise to the union of PilA-N and PilA-C.

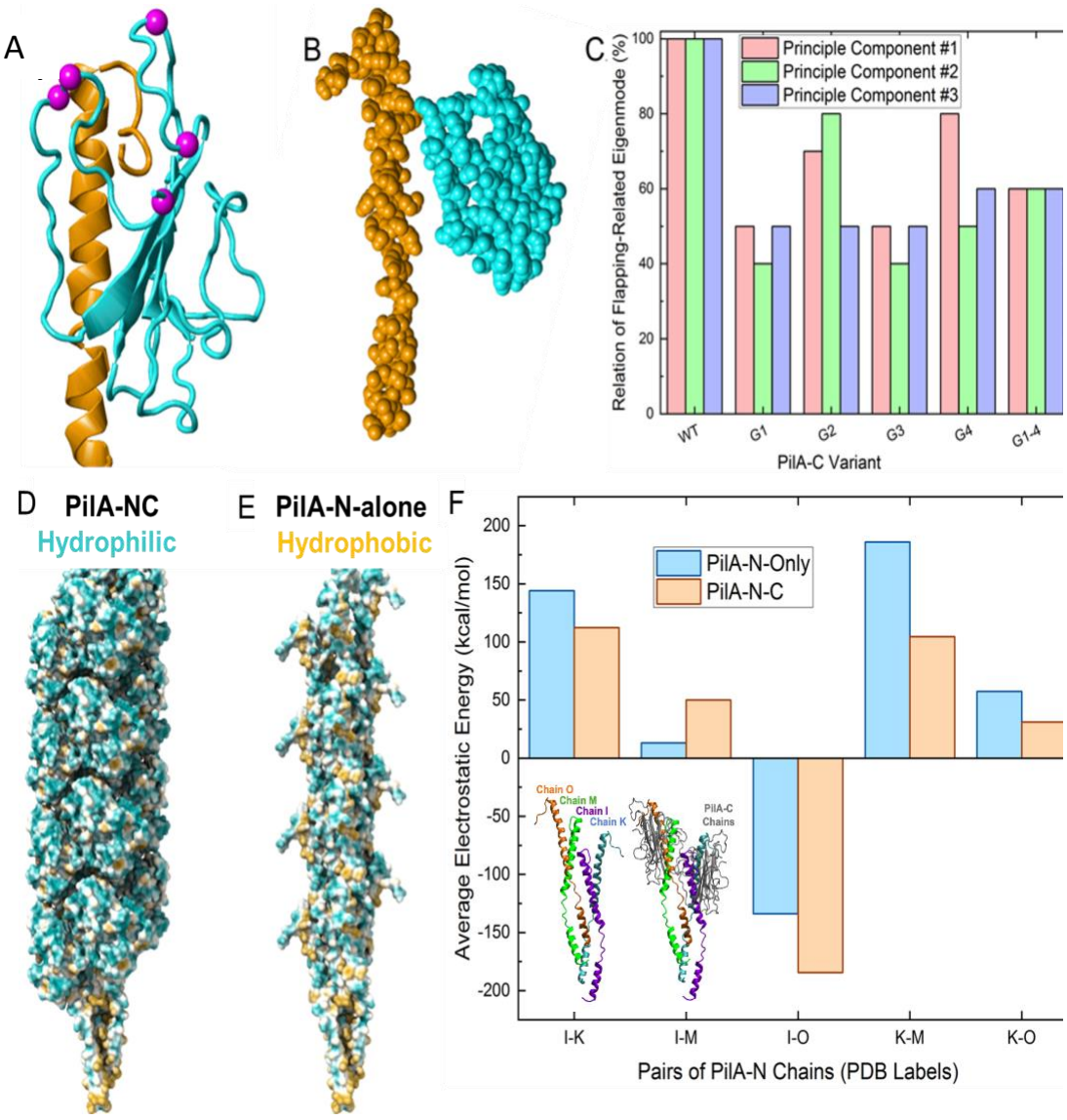

Figure 4.4: Co-assembly of PilA-C(cyan) and PilA-N (yellow).

A-B, Flaps of PilA-C could wrap around PilA-N. Glycines (pink) may function as hinges for flaps to open. **C,** Projections for eigenmodes resemble a flapping motion. **D-E,** PilA-C reduces the hydrophobicity of PilA-N filament. **F,** PilA-C stabilizes PilA-N. Inset shows chains I, K, M and O to make the pairing projections.

4.6 Discussion

As stated in this chapter, the structural integrity of the pilus filament is a consequence of the interactions between its two components: PilA-N and PilA-C. Although the role of this pilus has been discussed in length in previous chapters, little is known about the dynamics and protein-protein interactions that allow the filament to regulate or directly translocate the secretion of nanowire-forming cytochromes into the extracellular environment. To have a better insight into the pilus dynamic and stability of the filament, we approached the problem through *in vivo* and *in silico* analysis.

First, we decided to truncate the helical core responsible for the interaction between PilA-N and PilA-C at the C terminus of the protein through electrostatic interaction between S61 and A1, and hydrophobically between L47 and Y45 respectively[59]. The expression of the truncated PilA-N pilins at residues L16, A26, and S37 aimed to study the effect of Two-Component System in nanowire secretion in a *ΔpilA-N* background when the interaction between PilA-N and PilA-C is absent. PilA proteins are regulated through a negative feedback loop called the Two-Component System (TCS) composed of a histidine kinase (PilS) and a signal protein that serves as a transcriptional regulator of the *pilA* operon[33,35]. This mechanism allows the cell to use the sensory kinase embedded in the inner membrane to regulate the expression of pilins. As the concentration of pilins increases, PilS will dephosphorylate PilR to repress *pilA-N* transcription. This mechanism is thought to allow the cells to quickly adapt to extracellular stress and conditions[33,35]. Interestingly, *Gs* pilin is also regulated by this mechanism and its disruption has been shown to affect the expression of OmcS, OmcC, and OmcB[32,34].

Previous studies have shown that the most likely place of interaction occurs in the inner membrane where residues E5 and P22 from the pilin play a key role in PilS recognition[33,35]. Therefore, two of the truncated pilins (A26 and S37) provide a way to compare a) PilS/PilR regulation and b) protein stability. As mentioned earlier, no cytochromes were observed extracellularly in either construct, which suggests that PilA-N alone is not responsible for cytochrome secretion. To further test this hypothesis, qRT-PCR will be conducted in the future to compare WT, *ΔpilA-N*, and the three truncated pilins constructs to determine if there is any difference at the transcriptional level. Although some studies suggest that a truncation of the C termini of pilus affects native *pilA* transcription, we were not able to determine if this is the case in *Gs*. Even though we can assume that PilA-C is the structural equivalent to the C termini of other pili, as we are working with a *pilA-N* knockout we would need to introduce said constructs into a WT background to determine if there is also a transcriptional reduction. Once we established that no cytochromes were secreted using the N-terminus of PilA-N we investigated the stability of the monomer. Results shown in Figure 4.2 demonstrate that truncated pilins are not stable in the absence of PilA-C and that a hypothetical PilA-N filament would be highly unstable as shown in Fig 4.4. It is known that other T2SS endopilins are primed with a complex composed of minor endopilins that will allow the complex to export proteins, adhesins, toxins, and cytochromes[60,61]. It is possible that the interaction of PilA-N and PilA-C recruits PilY1 proteins that will then serve as direct contact between the filament and the cargo. Computationally, the results also support this hypothesis. MD simulations showed that PilA-N interactions are much more stable when PilA-C is present, as we can observe an increase in energy generated by the non-bonded interactions. The N-terminal of PilA-N

is primarily composed of hydrophobic residues, and binding to PilA-C prevents the exposure of the hydrophobic side chains to the aqueous environment. Thus, we can conclude that the interaction between PilA-N and PilA-C not only plays a role in nanowire translocation but also pilus stability.

Once the importance of this interaction was established, we further studied the plausible mechanism through which PilA-C interacts with PilA-N. From the structure, we can observe that the C terminus of PilA-N protrudes through PilA-C which wraps itself around the 5 terminal residues at the C terminus of PilA-N[59]. The globular protein PilA-C contains two flaps that contain Gly residues that were thought to act as hinges for movement (G10, G11, G31, and G37). Similarly, the HIV-1 protease in Human Immunodeficiency Virus (HIV) contains glycine-rich flaps or β-hairpins that allow the enzyme to bring the substrate closer to the catalytic site composed of Asp-25-Thr-26-Gly-27[193]. MD simulations of the enzyme showed a downward motion of the flap elbows, cantilever, and fulcrum that resulted in an upward motion to close and rotate the flaps into the catalytic domain of the protease[193]. Our computational work showed a similar case where Gly residues on both flaps serve as a hinge to allow the protein to wrap itself around PilA-N's C terminus domain. Our results show that the majority of the movement comes from the loops containing the G31 and G37 residues. Furthermore, the results of single-point mutants (G10A, G11A, G31A, and G37A) are comparatively similar to the simulated trajectories of a quadruple-point mutant (PilA-C$^{G10A,\ G11A,\ G31A,\ G37A}$). Although these results support the hypothesis that these residues play a key role in pilus dynamics and

stability, PilA-C mutants have been designed *in vivo* and will be expressed in a *ΔpilA-N* background.

Given our failed attempts to reconstitute *Gs* PilA filaments in *P. aeruginosa,* I am currently building on the work of Ueki *et al.* to use *E. coli* as a chassis[191]. Rather than just expressing *pilA-N* as previous works have done[191], I have incorporated both *pilA-N* and *pilA-C* to ensure proper assembly and stability of the filament. Preliminary experiments have been conducted to optimize the expression and purification of PilA-N-C filaments from *E. coli* in large quantities. Immunogold labeling will be performed in both filament preparations and whole cells to show the successful assembly of *Gs* PilA-N-C filaments. These tools will allow us to purify higher quantities of PilA-N-C filaments and perform various studies to corroborate what our *in silico* and *in vivo* results propose. We will test the role of PilA-C in the pilus stability using circular dichroism as a function of temperature by monitoring the melting of secondary structure features, denaturation, and disassembly. These results will allow us to further characterize the role of PilA-C in pilus dynamics and stability to end over two decades of controversy regarding the wrongfully called e-pili in EET.

4.7 Materials and Methods

4.7.1. Bacterial strains and growth conditions

The following strain used in this study weas obtained from our laboratory culture collection for further genetic manipulation: *pilA-N* knock-out mutant strain[162] (designated *ΔpilA-N*). The cultures were maintained at 30°C under strictly anaerobic conditions in growth medium supplemented with acetate (10 mM) as the electron donor and fumarate (40 mM) as the electron acceptor. As described previously[46], the *G. sulfurreducens* cells were grown in sterilized and deoxygenated NBAF medium[64], and 1L NBAF medium contained the following: 0.04 g/L calcium chloride dihydrate, 0.1 g /L, magnesium sulphate heptahydrate, 1.8 g/L sodium bicarbonate, 0.5 g/L sodium carbonate, 0.42 g/L potassium phosphate monobasic, 0.22 g/L potassium phosphate dibasic, 0.2 g/L ammonium chloride, 0.38 g/L potassium chloride, 0.36 g/L sodium chloride, vitamins and minerals[64]. 1 mM cysteine was added as an oxygen scavenger. NBAF agar plates were prepared as previously described [144] with the addition of 1.5% agar and 0.1% tryptone. The cells were grown under nanowire-producing conditions as previously described[21]. All bacterial strains were stored at -80°C as 15% DMSO stocks for *G. sulfurreducens*.

4.7.2. Truncated Pilin complementation

ΔpilA-N complementation was performed as previously described[144]. Truncated pilins were constructed by digesting the pRK2-Geo2i plasmid and truncated pilins amplicons (PilA-N$^{\Delta 17\text{-}61}$ (L16), PilA-N$^{\Delta 27\text{-}61}$ (A26), and PilA-N$^{\Delta 38\text{-}61}$ (S37) with EcoRI and NheI. Amplicons were generated using the following primers: PilA-N F as forward primer

with PilA-N L16, PilA-N A26, and PilA-N S37 respectively. Reverse primers include a 6x his-tag for western blot analysis. Phusion High-Fidelity DNA Polymerase (NEB M0530S) was used to generate the amplicons following the manufacturer's protocol.

Table 4.1: Primers to truncate *pilA-N*

Name	Sequence (5' – 3')
PilA-N F	cgcgaattcTTGGCCAATTACCCCCATACC
PilA-N L16	ctagctagcCTAGTGGTGATGGTGATGATGGAATCGCAATGCTTA GAGAATACCG
PilA-N A26	ctagctagcCTAGTGGTGATGGTGATGATGTTGACACGTTACGCC GAGAACT
PilA-N S37	ctagctagcCTAGTGGTGATGGTGATGATGTTTCTCAAGTCTTATG ACGCCGC

Digested products were gel extracted using NEB's Monarch DNA Extraction Kit (T1020L) and then ligated using T4 Ligase (NEB M0202S) following the manufacture's protocol. Ligated constructs were then transformed into DH5α (NEB C2987H) and sent for sequencing to confirm DNA sequences. Sequence confirmed plasmids were then transformed into S17.1 strains and then transformed into *ΔpilA-N* as previously described[59,144]. Cells were cultured as previously described with 200 μg/mL Kanamycin for selection and 50μg/mL for expression. Cells were induced with 50 μM vanillate for protein expression.

4.7.3. Cell and protein normalization for comparative expression studies

Whole cell lysates were normalized using a BCA Protein Assay Kit (Pierce #23225).

4.7.4. SDS-PAGE

For SDS-PAGE analysis, samples were boiled for 10 minutes in 2x SDS loading buffer with β-mercaptoethanol. Samples were run for 35 minutes at 190V in a 4-20% gradient Tricine protein gel (Thermo Fisher Scientific). Precision Plus Protein Prestained molecular weight standards (BioRad) were used to compare the molecular weight of the targeted proteins.

4.7.5. Western blot analysis

Polyclonal anti-PilY1-2(C-GEVVRPVFDVNLDGKVDYSDT) was raised as previously described by LifeTein[46]. Commercially available anti-his (Biorad #6200203) was used in this study. Antibodies were used to a 1:2000 dilution unless specified.

4.7.6. Computation of mechanical stability of pili.

Molecular Dynamics Simulation. System setup and parameterization*:* Starting from the wild-type *G. sulfurreducens* PilA-N/C filament recently reported from our lab (PDB 6NEF)[194], we constructed models of the experimentally designed mutants Aro5 (F24A, Y27A, Y32A, F51A, Y57A) and TRP (F51W, Y57W), which have been previously investigated[195,196]. We also constructed by homology the pilus filament of *G. metallireducens* (Metalli) by mutating 13 residues of the *G. sulfurreducens* PilA-N subunit

in situ within the filament context (S25A, V29Q, Y32F, S37E, L43T, A46N, A50Y, F51Y, A52S, D53E, D54H, T56F, P59N) and deleting the terminal 2 residues from each PilA-N subunit[197]. The *G. metallireducens* pilus was assumed to be heterodimeric, like the pilus of *G. sulfurreducens,* and because our interest was in the PilA-N – PilA-N interaction strength, we assumed that the PilA-C subunit for the two bacterial pili are identical. Each pili model was composed of 8 PilA-N and 8 PilA-C subunits.

Using tLEaP in the AmberTools20 package[198,199] hydrogen atoms were added to the pili models assuming standard protonation of titratable residues for circumneutral pH (e.g., deprotonated Asp and Glu; singly protonated His on N_ϵ; protonated Lys, Arg, Cys, and Tyr). Each structure was placed at the center of a box of explicit water with at least a 15 Å buffer region to the boundary of the box. A sufficient number of counterions were added to achieve charge neutrality. Standard proteinogenic residues were modelled with the AMBER FF14SB force field[175]. The TIP3P water model[176] and the monovalent ion parameters of Joung and Cheatham[177] were used to model the solution state.

Pre-production simulations. Each solvated pilus was subjected to 20000 steps of steepest descent, followed by 80000 steps of conjugate gradient minimization. A 10 kcal/(mol $Å^2$) restraint was applied to the heavy atoms of the protein backbone during the minimization. The system was subsequently heated from 0 to 300 K at a rate of 0.3 K/ps in the NVT ensemble and held at the final temperature for 1.0 ns. The restraints on the protein backbone were reduced to 1.0 kcal/(mol $Å^2$) for the heating stage, except for residues 6-14, 67-74, and 128-140. An additional 99 kcal/(mol $Å^2$) restraint force was applied to these residues to mimic the physical constraint that would be provided by their

burial in a bacterial cell membrane, as suggested from the *Orientations of Proteins in Membranes* webserver (https://opm.phar.umich.edu). All the restraints (except those mimicking membrane anchoring) were further reduced to 0.1 kcal/(mol Å^2) for a subsequent 2 ns simulation at 300 K in the NVT ensemble. The restraints mimicking membrane anchoring were increased by 0.9 kcal/(mol Å^2) so that the force applied to the selected residues was a constant 100 kcal/(mol Å^2)in all stages of the dynamical simulations. Finally, the density of the system was equilibrated over an 8 ns simulation in the NPT ensemble at 1.0 bar and 300 K. All NVT and NPT simulations (including the production-stage trajectories described below) employed periodic boundary conditions, the Particle Mesh Ewald[178] treatment of electrostatic interactions with a direct sum cut-off of 10.0 Å, the SHAKE algorithm[179,200] to rigidify bonds to hydrogen atoms, a Langevin thermostat with a collision frequency of 2 ps^{-1}, and an integration timestep for the Langevin equation of motion of 2.0 fs. Pressure in NPT simulations was regulated with a Monte Carlo barostat having a relaxation time of 1.0 ps. PMEMD in its CPU and GPU[201] implementations in the Amber20 package[199] was used to perform the minimization and dynamical simulations, respectively.

Production-stage simulations. The dynamics of the various pili were propagated with conventional (i.e., unbiased) MD in the NVT ensemble for 181 ns (Aro5 and WT), 155 ns (TRP), and 144 ns (*G. metallireducens*). A harmonic restraining force of 100 kcal/(mol Å^2) was applied to residues 6-14, 67-74, and 128-140 to mimic the physical constraint that would be provided by their burial in a lipid bilayer.

4.7.7. Relative Stability Analysis

The sum of van der Waals and Coulombic interactions among a bundle of four PilA-N subunits at the center of each filament was computed for all frames, sampled every 20 ps, over the last 30 ns of each production stage simulation. For this analysis, we used the pairwise keyword in CPPTRAJ[181], which computes the pairwise non-bonded interaction energies for the selected atoms. The total non-bonded interaction energy was taken as a relative measure of the PilA-N – PilA-N interaction strength. This quantity has been proposed to be a key factor in filament stability[202].

4.7.8. Cryo-EM reconstruction of OmcS filaments

The structure of OmcS filaments from Aro5 and Trp strains was solved as described previously[46]. Briefly, the OmcS filaments were first purified from the biofilm of strains Aro5 and Trp under the electricity-producing conditions similar to those used for WWT biofilms. The cryo-EM sample was prepared using the same blotting condition as previously described[203]. For each sample, approximately 4000 images of collected by Titan Krios microscope equipped with a K2 summit camera and energy filter from Yale West Campus Imaging Core. The raw movies were first motion corrected by MotionCor 2.1[204] and approximately 100,000 particles were picked manually. A round of 2D classification was applied to filter particles suitable for reconstructions. These particles were combined directly to generate the 3D volume using helical reconstruction implemented in RELION 2.1[205]. The reconstructed maps were at comparable resolution with the OmcS map from the wild-type with the map for OmcS nanowires of tryptophan-substituted and Aro5 strain

at 3.4 Å and 3.2 Å respectively. The OmcS structure (6EF8) can be readily docked into the density without any noticeable need for refinement or structural change. To generate the difference map, the maps were first manually aligned in Chimera 1.15 and then the vop subtract command was used to generate the difference map. All final figures were rendered in Chimera[185].

5. OmcS polymerization requires H16 axial coordination.

Controllable assembly of Geobacter cytochrome nanowires via tuning metal coordination is essential for extracellular electron transfer

Vishok Srikanth*, Sophia M. Yi*, **Aldo I. Salazar-Morales***, Matthew J. Guberman-Pfeffer, Ruchi Jain, J. Patrick O'Brien, Yangqi Gu, Peter J. Dahl, Sibel Ebru Yalcin, Anatoly I. Frenkel, Victor S. Batista, Gary W. Brudvig, & Nikhil S. Malvankar

* These authors contributed equally.

This chapter is a modified version of a submitted paper.

5.1 Author Contributions

V.S. established methods for nanowire depolymerization and self-assembly by carrying out gel filtration, UV-vis, CD and TEM characterization, and purified and characterized nanowires for these studies. S.M.Y. performed EPR and XAS data analysis. M. J.G-P performed molecular dynamics simulations to assess filament stability as a function of pH. **A.I.S.-M. and R.J. constructed the H16A mutant strain and A.I.S.-M. performed biochemical and functional characterization of the strain.** S.M.Y. purified OmcS nanowires for EPR and XAS. J.P.O. performed initial nanowire purification and UV-vis and CD spectroscopy. Y.G. assisted with CD and TEM characterization. P.J.D. performed

initial molecular dynamics simulations to compute dihedral angles under the guidance of V.S.B. S.E.Y. contributed to analysis and interpretation of UV-vis data. A.I.F. guided XAS measurements and data analysis, and G.W.B. guided EPR measurements. N.S.M. supervised the project. V.S., S.M.Y. and N.S.M. co-wrote the manuscript with input from all authors.

5.2 Summary

Microbial extracellular electron transfer (EET) is essential for a wide range of globally-important environmental processes and for applications in bioenergy, biofuels, bioelectronics, and bioremediation. Since 2005, type-IV pili have been thought to mediate long-range (>10 μm) EET in diverse species. However, recent studies revealed that during EET, conductive "nanowires" on the surface of *Geobacter sulfurreducens* are made up of cytochromes OmcS and OmcZ whereas pili remain intracellular, show low conductivity, and are required for secretion of cytochrome nanowires. Out of 111 cytochromes, only *omcS* and *omcZ* are essential for EET to minerals and electrodes, respectively. Nevertheless, the physiological relevance of OmcS and OmcZ filaments has been strongly questioned. Furthermore, the filaments' underlying polymerization mechanism is unknown. Here, we show that pH-tunable metal coordination across inter-protomer interfaces is essential for OmcS nanowire biogenesis *in vivo* and EET, and enables reversible nanowire assembly *in vitro*. Electron paramagnetic resonance and X-ray absorption spectroscopies reveal that hemes partially lose their axial histidine coordination at low pH, a finding supported by UV-visible and circular dichroism spectroscopies. Our studies suggest that inter-protomer metal coordination provides a latch to direct subunit

orientation to drive nanowire assembly. We thus show that chemically tuning metal-ligand coordination and protein-protein interfaces yields nanowires with controllable assembly. Our studies reveal a novel cytochrome polymerization mechanism distinct from previous examples of cytochrome assembly in engineered or disease conditions. Harnessing the bacterial ability to construct self-assembling and environment-sensing supramolecular structures that can withstand and function in acidic conditions and high-temperatures could yield stimuli-responsive bioelectronics.

5.3 Significance Statement

Until 2019, cytochromes were not believed to have the ability to polymerize into filaments as this feature was not believed to be necessary for cellular respiration. Our work characterizing OmcS filaments[44] showed that *Geobacter spp.* can polymerize cytochromes into filaments to facilitate EET. This work shed light on the axial heme-coordination of OmcS that allows for cytochrome assembly into filaments. In this work, I have developed a mutant ($OmcS^{H16A}$) that disrupts one axial coordination between the interface between heme 5 in each subunit and histidine 16 (His16) in the neighboring subunit to disrupt nanowire assembly. Here, we show for the first time that heme axial coordination is essential for cytochrome assembly and that the disruption of OmcS polymerization causes metabolic deficits in physiological growth conditions.

5.4 Introduction

In most cells, the biochemical chains of redox reactions that define the energy harvesting pathways of life[206] take place wholly within cellular compartments. The relevant

electron transport mechanisms are commensurate with the 1-2 nanometer length scales across which these reactions occur, relying on electron tunneling between molecules, and diffusion of small electron carriers[207,208]. However, many environmental microbes exhibit the remarkable capacity to expand their electron transport chain to span micrometers[21,37,209,210] or even centimeters[211-214], reaching electron acceptors and syntrophic partner cells over distances vastly exceeding the size of a single cell. Understanding the ability of diverse bacteria to perform extracellular electron transport (EET) to and from organisms and inorganic materials in their environment is critical for both understanding environmentally important biogeochemical processes and for unlocking the potential of these biophysical mechanisms for applications in engineering renewable energy devices and mixed biotic-abiotic systems[215-219].

Several longer-range EET processes are mediated by extracellular appendages referred to as microbial nanowires[21,209,212]. Studies of the nanowires used by *Geobacter sulfurreducens* (Fig. 1A) to transfer electrons over micrometers to extracellular minerals[30], syntrophic partner cells[109], or electrodes in bioelectrochemical systems[155] identified that PilA, the hypothesized protein building block of these filaments, was critical for certain EET processes involving microbial nanowires[21,38]. These claims inspired debate over whether aromatic amino acids in PilA could give rise to electron transport along such putative filaments[220,221], or whether instead EET in *Geobacter* was likely to be mediated by the abundant cytochromes produced in the biofilms performing EET[222,223]. Direct structural and biochemical studies of the nanowires obtained from cells under conditions requiring EET demonstrated the existence of protein polymers consisting of multiheme

outer membrane cytochromes OmcS[44,224] and OmcZ[40]. To date, the only experimentally determined high-resolution structures available for microbial nanowires from *G. sulfurreducens* are those of OmcS filaments. However, the physiological role and natural assembly of cytochrome nanowires has been questioned[225,226].

Further driving interest in OmcS filaments[227,228] is the fact that protein-based electronic nanomaterials have the potential to offer features critically needed for the next-generation of bioelectronics, including mechanical flexibility, controlled biological properties, and mixed electronic and ionic conductivity[229]. Aside from protein-based microbial nanowires, proteins are widely considered to be electronic insulators, transferring electrons over only 1-2 nanometers and losing functionality under non-physiological conditions[230-232]. OmcS nanowires can transport electrons efficiently over micrometers due to their uniquely long-range seamless arrangement of hemes stacked within edge-to-edge distances of approximately 3.5-6 Å (Fig. 5.1B)[44,224]. Cryogenic electron microscopy (cryo-EM) showed that the six bis-histidine ligated hemes in each OmcS protomer are arranged in three parallel-stacked pairs, with each heme pair perpendicular to the other pairs in a T-shaped geometry. The interface between subunits shows axial coordination of heme 5 in each subunit by histidine 16 (His16) in the neighboring subunit (Fig. 5.1C). This long-range polymerization of OmcS was itself surprising, given that supramolecular assemblies of heme proteins had been studied for over fifty years prior[233], without any indication that such an assembly could be physiologically required for cell respiration. Prior studies have examined the engineering potential of cytochrome *c* oligomerization that relies on a protein domain-exchange

mechanism[234-236]. However, this mechanism does not appear compatible with the OmcS cryo-EM structures, as the OmcS protomers within the filament do not appear to have multiple domains that could be exchanged during the polymerization process. Therefore, a novel mechanism must be invoked to explain the formation of OmcS nanowires. The inter-subunit metal coordination observed in OmcS had previously been observed in other cytochrome dimers[237,238], but no prior work had suggested that such an interaction could support the incorporation of thousands of monomers into a stable micrometer-scale assembly.

In this work, we address fundamental questions about the physiological role of OmcS filaments in *G. sulfurreducens* EET, and advance our understanding of the biophysical mechanism by which OmcS filaments are assembled. To directly understand the biological function of OmcS nanowires, we made a targeted mutation to the His16 residue responsible for inter-protomer metal coordination in the cryo-EM structures. Under the model that OmcS polymers are biologically irrelevant[225], which suggests that the known roles of OmcS in EET to insoluble iron oxides[30,36,239] are explained by redox activity of OmcS monomers, this mutation that disrupts OmcS polymerization should have no effect on EET. Instead, we find that disruption of inter-protomer metal coordination affects OmcS nanowire biogenesis and that the resultant lack of cell-attached OmcS filaments results in a defect in extracellular reduction of insoluble Fe(III) oxide. Furthermore, we find that His16 is required for localization of OmcS to the outer membrane and that wild-type OmcS expressed in cells is not monomeric when localized to the outer membrane. This finding is incompatible with previous models which proposed that OmcS mediates

EET via monomers localized extracellularly along non-cytochrome filaments. Our experiments thus provide direct evidence that polymerization of cytochromes into nanowires is essential for EET.

To determine the mechanism of OmcS polymerization, we directly probe the role of metal coordination in the oligomerization of OmcS. Iron-coordinating histidine residues become deprotonated to form imidazolate at high pH; at low pH they form imidazolium, potentially disrupting histidine-metal coordination interactions[240,241]. We find that, due to the flexible nature of ligation[242], controlling the protonation of these residues via pH manipulation drives reversible disassembly and self-assembly of OmcS nanowires, and we confirm via a suite of complementary spectroscopic methods that these transitions between monomers and polymers are accompanied by the expected changes in metal coordination without denaturation of the OmcS protein. We further utilize computational modelling to compare the strength of the inter-subunit metal coordination interactions to the strength of protein-protein interactions at the subunit interfaces and find that the strength of these interactions is comparable. Our findings suggest a model wherein inter-protomer metal

coordination serves as a latch to stabilize the relative orientation of subunits during nanowire assembly.

5.5 Results

5.5.1. His16 is necessary for *in vivo* OmcS polymerization and EET to Fe(III)

To study the role of heme axial coordination in cytochrome-forming nanowires we substituted His16 for Ala in the *omcS* gene of the OmcS-overexpressing CL-1 strain[156] *G. sulfurreducens*, creating the H16A strain. This point mutation in the 5th heme in the OmcS monomer disrupted the heme axial coordination between adjacent OmcS subunits in the H16A strain. Unlike wild-type CL-1 cells (Fig. 5.1A), strain H16A cells do not display any OmcS-like filaments (Fig. 5.1D). The *omcS* gene is essential for the reduction of insoluble Fe(III) oxide[30,36,239], we further examined whether the absence of OmcS filaments would affect this EET process. We found that strain H16A cells have a reduced ability to transfer electrons extracellularly to Fe(III) oxide (Fig. 5.1E) compared with the parent CL-1 strain. On the other hand, when we used soluble electron acceptors, H16A did not show any growth deficiencies (Fig. 5.3I) which further proves that proper assembly and secretion of OmcS nanowires is essential for reduction of Fe(III) as discussed in Chapter 2 and 3.

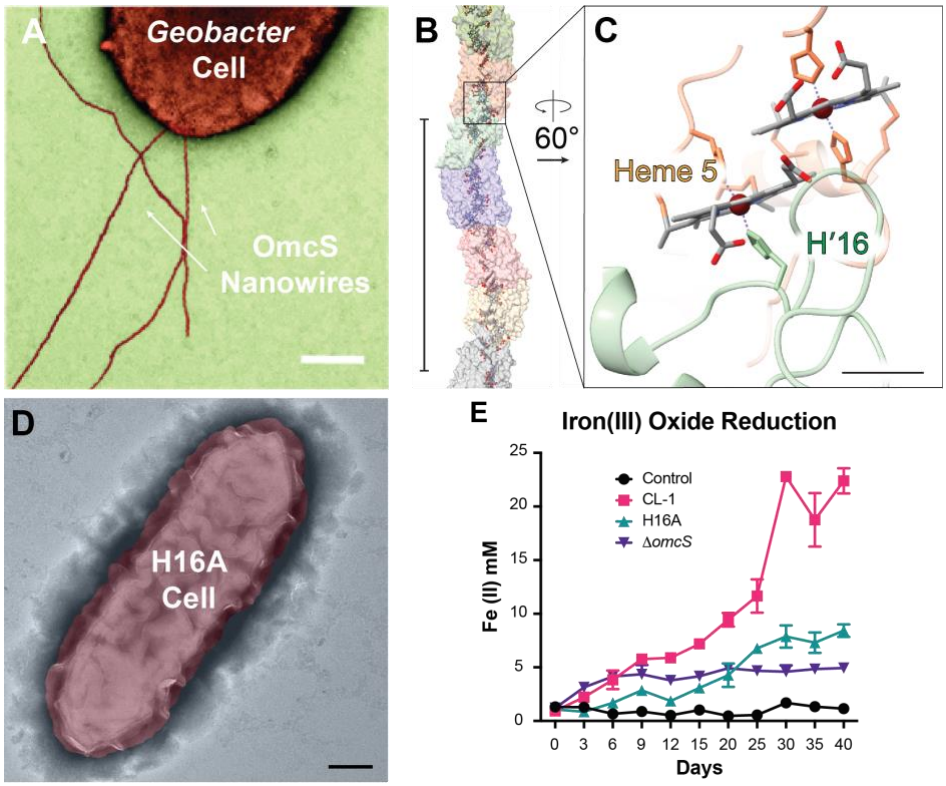

Figure 5.1: Histidine 16 is required for OmcS filament assembly and EET.

A, TEM image of intact OmcS nanowires emanating from a *Geobacter sulfurreducens* CL-1 cell (scale bar, 200 nm). **B**, Cryo-EM structure of OmcS nanowires (PDB ID: 6EF8) showing the stacked hemes (grey) along the filament core (scale bar, 20 nm), and **C** the inter-subunit site of heme iron coordination associated with residue His16 (scale bar, 5 Å). **D**, H16A mutation in *omcS* abolishes OmcS filament production in strain CL-1 (scale bar, 200 nm). **E**, Growth on insoluble Fe(III) oxide shows reduced ability of strain H16A (teal) to transfer electrons extracellularly compared with the parent CL-1 strain (pink), similar to cells in which the *omcS* gene was deleted (purple). Error bars show standard deviation, n = 3 biological replicates.

5.5.2. H16A does not cause transcriptional defects, but affects OmcS abundance and translocation.

As we described earlier, H16A cannot assemble OmcS nanowires, but can still grow using soluble electron acceptors which shows that this mutation is not lethal. To study the effect of H16A in OmcS monomers, we devised a series of biochemical assays to determine the influence of said mutation in the assembly and translocation of the protein into the extracellular environment. First, we performed a qRT-PCR analysis in CL1 and the H16A strain. This experiment showed that the transcription of OmcS, normalized to GroEL an intracellular chaperone, has a higher transcription in H16A than CL1 (Fig. 5.2A and 5.3A, B). Contrary to this, OmcS monomers were ~4.0 fold more abundant in CL1 compared to H16A (Fig5.3C-F). This difference observed in protein abundance and the transcription level of *omcS* in the mutant strain indicates the inability of OmcS to polymerize impacts the stability of OmcS protein *in vivo*.

To further understand how the H16A mutation impacted the potential assembly of OmcS filaments, we assayed subcellular fractions of the H16A and CL-1 strains for the presence of OmcS protein. We detected OmcS protein in the cytoplasmic, periplasmic, and outer-membrane-associated fractions of strain CL-1, but found no OmcS associated with the outer membrane in strain H16A (Figure 5.2C). This suggested that OmcS may be required to polymerize to be properly localized to the outer membrane.

Since OmcS filaments are stable in the presence of SDS if they are not heated, we devised a simple assay to check whether the OmcS we observed in the subcellular fractions

was in a monomeric form. We evaluated the subcellular fractions on SDS-PAGE with and without the heat treatment that is usually applied when preparing SDS-PAGE samples, creating quasi- "native" and "denatured" versions of each fraction. By including purified filamentous and monomeric samples of OmcS (see subsequent results sections), we could correlate the appearance of OmcS at the expected molecular weight to a high abundance of either polymeric or monomeric OmcS in a sample; samples that showed approximately 50 kDa OmcS only in the denatured version of a sample indicated that OmcS was present in a polymerized form (Figure 5.4C).

The amount of OmcS protein in the subcellular fractions is greatly reduced compared to our control for monomeric OmcS, making it difficult to detect OmcS in any of the "native" subcellular fractions even from compartments (e.g., cytoplasm) where the protein would be very likely to be present in a monomeric form. However, fractions that contained polymeric OmcS showed a clear difference between the "native" and "denatured" conditions with approximately 50 kDa OmcS being absent in the "native" condition and present in the "denatured" condition. This differentiation indicated that in the CL-1 strain, OmcS appears to already be in a polymeric state in the periplasmic and outer membrane associated-fractions. Together, our results indicate that the ability to polymerize is necessary for the proper localization of OmcS, and that monomeric OmcS is not present at or beyond the outer membrane, where OmcS is known to be involved in EET.

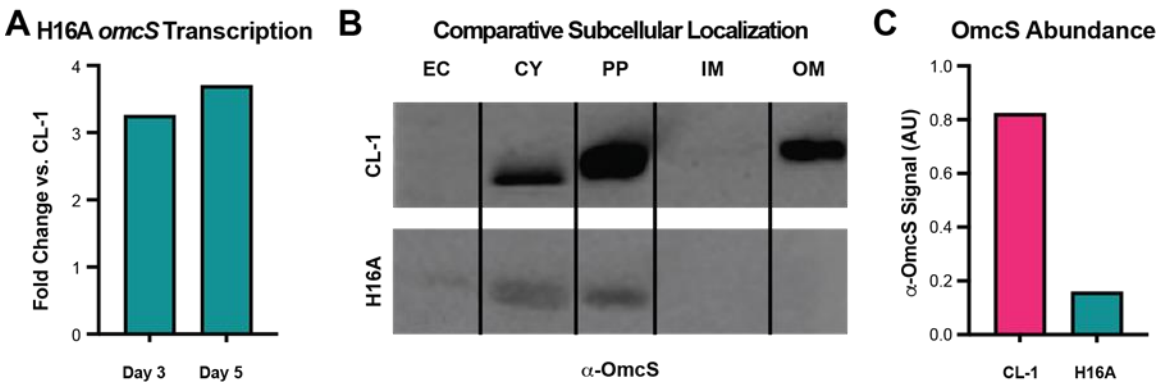

Figure 5.2: Comparative localization of wild type and H16A OmcS suggests no role for OmcS monomers in EET.

A, Quantitative Reverse Transcriptase – Polymerase Chain Reaction (qRT-PCR) analysis of RNA extracted from strains CL-1 and H16A indicates that OmcS transcripts are more abundant in the mutant. **B**, immunoblotting of subcellular fractions of strains CL-1 and H16A indicates that the H16A mutation prevents localization of OmcS to the outer membrane. **C**, immunoblotting of whole cell lysates (20 µg protein each lane) after five days of growth in fumarate media indicated that strain H16A produces a lesser abundance of OmcS protein than strain CL-1 (quantified immunoblot signal visualized, see Fig. 5.3).

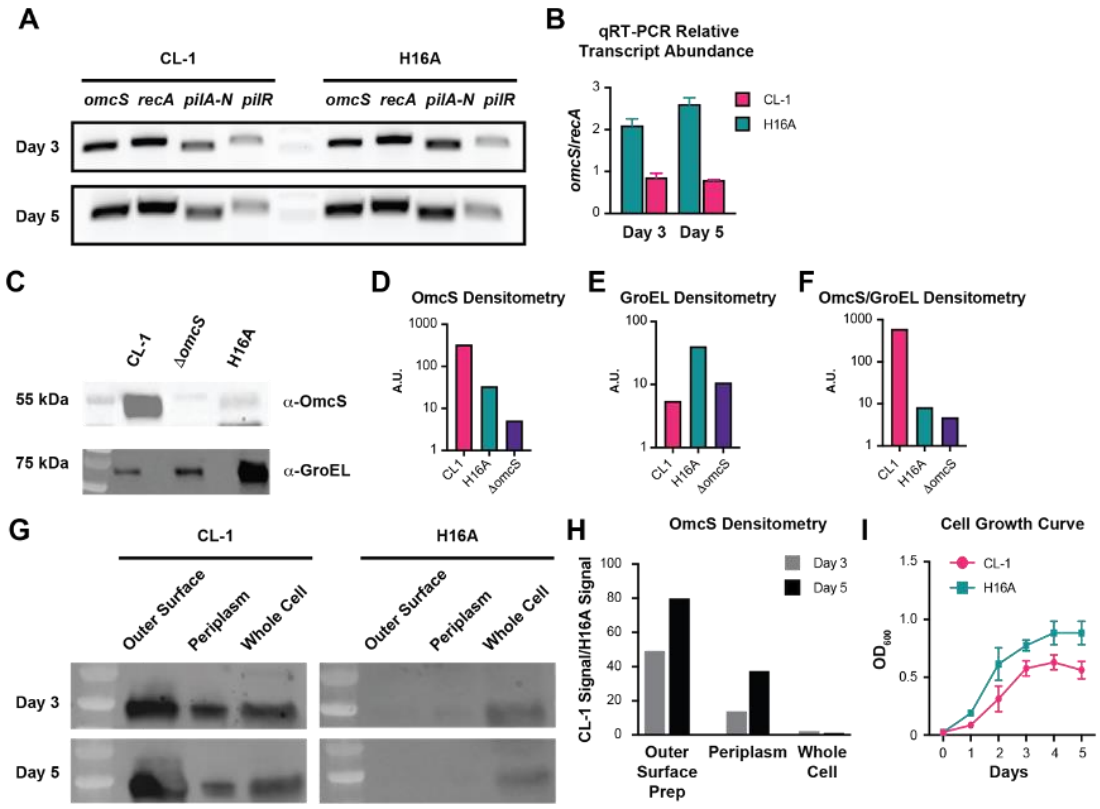

Figure 5.3: OmcS is degraded in H16A although transcription is not affected.

A, Agarose gel visualization of RT-PCR products produced from *omcS*, *recA*, *pilA-N*, and *pilR* transcripts present in total RNA extracted from strain CL-1 or H16A cells after either 3 or 5 days of growth. **B**, Relative abundance of *omcS* transcripts normalized to *recA* transcript, as assayed by qRT-PCR. **C-F**, Immunoblots and subsequent densitometry analysis illustrating the abundance of OmcS and GroEL proteins in whole cell lysates of strain CL-1, D*omcS*, and H16A; lanes from each strain correspond to comparable culture volumes. **G-H**, Immunoblot and subsequent densitometry analysis visualizing OmcS abundance in outer surface preparations, periplasmic fractions, or whole cell lysates of strains CL-1 and H16A. **I**, Typical growth curve illustrating cell density observed when growing strains CL-1 and H16A in liquid media.

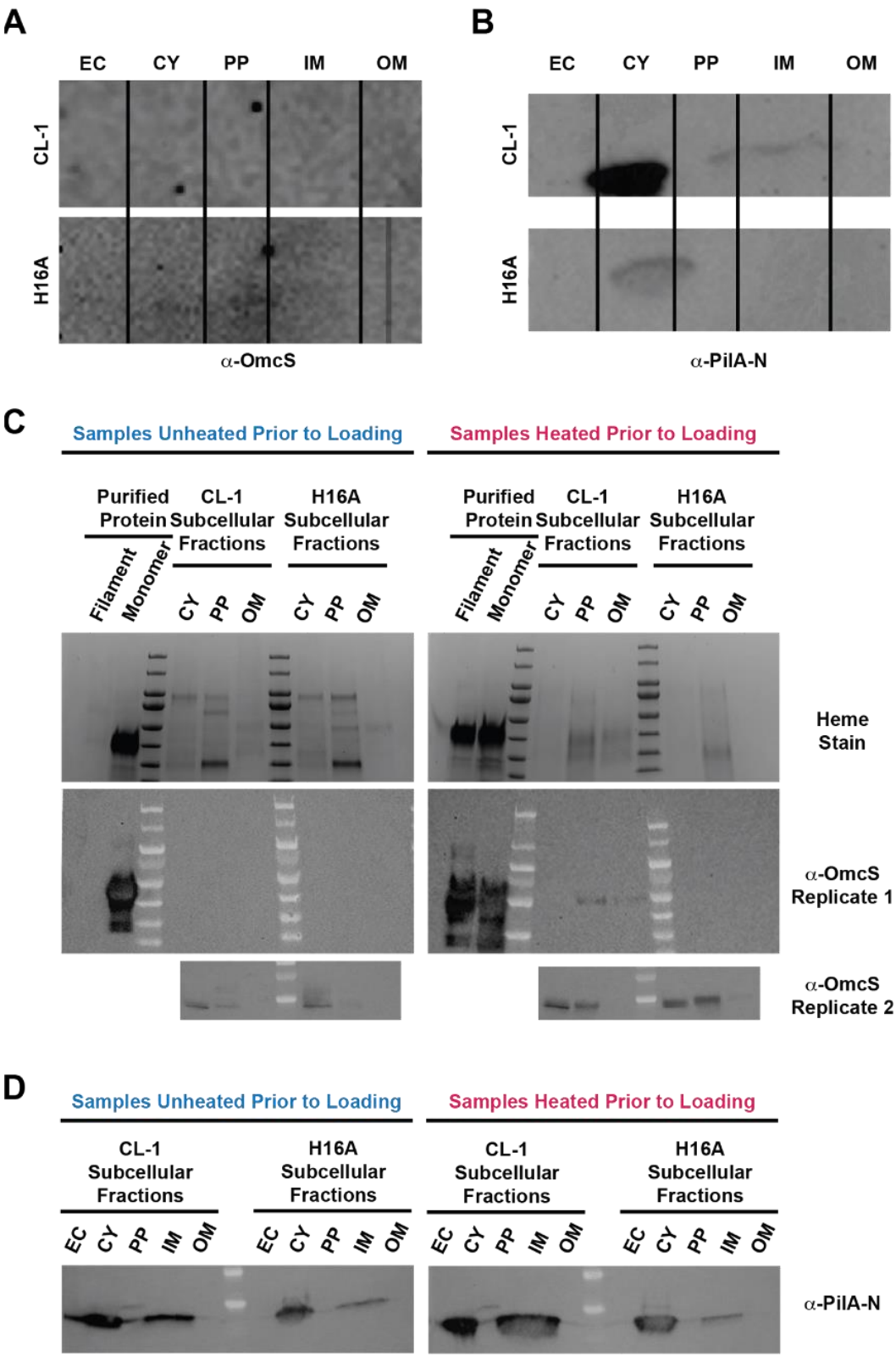
A
EC
CY
PP
IM
OM
CL-1
H16A
α-OmcS
B
EC
CY
PP
IM
OM
CL-1
H16A
α-PilA-N
C
Samples Unheated Prior to Loading
Samples Heated Prior to Loading
Purified Protein
Filament
Monomer
CL-1 Subcellular Fractions
H16A Subcellular Fractions
CY
PP
OM
Heme Stain
α-OmcS Replicate 1
α-OmcS Replicate 2
D
Samples Unheated Prior to Loading
Samples Heated Prior to Loading
CL-1 Subcellular Fractions
H16A Subcellular Fractions
EC
CY
PP
IM
OM
α-PilA-N

Figure 5.4: OmcS likely polymerizes in the periplasm and lack of OmcS filaments in H16A is not due to lack of pili.

A, Anti-OmcS immunoblot of soluble component of the subcellular fractions presented in **Error! Reference source not found.**B; lack of meaningful signal in any lanes indicates that OmcS present in these fractions is not well solubilized in these samples. **B**, Anti-PilA-N immunoblot of the same, soluble component of the subcellular fractions, indicated that soluble PilA-N was present in these samples, though notably not in outer membrane-associated or extracellular fractions. **C**, Heme staining visualization of c-type cytochromes and anti-OmcS immunoblot of the insoluble component of subcellular fractions from strains CL-1 and H16A, here compared when samples were or were not boiled prior to resolution in SDS-PAGE. Purified OmcS filament and monomer samples are provided for comparison and to illustrate the differential effect of heating or not heating the sample on monomeric and polymeric OmcS. **D**, Anti-PilA-N immunoblot of the same, insoluble component of the subcellular fractions.

5.6 Discussion

Since 2005, many studies of *G. sulfurreducens* microbial nanowire samples have asserted that the protein filaments being studied were exclusively type IV pili (T4P). The discoveries of OmcS and OmcZ nanowires[40,44,224] in filament preparations suggest an alternate interpretation of this prior work. Recent studies have suggested that previous studies measured cytochrome nanowires[40,44,226], that the role of T4P in *G. sulfurreducens* extracellular electron transfer is T4P involvement in the proper assembly and localization of cytochrome filaments, and that T4P filaments do not exist outside wild-type cells under nanowire-producing conditions that require EET[243]. It has been argued instead that *Geobacter* nanowire samples used in previous studies[224,225,244-247] do not contain cytochrome nanowires in any significant quantity[128]. However, in that study, cells were grown with soluble electron acceptors and not under conditions that require EET[128]. Our studies show that cytochrome nanowires are utilized by living cells during EET.

Related to the assertion that *G. sulfurreducens* uses T4P rather than cytochrome filaments for EET, the physiological role of OmcS filaments in *G. sulfurreducens* electron transfer has been questioned due to previous studies which proposed a model where monomeric OmcS 'decorated' extracellular T4P filaments[36,220]. The primary evidence for this model was immunogold detection of OmcS, which was performed via TEM of whole cell samples, where gold particles were observed to be localized to extracellular protein filaments[36]. The authors of this work asserted that the spacing of gold particles observed in their micrographs directly established the spacing of OmcS monomers 'aligned' on T4P filaments, though no direct evidence was provided that the visualized filaments are T4P.

Fundamental to these analyses was an underlying assumption that the labeling efficiency of OmcS in their immunogold experiment was 100%, which to our knowledge is not supported by any evidence either in this literature or elsewhere, and represents a fundamental misunderstanding of this technique. A far simpler, alternate explanation is that these authors observed gold nanoparticles localized to extracellular protein filaments in their immunogold experiment designed to detect OmcS because the extracellular protein filaments visualized in their experiment were OmcS filaments. However, the model of OmcS monomers involved in EET that arose from this literature has persisted.

My OmcS^{H16A} (H16A) strain reinforces our model where *Gs* polymerizes OmcS filaments in nature to reach a wider surface area and gain access to various electron acceptors. As shown in Figure 5.1E, our H16A strain behaves like a *ΔomcS* strain where we see a clear deficit compared to its parent strain CL1 as it is unable to assemble filaments (Fig. 5.1A, D). This iron reduction phenotype is similar to that observed in PilA and outer membrane cytochrome mutants where iron reduction phenotypes were deficient[21,41,42,248]. Although filaments are not assembled, it could be argued that monomers could still play a role in EET. Thus, our direct characterization of subcellular fractions suggests that OmcS monomers are not present at or beyond the outer membrane, and therefore cannot play a role in EET (Fig. 5.3G and Fig. 5.4). The finding that the H16A mutant cannot localize OmcS to the outer membrane further supports the notion that only the filament form of OmcS is directly relevant to the function of this outer membrane cytochrome. It could be argued that the lack of assembly is due to the lower concentration of OmcS in H16A compared to CL1, although our RT-qPCR data (Fig. 5.1A) shows that H16A is transcribing

approximately 3-fold more *omcS* than CL1. This discrepancy could be the result of the degradation of OmcS monomers due to the point mutation or accumulation due to their lack of axial heme coordination. Further experiments need to be conducted to assess the degradation of OmcS monomers in the interpretation of these results.

In conclusion, our present studies advance our understanding of the diversity of cytochrome nanowires and their biological role in microbial EET. These developments could also help to create next-generation electronics technology using synthetic biology for broad applications, ranging from programmable living cells to implantable electronic devices, and enable the harnessing of latent metabolic diversity in microbial communities toward uses in bioremediation and renewable energy applications.

5.7 Materials and Methods

5.7.1. Bacterial strains and growth conditions

Geobacter sulfurreducens strain CL-1, obtained from our laboratory culture collection, produces an elevated abundance of OmcS protein[156] and was used to obtain the OmcS nanowires for this study. *G. sulfurreducens* cultures were maintained at 25 or 30° C under strictly anaerobic conditions in sterilized and degassed NBAF growth medium[27], supplemented with 1 mm cysteine and with resazurin occasionally omitted as described previously[44]. NBAF media is composed of 0.38 g/liter KCl, 0.2 g/liter NH4Cl, 0.42 g/liter KH2PO4, 0.22 g/liter K2HPO4, 0.36 g/liter NaCl, 0.04 g/liter CaCl2·2H2O, 0.1 g/liter

MgSO4·7H2O, 1.8 g/liter NaHCO3, 0.5 g/liter Na2CO3·H2O, and 1.0mL/liter Na2SeO4. Media was supplemented with a) 10 ml/liter of a chelated mineral mix composed of 1.5 g of nitrilotriacetic acid (NTA), 0.1 g/liter MnCl2·4H2O, 0.5 g/liter FeSO4·7H2O, 0.17 g/liter CoCl2·6H2O, 0.1 g/liter ZnCl2, 0.03 g/liter CuSO4·5H2O, 0.005 g/liter AlK(SO4)2·12H2O, 0.005 g/liter H3BO3, 0.09 g/liter Na2MoO4, 0.05 g/liter NiCl2, 0.02 g/liter NaWO4·2H2O, and 0.10 g/liter Na2SeO4; and b) 15ml/liter DL vitamin mix composed of 0.002 g/liter biotin, 0.005 g/liter pantothenic acid, 0.0001 g/liter cyanocobalamin, 0.005 g/liter p-aminobenzoic acid, 0.005 g/liter nicotinic acid, 0.005 g/liter thiamine, 0.005 g/liter riboflavin 0.01 g/liter pyridoxine HCl, and 0.002 g/liter folic acid. Acetate was added as electron donor to a final concentration of 10mM and fumaric acid (40mM). For media containing Fe(III) (10 mM) as electron acceptor, a non-chelated mineral mix was prepared instead.

5.7.2. Filament Preparation

OmcS nanowires were separated from stationary-phase *G. sulfurreducens* cells. Cells recovered via centrifugation were resuspended in 150 mM ethanolamine (ETA), pH 10.5 solution and then blended for two minutes on the low setting using a commercial blender (Waring). Cells and cell debris were removed via centrifugation and 12.5% saturated ammonium sulphate (SAS) was added the remaining solution. The solution was centrifuged overnight and the precipitated nanowires were resuspended in 500 μL of ETA buffer pH 10.5.

Samples for immunoblotting were whole cell lysates prepared from cultures of strain CL-1 and H16A grown in NBAF media and sampled at the indicated time points, with each gel lane loaded with 20 µg of total protein. These samples were resolved on a 4-20% TGX (Tris-Glycine) gel and transferred using an iBlot2 Western Blot Transfer system (Thermo Fisher Scientific) utilized in accordance with the manufacturer's instructions. The polyclonal anti-OmcS primary antibody (LifeTein) was synthesized by immunizing two rabbits with synthetic peptide sequence containing residues 323 -339 of the mature OmcS protein (EGTADYTVLKGHAKIDD) and then affinity-purifying the serum against that peptide sequence. The primary antibody was used at a dilution of 1:2000 for immunoblotting. Visualization was achieved using an Immun-Star Goat Anti-Rabbit (GAR)-AP Detection Kit (BioRad) and a ChemiDoc imaging system (BioRad), following the manufacturer's instructions. Quantification was performed using ImageJ software.

5.7.3. Transmission electron microscopy (TEM) imaging

Carbon film-coated copper grids, mesh size 400 (Electron Microscopy Sciences), were cleaned by treatment in a PDC-001-HP plasma cleaner (Harrick Plasma) on the medium setting for 30 seconds. 5 µL of OmcS samples were deposited onto the carbon film face of the grid and incubated for 10 minutes to allow proteins in the sample to adhere to the surface, then the remaining solution was removed with blotting paper. Samples were subsequently negatively stained using a 1% phosphotungstic acid (PTA), pH 6 solution by two rounds of floating the grid face-down on a 50 µL drop of the staining solution for 30 seconds and then blotting the remaining liquid away. Grids were air-dried and then stored covered prior to imaging using a JEM-1400Plus microscope operating at 80 kV (JEOL).

Power spectra analysis of OmcS filaments imaged by negative-stain TEM was performed using SPRING software[94]. Raw images of OmcS filaments with a pixel size of either 1.9 or 3.1 Å were processed into 384 Å-long segments used to generate the power spectra based on an estimated helical rise of 47 Å per subunit [44] and a conservative estimate of the helix width as 100 Å, either with or without prior alignment and classification of the segments as implemented in SPRING.

5.7.4. mRNA extraction

For mRNA extraction, *G. sulfurreducens* strains were grown to mid- and late-log phase as previously described[249]. Cells were treated with RNAprotect Bacteria Reagent (Qiagen) and then harvested at 4 °C with centrifugation at 5,000 x *g* for 10 minutes. Cells were resuspended in TE buffer containing lysozyme and proteinase K to obtain the genomic material. An on-column DNAse digestion was performed according to the manufacturers protocol (Qiagen, RNeasy Plus Mini Kit) to eliminate DNA traces, and then mRNA was eluted. Triplicates were made from this mRNA extraction for downstream analysis via reverse transcription-quantitative polymerase chain reaction (RT-qPCR).

5.7.5. RT-qPCR

To verify any expression defect in H16A, we compared gene expression of *omcS, recA, pilA-N, and pilR* using previously published primer sets[249]. A total of 1 µg of mRNA was used as template to synthesize cDNA following SuperScript First-Strand's (Invitrogen) protocol, using random hexamer as primers, and then treating with an RNAse to remove traces of mRNA. A 1:5 dilution from the mRNA product was made to be used

as template to amplify *omcS, recA, pilA-N, and pilR amplicons using* GoTaq G2 Master Mix (Promega) for RT-PCR analysis; KAPA SYBR Fast qPCR Master Mix Kit (KAPA Biosystems) was used for RT-qPCR analysis. A 53° C annealing temperature was used for RT-PCR and 60° C for RT-qPCR. RT-qPCR analysis was performed in a CFX Opus 384 Real-Time PCR System (Bio-Rad) with the following settings: Enzyme Activation 95° C for 30 seconds; Denaturing 95° C for 3 seconds; Annealing 60° C for 30 seconds for 40 cycles. Melt curve analysis was performed from 65-95° C.

Table 5.1: Primer pairs for RT-qPCR analysis[249]:

Name	Sequence (5' – 3')
pilA-F	ATCGGTATTCTCGCTGCAAT
pilA-R	AATGCGGACTCAAGAGCAGT
pilR-F	TTTCCGGGAGGATCTCTTTT
pilR-R	TTATGATGCGGTCGCTGTAG
omcS-F	TGGTTGGCGAAGGCATAGG
omcs-R	CCATCAAGAACAGCGGTTCC
recA-F	CACCGGCATAATCTCCAAGT
recA-R	ATCTTGCGGATATCGAGACG

5.7.6. H16A Mutant Construction.

omcS was cloned into pk18mobsacB using *omcS* F and *omcS* R to amplify *omcS* and 500 bp up- and downstream of the gene using BamHI and XbaI to digest. Ligation was performed with T4 DNA Ligase following NEB protocol. Sequence verified plasmid was used as a template to introduce a point mutation using NEB Q5 Site-Directed Mutagenesis Kit following manufacturer's protocol and H16A F and H16A R primers. Sequence verified plasmid was transformed into the donor strain S17-1 for subsequent transformation into *G. sulfurreducens* strain CL1. Conjugation was performed as described by Chan *et*

al.[84] on NBAF agar plates supplemented with 200 μg/ml Kanamycin for selection. Single colonies were isolated on kanamycin plates and flanking primers (*omcS* Flanking F and R) were used to confirm the plasmid integration. Colonies with a successful plasmid integration were then plated in NBAF plates with 10% sucrose to identify second recombinant cells. Resistant colonies were then plated on kanamycin plates to test sensitivity. Kanamycin-sensitive cells were sent for sequencing to confirm the point mutation.

Table 5.2: *omcS*^{H16A} Construction

Name	Sequence (5' – 3')
omcS F (-500bp)	Acggttggatccttcggcaagcggggcagc
omcS R (+500bp)	Gatgttctagcgcccttgcgctcgccgtgg
H16A F	Ccacacgatggcaaactcgctgggcggc
H16A R	Caccttcgcactcggca
omcS flanking F (+50bp)	Ggagcgggatccggccgggttgccggagaa
omcS flanking R (-50bp)	Cctttctagcgcggaccccggcggaatcac

5.7.7. Iron Oxide Measurements

Soluble iron was measured using a ferrozine assay as previously described[250]. 100μL of culture were taken at different time points and solubilized in 0.5N HCl in the dark. This sample was used for the Ferrozine Assay ((1 g/liter) in 50 mM HEPES (N-2-hydroxyethylpiperazine-N-2-ethanesulfonic acid) buffer) to determine soluble iron in the

media. Fe(II) standards were prepared with ferrous ethylenediammonium sulfate and measured at OD_{562}.

5.8 Acknowledgments

We thank Hannah Lant for help with EPR, Amani Ebrahim and Yang Liu for help with XAS, Catharine Shipps, Jens Neu, and Eric Martz for helpful discussions, Fadel A. Samatey and Yuri Y. Londer for providing purified PpcA protein, Derek Lovley for providing the CL-1 strain, and Cong Shen for providing the Δ*omcS* strain in the CL-1 background. This research used beamline 7-BM (QAS) of the National Synchrotron Light Source II, a U.S. DOE Office of Science User Facility operated for the DOE Office of Science by Brookhaven National Laboratory under Contract No. DE-SC0012704 and 12-BM beamline of the Advanced Photon Source at Argonne National Laboratory, supported by DOE under Contract No. DE-AC02-06CH11357. This research was supported by the National Institutes of Health Director's New Innovator award (1DP2AI138259-01 to N.S.M.), the NSF CAREER award no. 1749662 (to N.S.M.), NSF Early-Concept Grant for Exploratory Research (EAGER) Award No. 2038000. (to N.S.M. and V.S.B.), NSF CHE award no. 1903576 (to A.I.F.), NSF Graduate Research Fellowship award 2017224445 (to J.P.O.), and NIH Training Grant T32 GM007223 (supporting V.S.). Research was sponsored by the Defense Advanced Research Project Agency (DARPA) Army Research Office (ARO) and was accomplished under Cooperative Agreement Number W911NF-18-2-0100 (with N.S.M. and V.S.B.).

6. Conclusions and Future Directions

The discovery of *Geobacter sulfurreducens* and its potential implications on bioremediation and biotechnology has made this soil microbe relevant to due to its pathways and mechanisms to transfer electrons. Years of research have been devoted to forming a better understanding of the mechanisms and proteins that allow *Gs* to transfer electrons over micrometer-long distances. A combination of biochemical, biophysical, and genetic approaches showed that *Gs* pili were important for extracellular electron transfer. These studies showed that alterations to *pilA-N* sequence had a drastic effect on iron reduction and current production phenotypes of the mutant strains. In this work, I have addressed over ten years of controversies where the role of PilA-N was attributed to its mischaracterized electroconductive properties to transfer electrons and not a secretory role to translocate cytochrome-forming nanowires[21,36-39,41-43].

First, we solved the structure of PilA-N filaments where PilA-N and PilA-C form a heterodimer, constituting the subunit of the PilA filament[59]. This structure, in combination with twitching, attachment, and our functional secretion assay demonstrated that *Gs* pili are not the electroconductive appendage, but rather an endopilus-like filament that secretes OmcS and OmcZ nanowires as shown in Chapter 2. My experiments reintroducing native PilA-N into *pilA-N* mutants showed a recovery of both previously affected phenotypes where our complemented Aro5 strain was able to reduce iron and produce a current like that shown by WT in Chapter 3. Furthermore, we show EET at a single-cell level using EFM which confirms that OmcS and OmcZ nanowires are responsible for this phenomenon. Further analysis of the mutations and heterologous

expression of pili in *Gs* demonstrated that deficiencies in iron reduction and current production were due to: 1) the lack of interactions between pili and OmcS and OmcZ; 2) the lower stability of the filament; or 3) the lack of interaction between the nanowires and the expressed pili as shown in Chapter 4. *In silico* analysis demonstrated that PilA-N requires PilA-C for stability and identified 4 Gly residues in its globular domain that allow PilA-C to wrap itself around PilA-N to stabilize the structure of the filament. Finally, we further studied the assembly mechanism of OmcS nanowires by disrupting the axial heme coordination in heme 5 in OmcS. Our $OmcS^{H16A}$ strain showed expression of the OmcS monomer, but was unable to assemble into polymers demonstrating the key role of this residue in nanowire assembly.

The knowledge acquired in this work presents a unique opportunity to further advance the role of *Gs* in bioremediation and biomaterials. This work has characterized the role of pili and has opened up the possibility to engineer electroconductive bacteria capable of reducing metal oxides in nature without the limitations of a slow doubling time and anoxic needs. In this work we built on the work of Ueki *et al.* utilizing *E. coli* as a chassis for this electroconductive strain[251]. I have utilized this system to introduce both PilA-N and PilA-C to optimize the expression and purification of PilA-N-C filaments as seen in Chapter 5. This system will allow us to test various constructs to alter PilA-C to have a better understanding of pilus dynamics and stability as seen in our *in silico* experiments. Furthermore, if we can purify larger quantities of PilA filaments with ease, we will be able to test protein-protein interactions with other nanowires and cytochromes to elucidate the mechanisms through which PilA filaments translocate nanowires into the extracellular environment. Although some of the players that allow *Gs* to conduct EET have been

characterized, there are still components or interactions that have not been investigated yet. Producing large quantities of PilA filaments will allow us to design screens through pull-down assays to identify these interactions. Through surface plasmon resonance, we will further characterize the dynamics of said interactions to build a model that explains the role of PilA filaments in EET.

The story of *Gs* has been intertwined with mystery and excitement. Since its discovery, it has captivated many generations of scientists with its electroconductive appendages capable of reducing metal oxides in the soil and its bioremediation and biomaterials potential. This work has shown that said appendages are composed of cytochrome-forming nanowires and, that the formerly called e-pili, are an endopilus-like filament involved in nanowire translocation. Further studies will have to be conducted to identify and characterize the components that allow *Gs* to transfer electrons and assemble the minimum required components to achieve EET in other bacteria. The road to this achievement is still long, but the insight provided by this work has paved the way for future generations to accomplish this feat.

7. References

1 Radlinski, L. C. & Baumler, A. J. To breathe or not to breathe? *Elife* **11** (2022). https://doi.org:10.7554/eLife.79593

2 Price, E. E., Roman-Rodriguez, F. & Boyd, J. M. Bacterial approaches to sensing and responding to respiration and respiration metabolites. *Mol Microbiol* **116**, 1009-1021 (2021). https://doi.org:10.1111/mmi.14795

3 Ueki, T. Cytochromes in Extracellular Electron Transfer in Geobacter. *Appl Environ Microbiol* **87** (2021). https://doi.org:10.1128/AEM.03109-20

4 Liu, D. F. & Li, W. W. Potential-dependent extracellular electron transfer pathways of exoelectrogens. *Curr Opin Chem Biol* **59**, 140-146 (2020). https://doi.org:10.1016/j.cbpa.2020.06.005

5 Wang, W. & Lee, D. J. Direct interspecies electron transfer mechanism in enhanced methanogenesis: A mini-review. *Bioresour Technol* **330**, 124980 (2021). https://doi.org:10.1016/j.biortech.2021.124980

6 Mei, R. *et al.* Novel Geobacter species and diverse methanogens contribute to enhanced methane production in media-added methanogenic reactors. *Water Res* **147**, 403-412 (2018). https://doi.org:10.1016/j.watres.2018.10.026

7 Mostafa, A., Im, S., Song, Y.-C., Ahn, Y. & Kim, D.-H. Enhanced Anaerobic Digestion by Stimulating DIET Reaction. *Processes* **8** (2020). https://doi.org:10.3390/pr8040424

8 Summers, F., Leang, Franks, Malvankar, Lovley. Direct Exchange of Electrons Within Aggregates of an Evolved Syntrophic Coculture of Anaerobic Bacteria. *Science* **330** (2010).

9 Childers, S. E., Ciufo, S., & Lovely, D. Geobacter metallireducens accesses insoluble Fe(III) oxide by chemotaxis. *Nature*, 767-769 (2002).

10 Phillips, L. J. C. Phylogenetic Analysis of Dissimilatory Fe(III)-Reducing Bacteria. *J Bacteriol* **178**, 2402-2408 (1996).

11 Newman, H. Extracellular electron transfer. *Cellular and Molecular Life Sciences* **58** (2001).

12 Aklujkar, M. *et al.* Proteins involved in electron transfer to Fe(III) and Mn(IV) oxides by Geobacter sulfurreducens and Geobacter uraniireducens. *Microbiology* **159**, 515-535 (2013). https://doi.org:10.1099/mic.0.064089-0

13 Rollefson, J. B., Stephen, C. S., Tien, M. & Bond, D. R. Identification of an extracellular polysaccharide network essential for cytochrome anchoring and biofilm formation in Geobacter sulfurreducens. *J Bacteriol* **193**, 1023-1033 (2011). https://doi.org:10.1128/JB.01092-10

14 Cologgi, D. L., Lampa-Pastirk, S., Speers, A. M., Kelly, S. D. & Reguera, G. Extracellular reduction of uranium via Geobacter conductive pili as a protective cellular mechanism. *Proc Natl Acad Sci U S A* **108**, 15248-15252 (2011). https://doi.org:10.1073/pnas.1108616108

15 Rollefson, J. B., Levar, C. E. & Bond, D. R. Identification of genes involved in biofilm formation and respiration via mini-Himar transposon mutagenesis of Geobacter sulfurreducens. *J Bacteriol* **191**, 4207-4217 (2009). https://doi.org:10.1128/JB.00057-09

16 Yi, H. *et al.* Selection of a variant of Geobacter sulfurreducens with enhanced capacity for current production in microbial fuel cells. *Biosens Bioelectron* **24**, 3498-3503 (2009). https://doi.org:10.1016/j.bios.2009.05.004

17 Inoue, K. *et al.* Purification and characterization of OmcZ, an outer-surface, octaheme c-type cytochrome essential for optimal current production by Geobacter sulfurreducens. *Appl Environ Microbiol* **76**, 3999-4007 (2010). https://doi.org:10.1128/AEM.00027-10

18 Leang, C. *et al.* Adaptation to disruption of the electron transfer pathway for Fe(III) reduction in Geobacter sulfurreducens. *J Bacteriol* **187**, 5918-5926 (2005). https://doi.org:10.1128/JB.187.17.5918-5926.2005

19 Lovley, D. R. *et al.* Geobacter: the microbe electric's physiology, ecology, and practical applications. *Adv Microb Physiol* **59**, 1-100 (2011). https://doi.org:10.1016/B978-0-12-387661-4.00004-5

20 Butler, J. E., Kaufmann, F., Coppi, M. V., Nunez, C. & Lovley, D. R. MacA, a diheme c-type cytochrome involved in Fe(III) reduction by Geobacter sulfurreducens. *J Bacteriol* **186**, 4042-4045 (2004). https://doi.org:10.1128/JB.186.12.4042-4045.2004

21 Reguera, G. *et al.* Extracellular electron transfer via microbial nanowires. *Nature* **435**, 1098-1101 (2005).

22 Mattick, J. S. Type IV pili and twitching motility. *Annu Rev Microbiol* **56**, 289-314 (2002). https://doi.org:10.1146/annurev.micro.56.012302.160938

23 Hager, A. J. *et al.* Type IV pili-mediated secretion modulates Francisella virulence. *Mol Microbiol* **62**, 227-237 (2006). https://doi.org:10.1111/j.1365-2958.2006.05365.x

24 Craig, L. *et al.* Type IV pilus structure by cryo-electron microscopy and crystallography: implications for pilus assembly and functions. *Mol Cell* **23**, 651-662 (2006). https://doi.org:10.1016/j.molcel.2006.07.004

25 Giltner, C. L., Nguyen, Y. & Burrows, L. L. Type IV pilin proteins: versatile molecular modules. *Microbiol Mol Biol Rev* **76**, 740-772 (2012). https://doi.org:10.1128/MMBR.00035-12

26 Craig, L., Forest, K. T. & Maier, B. Type IV pili: dynamics, biophysics and functional consequences. *Nat Rev Microbiol* **17**, 429-440 (2019). https://doi.org:10.1038/s41579-019-0195-4

27 Coppi, M. V., Leang, C., Sandler, S. J. & Lovley, D. R. Development of a genetic system for *Geobacter sulfurreducens*. *Appl Environ Microbiol* **67**, 3180-3187 (2001). https://doi.org:10.1128/AEM.67.7.3180-3187.2001

28 Leang, C., Coppi, M. V. & Lovley, D. R. OmcB, a c-type polyheme cytochrome, involved in Fe(III) reduction in Geobacter sulfurreducens. *J Bacteriol* **185**, 2096-2103 (2003). https://doi.org:10.1128/jb.185.7.2096-2103.2003

29 Lovley, L. L. H. M. C. C. M. S. Biochemical and genetic characterization of PpcA, a periplasmic c-type cytochrome in Geobacter sulfurreducens. *Biochem J* **369** (2003).

30 Mehta, T., Coppi, M. V., Childers, S. E. & Lovley, D. R. Outer membrane c-type cytochromes required for Fe(III) and Mn(IV) oxide reduction in *Geobacter sulfurreducens*. *Appl Environ Microbiol* **71**, 8634-8641 (2005). https://doi.org:10.1128/AEM.71.12.8634-8641.2005

31 Nevin, K. P. *et al.* Anode biofilm transcriptomics reveals outer surface components essential for high density current production in *Geobacter sulfurreducens* fuel cells. *PLoS One* **4**, e5628 (2009). https://doi.org:10.1371/journal.pone.0005628

32 Juarez, K. *et al.* PilR, a transcriptional regulator for pilin and other genes required for Fe(III) reduction in Geobacter sulfurreducens. *J Mol Microbiol Biotechnol* **16**, 146-158 (2009). https://doi.org:10.1159/000115849

33 Kilmury, S. L. N. & Burrows, L. L. The Pseudomonas aeruginosa PilSR Two-Component System Regulates Both Twitching and Swimming Motilities. *MBio* **9** (2018). https://doi.org:10.1128/mBio.01310-18

34 Hernandez-Eligio, A., Andrade, A., Soto, L., Morett, E. & Juarez, K. The unphosphorylated form of the PilR two-component system regulates pilA gene expression in Geobacter sulfurreducens. *Environ Sci Pollut Res Int* **24**, 25693-25701 (2017). https://doi.org:10.1007/s11356-016-6192-5

35 Kilmury, S. L. & Burrows, L. L. Type IV pilins regulate their own expression via direct intramembrane interactions with the sensor kinase PilS. *Proc Natl Acad Sci U S A* **113**, 6017-6022 (2016). https://doi.org:10.1073/pnas.1512947113

36 Leang, C., Qian, X., Mester, T. & Lovley, D. R. Alignment of the c-type cytochrome OmcS along pili of Geobacter sulfurreducens. *Appl Environ Microbiol* **76**, 4080-4084 (2010). https://doi.org:10.1128/AEM.00023-10

37 Malvankar, N. S. *et al.* Tunable metallic-like conductivity in microbial nanowire networks. *Nat Nanotechnol* **6**, 573-579 (2011). https://doi.org:10.1038/nnano.2011.119

38 Vargas, M. *et al.* Aromatic amino acids required for pili conductivity and long-range extracellular electron transport in *Geobacter sulfurreducens*. *mBio* **4**, e00105-00113 (2013). https://doi.org:10.1128/mBio.00105-13

39 Tan, Y. *et al.* Synthetic Biological Protein Nanowires with High Conductivity. *Small* **12**, 4481-4485 (2016). https://doi.org:10.1002/smll.201601112

40 Yalcin, S. E. *et al.* Electric field stimulates production of highly conductive microbial OmcZ nanowires. *Nat Chem Biol* **16**, 1136-1142 (2020). https://doi.org:10.1038/s41589-020-0623-9

41 Tan, Y. *et al.* The Low Conductivity of Geobacter uraniireducens Pili Suggests a Diversity of Extracellular Electron Transfer Mechanisms in the Genus Geobacter. *Front Microbiol* **7**, 980 (2016). https://doi.org:10.3389/fmicb.2016.00980

42 Liu, X. *et al.* A Geobacter sulfurreducens strain expressing pseudomonas aeruginosa type IV pili localizes OmcS on pili but is deficient in Fe(III) oxide reduction and current production. *Appl Environ Microbiol* **80**, 1219-1224 (2014). https://doi.org:10.1128/AEM.02938-13

43 Tan, Y. *et al.* Expressing the Geobacter metallireducens PilA in Geobacter sulfurreducens Yields Pili with Exceptional Conductivity. *mBio* **8** (2017). https://doi.org:10.1128/mBio.02203-16

44 Wang, F. *et al.* Structure of Microbial Nanowires Reveals Stacked Hemes that Transport Electrons over Micrometers. *Cell* **177**, 361-369 e310 (2019). https://doi.org:10.1016/j.cell.2019.03.029

45 Gu, Y. *et al.* Structure of Geobacter cytochrome OmcZ identifies mechanism of nanowire assembly and conductivity. *Nat Microbiol* **8**, 284-298 (2023). https://doi.org:10.1038/s41564-022-01315-5

46 Wang, F. *et al.* Structure of microbial nanowires reveals stacked hemes that transport electrons over micrometers. *Cell* **177**, 361-369 (2019). https://doi.org:https://doi.org/10.1016/j.cell.2019.03.029

47 Filman, D. J. *et al.* Cryo-EM reveals the structural basis of long-range electron transport in a cytochrome-based bacterial nanowire. *Communications Biology* **2**, 219 (2019).

48 Yalcin, S. E. *et al.* Electric field stimulates production of highly conductive microbial OmcZ nanowires. *Nature Chemical Biology* **16**, 1136-1142 (2020). https://doi.org:10.1038/s41589-020-0623-9

49 Malvankar, N. S. *et al.* Tunable metallic-like conductivity in microbial nanowire networks. *Nature Nanotechnology* **6**, 573-579 (2011).

50 Michel, G. P. & Voulhoux, R. in *Bacterial Secreted Proteins: Secretory Mechanisms and Role in Pathogenesis* (ed K. Wooldridge) 67-92 (Caister Academic, 2009).

51 Malvankar, N. S., Tuominen, M. T. & Lovley, D. R. Lack of cytochrome involvement in long-range electron transport through conductive biofilms and nanowires of Geobacter sulfurreducens. *Energy & Environmental Science* **5** (2012). https://doi.org:10.1039/c2ee22330a

52 Yalcin, S. E. & Malvankar, N. The blind men and the filament: Understanding structures and functions of microbial nanowires *Current Opinion in Chemical Biology* **59**, 193-201 (2020).

53 Liu, X., Zhuo, S., Rensing, C. & Zhou, S. Syntrophic growth with direct interspecies electron transfer between pili-free *Geobacter* species. *The ISME Journal* **12**, 2142–2151 (2018). https://doi.org:10.1038/s41396-018-0193-y

54 Richter, L. V., Sandler, S. J. & Weis, R. M. Two isoforms of *Geobacter sulfurreducens* PilA have distinct roles in pilus biogenesis, cytochrome localization, extracellular electron transfer, and biofilm formation. *Journal of Bacteriology* **194**, 2551-2563 (2012). https://doi.org:10.1128/jb.06366-11

55 Wang, F. *et al.* Structure of Geobacter OmcZ filaments suggests extracellular cytochrome polymers evolved independently multiple times. *Elife* **11** (2022). https://doi.org:10.7554/eLife.81551

56 Mehta, T., Childers, S. E., Glaven, R., Lovley, D. R. & Mester, T. A putative multicopper protein secreted by an atypical type II secretion system involved in the reduction of insoluble electron acceptors in Geobacter sulfurreducens. *Microbiology* **152**, 2257-2264 (2006). https://doi.org:10.1099/mic.0.28864-0

57 Ordonez, M. V., Schrott, G. D., Massazza, D. A. & Busalmen, J. P. The relay network of Geobacter biofilms. *Energy & Environmental Science* **9**, 2677-2681 (2016). https://doi.org:10.1039/C6EE01699E

58 Reardon, P. N. & Mueller, K. T. Structure of the type IVa major pilin from the electrically conductive bacterial nanowires of Geobacter sulfurreducens. *J Biol Chem* **288**, 29260-29266 (2013). https://doi.org:10.1074/jbc.M113.498527

59 Gu, Y., Srinkanth, V. , Salazar-Morales, A.I., Jain, R., Gubberman-Pfeffer, M., O'Brien, J.P., Yi, S.M., Soni, R.K., Samatey, F.A., Ebru Yalcin, S., Batista, V.S., Malbankar, N.S. Heterodimeric structure of Geobacter pili reveals low conductivity and a role in the secretion of microbial nanowires. *Nature* (2021).

60 Chang, Y. W. *et al.* Architecture of the type IVa pilus machine. *Science* **351**, aad2001 (2016). https://doi.org:10.1126/science.aad2001

61 Vignon, G. *et al.* Type IV-like pili formed by the type II secreton: specificity, composition, bundling, polar localization, and surface presentation of peptides. *J Bacteriol* **185**, 3416-3428 (2003). https://doi.org:10.1128/jb.185.11.3416-3428.2003

62 Shi, L. *et al.* Direct involvement of type II secretion system in extracellular translocation of *Shewanella oneidensis* outer membrane cytochromes MtrC and OmcA. *Journal of bacteriology* **190**, 5512-5516 (2008).

63 Shu, C., Xiao, K., Yan, Q. & Sun, X. Comparative analysis of Type IV pilin in *Desulfuromonadales*. *Frontiers in Microbiology* **7**, 2080 (2016).

64 O'Brien, J. P. & Malvankar, N. S. A simple and low-cost procedure for growing *Geobacter sulfurreducens* cell cultures and biofilms in bioelectrochemical systems. *Current Protocols in Microbiology* **43**, A.4K.1-A.4K.27 (2017). https://doi.org:10.1002/cpmc.20

65 Liu, X., Zhan, J., Jing, X., Zhou, S. & Lovley, D. R. A pilin chaperone required for the expression of electrically conductive *Geobacter sulfurreducens* pili. *Environmental Microbiology* (2019).

66 Vignon, G. *et al.* Type IV-like pili formed by the type II secreton: specificity, composition, bundling, polar localization, and surface presentation of peptides. *Journal of bacteriology* **185**, 3416-3428 (2003).

67 Durand, É. *et al.* XcpX controls biogenesis of the *Pseudomonas aeruginosa* XcpT-containing pseudopilus. *Journal of Biological Chemistry* **280**, 31378-31389 (2005).

68 Wang, F. *et al.* Cryoelectron microscopy reconstructions of the *Pseudomonas aeruginosa* and *Neisseria gonorrhoeae* type IV pili at sub-nanometer resolution. *Structure* **25**, 1423-1435 (2017). https://doi.org:10.1016/j.str.2017.07.016

69 Craig, L., Pique, M. E. & Tainer, J. A. Type IV pilus structure and bacterial pathogenicity. *Nature Review Microbiology* **2**, 363-378 (2004).

70 Lopez-Castilla, A. *et al.* Structure of the calcium-dependent type 2 secretion pseudopilus. *Nature Microbiology* **2**, 1686-1695 (2017).

71 Li, J., Egelman, E. H. & Craig, L. Structure of the *Vibrio cholerae* type IVb pilus and stability comparison with the *Neisseria gonorrhoeae* type IVa pilus. *Journal of Molecular Biology* **418**, 47-64 (2012). https://doi.org:http://dx.doi.org/10.1016/j.jmb.2012.02.017

72 Feliciano, G. T., da Silva, A. J., Reguera, G. & Artacho, E. Molecular and electronic structure of the peptide subunit of Geobacter sulfurreducens conductive pili from first principles. *J Phys Chem A* **116**, 8023-8030 (2012). https://doi.org:10.1021/jp302232p

73 Mehta, T., Childers, S. E., Glaven, R., Lovley, D. R. & Mester, T. A putative multicopper protein secreted by an atypical type II secretion system involved in the reduction of insoluble electron acceptors in *Geobacter sulfurreducens*. *Microbiology* **152**, 2257-2264 (2006).

74 Bouhenni, R. A. *et al.* The role of *Shewanella oneidensis* MR-1 outer surface structures in extracellular electron transfer. *Electroanalysis* **22**, 856-864 (2010). https://doi.org:10.1002/elan.200880006

75 Liu, X. *et al.* A *Geobacter sulfurreducens* strain expressing *Pseudomonas aeruginosa* type IV pili localizes OmcS on pili but is deficient in Fe(III) oxide reduction and current production. *Applied and Environmental Microbiology* **80**, 1219-1224 (2014).

76 Liu, X., Ye, Y., Xiao, K., Rensing, C. & Zhou, S. Molecular evidence for the adaptive evolution of *Geobacter sulfurreducens* to perform dissimilatory iron reduction in natural environments. *Molecular Microbiology* **113**, 783-793 (2019).

77 Craig, L., Forest, K. T. & Maier, B. Type IV pili: dynamics, biophysics and functional consequences. *Nature Reviews Microbiology* **17**, 429-440 (2019). https://doi.org:10.1038/s41579-019-0195-4

78 Nivaskumar, M. *et al.* Distinct docking and stabilization steps of the Pseudopilus conformational transition path suggest rotational assembly of type IV pilus-like fibers. *Structure* **22**, 685-696 (2014). https://doi.org:10.1016/j.str.2014.03.001

79 Durand, E. *et al.* The assembly mode of the pseudopilus: a hallmark to distinguish a novel secretion system subtype. *J Biol Chem* **286**, 24407-24416 (2011). https://doi.org:10.1074/jbc.M111.234278

80 Douzi, B., Filloux, A. & Voulhoux, R. On the path to uncover the bacterial type II secretion system. *Philos Trans R Soc Lond B Biol Sci* **367**, 1059-1072 (2012). https://doi.org:10.1098/rstb.2011.0204

81 Liu, X. *et al.* A *Geobacter sulfurreducens* Strain Expressing *Pseudomonas aeruginosa* Type IV Pili Localizes OmcS on Pili but Is Deficient in Fe(III) Oxide Reduction and Current Production. *Appl Environ Microb* **80**, 1219-1224 (2014). https://doi.org:10.1128/Aem.02938-13

82 Tan, Y. *et al.* The Low Conductivity of *Geobacter uraniireducens* Pili Suggests a Diversity of Extracellular Electron Transfer Mechanisms in the Genus *Geobacter*. *Front Microbiol* **7**, 980 (2016). https://doi.org:10.3389/fmicb.2016.00980

83 O'Brien, J. P. & Malvankar, N. S. A Simple and Low-Cost Procedure for Growing *Geobacter sulfurreducens* Cell Cultures and Biofilms in Bioelectrochemical Systems. *Curr Protoc Microbiol* **43**, A 4K 1-A 4K 27 (2016). https://doi.org:10.1002/cpmc.20

84 Chan, C. H., Levar, C. E., Zacharoff, L., Badalamenti, J. P. & Bond, D. R. Scarless Genome Editing and Stable Inducible Expression Vectors for *Geobacter sulfurreducens*. *Appl Environ Microbiol* **81**, 7178-7186 (2015). https://doi.org:10.1128/AEM.01967-15

85 Kumar, S., Stecher, G., Li, M., Knyaz, C. & Tamura, K. MEGA X: Molecular Evolutionary Genetics Analysis across Computing Platforms. *Mol Biol Evol* **35**, 1547-1549 (2018). https://doi.org:10.1093/molbev/msy096

86 Guindon, S. *et al.* New algorithms and methods to estimate maximum-likelihood phylogenies: assessing the performance of PhyML 3.0. *Syst Biol* **59**, 307-321 (2010). https://doi.org:10.1093/sysbio/syq010

87 Lefort, V., Longueville, J. E. & Gascuel, O. SMS: Smart Model Selection in PhyML. *Mol Biol Evol* **34**, 2422-2424 (2017). https://doi.org:10.1093/molbev/msx149

88 Yu, G. C., Smith, D. K., Zhu, H. C., Guan, Y. & Lam, T. T. Y. GGTREE: an R package for visualization and annotation of phylogenetic trees with their covariates and other associated data. *Methods Ecol Evol* **8**, 28-36 (2017). https://doi.org:10.1111/2041-210x.12628

89 Team, R. C. R: A language and environment for statistical computing. (2013).

90 Shevchenko, A., Tomas, H., Havlis, J., Olsen, J. V. & Mann, M. In-gel digestion for mass spectrometric characterization of proteins and proteomes. *Nat Protoc* **1**, 2856-2860 (2006). https://doi.org:10.1038/nprot.2006.468

91 Cox, J. & Mann, M. MaxQuant enables high peptide identification rates, individualized ppb-range mass accuracies and proteome-wide protein quantification. *Nature biotechnology* **26**, 1367-1372 (2008).

92 Zivanov, J. *et al.* New tools for automated high-resolution cryo-EM structure determination in RELION-3. *Elife* **7**, e42166 (2018). https://doi.org:10.7554/eLife.42166

93 Zhang, K. Gctf: Real-time CTF determination and correction. *J Struct Biol* **193**, 1-12 (2016). https://doi.org:10.1016/j.jsb.2015.11.003

94 Desfosses, A., Ciuffa, R., Gutsche, I. & Sachse, C. SPRING - an image processing package for single-particle based helical reconstruction from electron cryomicrographs. *J Struct Biol* **185**, 15-26 (2014). https://doi.org:10.1016/j.jsb.2013.11.003

95 He, S. & Scheres, S. H. W. Helical reconstruction in RELION. *J Struct Biol* **198**, 163-176 (2017). https://doi.org:10.1016/j.jsb.2017.02.003

96 Egelman, E. H. The iterative helical real space reconstruction method: surmounting the problems posed by real polymers. *J Struct Biol* **157**, 83-94 (2007). https://doi.org:10.1016/j.jsb.2006.05.015

97 Zivanov, J., Nakane, T. & Scheres, S. H. W. A Bayesian approach to beam-induced motion correction in cryo-EM single-particle analysis. *IUCrJ* **6**, 5-17 (2019). https://doi.org:10.1107/S205225251801463X

98 Pettersen, E. F. *et al.* UCSF Chimera--a visualization system for exploratory research and analysis. *J Comput Chem* **25**, 1605-1612 (2004). https://doi.org:10.1002/jcc.20084

99 Emsley, P. & Cowtan, K. Coot: model-building tools for molecular graphics. *Acta Crystallogr D Biol Crystallogr* **60**, 2126-2132 (2004). https://doi.org:10.1107/S0907444904019158

100 Afonine, P. V. *et al.* Real-space refinement in *PHENIX* for cryo-EM and crystallography. *Acta Crystallogr D Struct Biol* **74**, 531-544 (2018). https://doi.org:10.1107/S2059798318006551

101 Nečas, D. & Klapetek, P. Gwyddion: an open-source software for SPM data analysis. *Open Phys* **10**, 181-188 (2012). https://doi.org:10.2478/s11534-011-0096-2

102 Liu, X., Zhan, J., Jing, X., Zhou, S. & Lovley, D. R. A pilin chaperone required for the expression of electrically conductive *Geobacter sulfurreducens* pili. *Environ Microbiol* **21**, 2511-2522 (2019). https://doi.org:10.1111/1462-2920.14638

103 Tan, Y. *et al.* The low conductivity of *Geobacter uraniireducens* pili suggests a diversity of extracellular electron transfer mechanisms in the genus *Geobacter*. *Frontiers in Microbiology* **7**, 980 (2016). https://doi.org:10.3389/fmicb.2016.00980

104 Gorby, Y. A. *et al.* Electrically conductive bacterial nanowires produced by *Shewanella oneidensis* strain MR-1 and other microorganisms. *Proceedings of the National Academy of Sciences* **103**, 11358-11363 (2006). https://doi.org:10.1073/pnas.0604517103

105 Walker, D. J. *et al.* The archaellum of *Methanospirillum hungatei* is electrically conductive. *mbio* **10**, e00579-00519 (2019).

106 Walker, D. J. *et al.* Electrically conductive pili from pilin genes of phylogenetically diverse microorganisms. *The ISME journal* **12**, 48-58 (2018).

107 Childers, S. E., Ciufo, S. & Lovley, D. R. *Geobacter metallireducens* accesses insoluble Fe(III) oxide by chemotaxis. *Nature* **416**, 767-769 (2002).

108 Reguera, G. *et al.* Biofilm and nanowire production leads to increased current in *Geobacter sulfurreducens* fuel cells. *Applied and Environmental Microbiology* **72**, 7345-7348 (2006). https://doi.org:10.1128/AEM.01444-06

109 Summers, Z. M. *et al.* Direct exchange of electrons within aggregates of an evolved syntrophic coculture of anaerobic bacteria. *Science* **330**, 1413-1415 (2010).

110 Walker, D. J. *et al.* Syntrophus conductive pili demonstrate that common hydrogen-donating syntrophs can have a direct electron transfer option. *The ISME Journal* **14**, 837-846 (2020).

111 Poweleit, N. *et al.* CryoEM structure of the *Methanospirillum hungatei* archaellum reveals structural features distinct from the bacterial flagellum and type IV pilus. *Nature Microbiology* **2**, 16222 (2016). https://doi.org:10.1038/nmicrobiol.2016.222

112 Wegener, G., Krukenberg, V., Riedel, D., Tegetmeyer, H. E. & Boetius, A. Intercellular wiring enables electron transfer between methanotrophic archaea and bacteria. *Nature* **526**, 587-590 (2015). https://doi.org:10.1038/nature15733

113 Rotaru, A.-E. *et al.* A new model for electron flow during anaerobic digestion: direct interspecies electron transfer to Methanosaeta for the reduction of carbon dioxide to methane. *Energy & Environmental Science* **7**, 408-415 (2014).

114 Levar, C., Rollefson, J. & Bond, D. in *Microbial Metal Respiration: From Geochemistry to Potential Applications* (eds Johannes Gescher & Andreas Kappler) 29-48 (Springer 2012).

115 Gu, Y. *et al.* Structure of *Geobacter* pili reveals secretory rather than nanowire behavior. *Nature* **597**, 430-434 (2021).

116 Nevin, K. P. & Lovley, D. R. Mechanisms for Fe(III) oxide reduction in sedimentary environments. *Geomicrobiology Journal* **19**, 141-159 (2002). https://doi.org:10.1080/01490450252864253

117 Kim, M. K., Ingremeau, F., Zhao, A., Bassler, B. L. & Stone, H. A. Local and global consequences of flow on bacterial quorum sensing. *Nature Microbiology* **1**, 15005 (2016).

118 Wang, F. *et al.* Cryo-EM structure of an extracellular *Geobacter* OmcE cytochrome filament reveals tetrahaem packing. *Nature Microbiology* **7**, 1291-1300 (2022). https://doi.org:10.1038/s41564-022-01159-z

119 Wang, F. *et al.* Structure of *Geobacter* OmcZ filaments suggests extracellular cytochrome polymers evolved independently multiple times. *eLife* **11**, e81551 (2022). https://doi.org:10.7554/eLife.81551

120 Gu, Y. *et al.* Structure of *Geobacter* cytochrome OmcZ identifies mechanism of nanowire assembly and conductivity. *Nature Microbiology* **DOI:10.1038/s41564-022-01315-5**, https://yale.app.box.com/s/w7qtietdclao79xnzlrotow77icc77qpgu (2022).

121 Wang, F., Craig, L., Liu, X., Rensing, C. & Egelman, E. H. Microbial nanowires: type IV pili or cytochrome filaments? *Trends in Microbiology* (2022). https://doi.org:https://doi.org/10.1016/j.tim.2022.11.004

122 Yalcin, S. E. & Malvankar, N. S. Seeing is believing: Novel imaging methods help identify structure and function of *Geobacter* nanowires in electricity-producing biofilms in Roadmap on emerging concepts in the physical biology of bacterial biofilms: from surface sensing to community formation *Physical Biology* **18**, 051501 (2021).

123 Clarke, T. A. & Edwards, M. J. Uncovering nature's electronics. *Nature Chemical Biology* **16**, 1041-1042 (2020).

124 Mehta, T., Coppi, M. V., Childers, S. E. & Lovley, D. R. Outer membrane *c*-type cytochromes required for Fe (III) and Mn (IV) oxide reduction in *Geobacter*

sulfurreducens. *Applied and Environmental Microbiology* **71**, 8634-8641 (2005). https://doi.org:10.1128/aem.71.12.8634-8641.2005

125 Nevin, K. P. *et al.* Anode biofilm transcriptomics reveals outer surface components essential for high density current production in *Geobacter sulfurreducens* fuel cells. *PLoS ONE* **4**, e5628 (2009).

126 Lovley, D. R. Untangling *Geobacter sulfurreducens* Nanowires. *mBio*, e00850-00822 (2022). https://doi.org:doi:10.1128/mbio.00850-22

127 Lovley, D. R. On the existence of pilin-based microbial nanowires. *Frontiers in Microbiology* **13** (2022). https://doi.org:10.3389/fmicb.2022.872610

128 Liu, X., Walker, D. J., Nonnenmann, S. S., Sun, D. & Lovley, D. R. Direct observation of electrically conductive pili emanating from *Geobacter sulfurreducens*. *Mbio* **12**, e02209-02221 (2021).

129 Ueki, T. *et al.* Decorating the outer surface of microbially produced protein nanowires with peptides. *ACS synthetic biology* **8**, 1809-1817 (2019).

130 Cologgi, D. L., Lampa-Pastirk, S., Speers, A. M., Kelly, S. D. & Reguera, G. Extracellular reduction of uranium via *Geobacter* conductive pili as a protective cellular mechanism. *Proceedings of the National Academy of Sciences* **108**, 15248-15252 (2011).

131 Vargas, M. *et al.* Aromatic amino acids required for pili conductivity and long-range extracellular electron transport in *Geobacter sulfurreducens*. *mBio* **4**, e00105-00113 (2013).

132 Malvankar, N. S., Tuominen, M. T. & Lovley, D. R. Lack of cytochrome involvement in long-range electron transport through conductive biofilms and nanowires of *Geobacter sulfurreducens*. *Energy & Environmental Science* **5**, 8651-8659 (2012).

133 Inoue, K. *et al.* Specific localization of the *c*-type cytochrome OmcZ at the anode surface in current-producing biofilms of *Geobacter sulfurreducens*. *Environmental Microbiology Reports* **3**, 211-217 (2010). https://doi.org:10.1111/j.1758-2229.2010.00210.x

134 Chadwick, G. L., Otero, F. J., Gralnick, J. A., Bond, D. R. & Orphan, V. J. NanoSIMS imaging reveals metabolic stratification within current-producing biofilms. *Proceedings of the National Academy of Sciences* **116**, 20716-20724 (2019).

135 Steidl, R. J., Lampa-Pastirk, S. & Reguera, G. Mechanistic stratification in electroactive biofilms of Geobacter sulfurreducens mediated by pilus nanowires. *Nature Communications* **7** (2016). https://doi.org:10.1038/ncomms12217

136 Lovley, D. R. Live wires: direct extracellular electron exchange for bioenergy and the bioremediation of energy-related contamination. *Energy and Environmental Science* **4**, 4896-4906 (2011). https://doi.org:DOI: 10.1039/C1EE02229F

137 Srikanth, V. *et al.* Reversible assembly of *Geobacter sulfurreducens* cytochrome OmcS nanowires is essential for extracellular electron transfer. *in review* https://yale.box.com/s/me7b9ez6r1qopo7la41an46wjz42az42xpf (2021).

138 Neu, J. *et al.* Microbial biofilms as living photoconductors due to ultrafast electron transfer in cytochrome OmcS nanowires. *Nature Communications* **13**, 1-12 (2022).

139 Yalcin, S. E. *et al.* Direct imaging of charge transport in progressively reduced graphene oxide using electrostatic force microscopy. *ACS Nano* **9**, 2981-2988 (2015). https://doi.org:10.1021/nn507150q

140 Salas, E. C., Sun, Z., Lüttge, A. & Tour, J. M. Reduction of graphene oxide via bacterial respiration. *ACS nano* **4**, 4852-4856 (2010).

141 Kalathil, S. *et al.* Bioinspired synthesis of reduced graphene oxide-wrapped *Geobacter sulfurreducens* as a hybrid electrocatalyst for efficient oxygen evolution reaction. *Chemistry of Materials* **31**, 3686-3693 (2019). https://doi.org:10.1021/acs.chemmater.9b00394

142 Yi, G. *et al.* Bacteria-affinity aminated carbon nanotubes bridging reduced graphene oxide for highly efficient microbial electrocatalysis. *Environmental Research* **191**, 110212 (2020). https://doi.org:https://doi.org/10.1016/j.envres.2020.110212

143 Malvankar, N. S., Yalcin, S. E., Tuominen, M. T. & Lovley, D. R. Visualization of charge propagation along individual pili proteins using ambient electrostatic force microscopy. *Nature Nanotechnology* **9**, 1012-1017 (2014).

144 Chan, C. H., Levar, C. E., Zacharoff, L., Badalamenti, J. P. & Bond, D. R. Scarless genome editing and stable inducible expression vectors for *Geobacter sulfurreducens*. *Appl. Environ. Microbiol.* **81**, 7178-7186 (2015).

145 Levar, C. E., Hoffman, C. L., Dunshee, A. J., Toner, B. M. & Bond, D. R. Redox potential as a master variable controlling pathways of metal reduction by *Geobacter sulfurreducens*. *The ISME journal* **11**, 741-752 (2017).

146 Kleber, M. *et al.* Dynamic interactions at the mineral–organic matter interface. *Nature Reviews Earth & Environment*, 1-20 (2021).

147 J O'Loughlin, E., A Gorski, C. & M Scherer, M. Effects of phosphate on secondary mineral formation during the bioreduction of akaganeite (β-FeOOH): Green rust versus framboidal magnetite. *Current Inorganic Chemistry (Discontinued)* **5**, 214-224 (2015).

148 Tan, Y. *et al.* Synthetic biological protein nanowires with high conductivity. *Small* **12**, 4481–4485 (2016).

149 Hernández-Eligio, A. *et al.* GSU1771 regulates extracellular electron transfer and electroactive biofilm formation in Geobacter sulfurreducens: Genetic and electrochemical characterization. *Bioelectrochemistry* **145**, 108101 (2022). https://doi.org:https://doi.org/10.1016/j.bioelechem.2022.108101

150 Nguyen, Y. *et al.* Pseudomonas aeruginosa minor pilins prime type IVa pilus assembly and promote surface display of the PilY1 adhesin. *Journal of Biological Chemistry* **290**, 601-611 (2015).

151 Treuner-Lange, A. *et al.* PilY1 and minor pilins form a complex priming the type IVa pilus in *Myxococcus xanthus*. *Nature communications* **11**, 1-14 (2020).

152 Herfurth, M. *et al.* A noncanonical cytochrome *c* stimulates calcium binding by PilY1 for type IVa pili formation. *Proceedings of the National Academy of Sciences* **119**, e2115061119 (2022). https://doi.org:doi:10.1073/pnas.2115061119

153 Kellenberger, C. A. *et al.* GEMM-I riboswitches from *Geobacter* sense the bacterial second messenger cyclic AMP-GMP. *Proceedings of the National Academy of Sciences* **112**, 5383-5388 (2015). https://doi.org:doi:10.1073/pnas.1419328112

154 Wang, F., Craig, L., Liu, X., Rensing, C. & Egelman, E. H. Microbial nanowires: type IV pili or cytochrome filaments? *Trends in Microbiology* **31**, 384-392 (2023). https://doi.org:https://doi.org/10.1016/j.tim.2022.11.004

155 Holmes, D. E. *et al.* Microarray and genetic analysis of electron transfer to electrodes in *Geobacter sulfurreducens*. *Environmental Microbiology* **8**, 1805-1815 (2006). https://doi.org:10.1111/j.1462-2920.2006.01065.x

156 Leang, C., Malvankar, N. S., Franks, A. E., Nevin, K. P. & Lovley, D. R. Engineering *Geobacter sulfurreducens* to produce a highly cohesive conductive matrix with enhanced capacity for current production. *Energy & Environmental Science* **6**, 1901-1908 (2013).

157 Malvankar, N. S., Tuominen, M. T. & Lovley, D. R. Biofilm conductivity is a decisive variable for high-current-density *Geobacter sulfurreducens* microbial fuel cells. *Energy & Environmental Science* **5**, 5790-5797 (2012).

158 Babauta, J. T., Nguyen, H. D., Harrington, T. D., Renslow, R. & Beyenal, H. pH, redox potential and local biofilm potential microenvironments within *Geobacter sulfurreducens* biofilms and their roles in electron transfer. *Biotechnology and Bioengineering* **109**, 2651-2662 (2012).

159 Fukushima, T. *et al.* The molecular basis for binding of an electron transfer protein to a metal oxide surface. *Journal of the American Chemical Society* **139**, 12647-12654 (2017).

160 Kracher, D. *et al.* Extracellular electron transfer systems fuel cellulose oxidative degradation. *Science* **352**, 1098-1101 (2016). https://doi.org:10.1126/science.aaf3165

161 Coppi, M. V., Leang, C., Sandler, S. J. & Lovley, D. R. Development of a genetic system for *Geobacter sulfurreducens*. *Applied and Environmental Microbiology* **67**, 3180-3187 (2001). https://doi.org:10.1128/aem.67.7.3180-3187.2001

162 Richter, L. V., Sandler, S. J. & Weis, R. M. Two isoforms of Geobacter sulfurreducens PilA have distinct roles in pilus biogenesis, cytochrome localization, extracellular electron transfer, and biofilm formation. *J Bacteriol* **194**, 2551-2563 (2012). https://doi.org:10.1128/JB.06366-11

163 Tan, Y. *et al.* Expressing the *Geobacter metallireducens* PilA in *Geobacter sulfurreducens* yields pili with exceptional conductivity. *mBio* **8**, e02203-02216 (2017).

164 Alexeyev, M. F. The pKNOCK series of broad-host-range mobilizable suicide vectors for gene knockout and targeted DNA insertion into the chromosome of gram-negative bacteria. *Biotechniques* **26**, 824-828 (1999).

165 Nečas, D. & Klapetek, P. Gwyddion: an open-source software for SPM data analysis. *Open Physics* **10**, 181-188 (2012).

166 Chen, J., Yao, B., Li, C. & Shi, G. An improved Hummers method for eco-friendly synthesis of graphene oxide. *Carbon* **64**, 225-229 (2013).

167 Yalcin, S. E., Labastide, J. A., Sowle, D. L. & Barnes, M. D. Spectral properties of multiply charged semiconductor quantum dots. *Nano Letters* **11**, 4425-4430 (2011). https://doi.org:10.1021/nl2026103

168 Yalcin, S. E., Yang, B., Labastide, J. A. & Barnes, M. D. Electrostatic force microscopy and spectral studies of electron attachment to single quantum dots on indium tin oxide substrates. *The Journal of Physical Chemistry C* **116**, 15847-15853 (2012). https://doi.org:10.1021/jp305857d

169 Heim, T., Lmimouni, K. & Vuillaume, D. Ambipolar charge injection and transport in a single pentacene monolayer island. *Nano Letters* **4**, 2145-2150 (2004). https://doi.org:10.1021/nl0487673

170 Dautel, O. J. *et al.* Electroactive nanorods and nanorings designed by supramolecular association of π-conjugated oligomers. *Chemistry – A European Journal* **14**, 4201-4213 (2008). https://doi.org:10.1002/chem.200701638

171 Melin, T., Zdrojek, M. & Brunel, D. in *Scanning Probe Microscopy in Nanoscience and Nanotechnology NanoScience and Technology* (ed Bharat Bhushan) 89-128 (Springer Berlin Heidelberg, 2010).

172 Fumagalli, L., Esteban-Ferrer, D., Cuervo, A., Carrascosa, J. L. & Gomila, G. Label-free identification of single dielectric nanoparticles and viruses with ultraweak polarization forces. *Nature Materials* **11**, 808-816 (2012).

173 Schutz, C. N. & Warshel, A. What are the dielectric "constants" of proteins and how to validate electrostatic models? *Proteins: Structure, Function, and Bioinformatics* **44**, 400-417 (2001). https://doi.org:10.1002/prot.1106

174 Amber 20 (University of California, San Francisco., 2022).

175 Maier, J. A. *et al.* ff14SB: improving the accuracy of protein side chain and backbone parameters from ff99SB. *Journal of chemical theory and computation* **11**, 3696-3713 (2015).

176 Jorgensen, W. L., Chandrasekhar, J., Madura, J. D., Impey, R. W. & Klein, M. L. Comparison of simple potential functions for simulating liquid water. *The Journal of chemical physics* **79**, 926-935 (1983).

177 Joung, I. S. & Cheatham III, T. E. Determination of alkali and halide monovalent ion parameters for use in explicitly solvated biomolecular simulations. *The journal of physical chemistry B* **112**, 9020-9041 (2008).

178 Darden, T., York, D. & Pedersen, L. Particle mesh Ewald: An N· log (N) method for Ewald sums in large systems. *The Journal of chemical physics* **98**, 10089-10092 (1993).

179 Miyamoto, S. & Kollman, P. A. Settle: An Analytical Version of the SHAKE and RATTLE Algorithm for Rigid Water Models. *Journal of Computational Chemistry* **13**, 952-962 (1992).

180 Gotz, A. W. *et al.* Routine microsecond molecular dynamics simulations with AMBER on GPUs. 1. Generalized born. *Journal of chemical theory and computation* **8**, 1542-1555 (2012).

181 Roe, D. R. & Cheatham III, T. E. PTRAJ and CPPTRAJ: software for processing and analysis of molecular dynamics trajectory data. *Journal of chemical theory and computation* **9**, 3084-3095 (2013).

182 Chlebek, J. L., Denise, R., Craig, L. & Dalia, A. B. Motor-independent retraction of type IV pili is governed by an inherent property of the pilus filament. *Proceedings of the National Academy of Sciences* **118**, e2102780118 (2021).

183 Zivanov, J., Nakane, T. & Scheres, S. H. A Bayesian approach to beam-induced motion correction in cryo-EM single-particle analysis. *IUCrJ* **6**, 5-17 (2019).

184 Scheres, S. H. RELION: implementation of a Bayesian approach to cryo-EM structure determination. *Journal of Structural Biology* **180**, 519-530 (2012).

185 Pettersen, E. F. *et al.* UCSF Chimera—a visualization system for exploratory research and analysis. *Journal of computational chemistry* **25**, 1605-1612 (2004).

186 Wolfgang., M., van Putten, J.P.M., Hayes, S.F., Dorward, D.,and Koomey, M. Components and dynamics of fiber formation define a ubiquitous biogenesis pathway for bacterial pili. **19**, 6408-6418 (2000). https://doi.org:10.1093/emboj/19.23.6408

187 Craig, L., Pique, M. E. & Tainer, J. A. Type IV pilus structure and bacterial pathogenicity. *Nat Rev Microbiol* **2**, 363-378 (2004). https://doi.org:10.1038/nrmicro885

188 Karami, Y. *et al.* Computational and biochemical analysis of type IV pilus dynamics and stability. *Structure* **29**, 1397-1409 e1396 (2021). https://doi.org:10.1016/j.str.2021.07.008

189 Bardiaux, B. *et al.* Structure and Assembly of the Enterohemorrhagic Escherichia coli Type 4 Pilus. *Structure* **27**, 1082-1093 e1085 (2019). https://doi.org:10.1016/j.str.2019.03.021

190 Liu, X. *et al.* Biological synthesis of high-conductive pili in aerobic bacterium Pseudomonas aeruginosa. *Appl Microbiol Biotechnol* **103**, 1535-1544 (2019). https://doi.org:10.1007/s00253-018-9484-5

191 Ueki, T. *et al.* An Escherichia coli Chassis for Production of Electrically Conductive Protein Nanowires. *ACS Synth Biol* **9**, 647-654 (2020). https://doi.org:10.1021/acssynbio.9b00506

192 Francetic, O., Buddelmeijer, N., Lewenza, S., Kumamoto, C. A. & Pugsley, A. P. Signal recognition particle-dependent inner membrane targeting of the PulG Pseudopilin component of a type II secretion system. *J Bacteriol* **189**, 1783-1793 (2007). https://doi.org:10.1128/JB.01230-06

193 Hornak, V., Okur, A., Rizzo, R., Simmerling, C. HIV-1 protease flaps spontaneously open and reclose
in molecular dynamics simulations. *PNAS* **103**, 915-920 (2005).

194 Filman, D. J. *et al.* Cryo-EM reveals the structural basis of long-range electron transport in a cytochrome-based bacterial nanowire. *Communications biology* **2**, 1-6 (2019).

195 Vargas, M. *et al.* Aromatic amino acids required for pili conductivity and long-range extracellular electron transport in Geobacter sulfurreducens. *MBio* **4**, e00105-00113 (2013).

196 Tan, Y. *et al.* Synthetic biological protein nanowires with high conductivity. *small* **12**, 4481-4485 (2016).

197 Tan, Y. *et al.* Expressing the Geobacter metallireducens PilA in Geobacter sulfurreducens yields pili with exceptional conductivity. *MBio* **8**, e02203-02216 (2017).

198 Case, D. A. *et al.* The Amber biomolecular simulation programs. *Journal of computational chemistry* **26**, 1668-1688 (2005).

199 D.A. Case, H. M. A., K. Belfon, I.Y. Ben-Shalom, S.R. Brozell, D.S. Cerutti, T.E. Cheatham, III, V.W.D. Cruzeiro, T.A. Darden, R.E. Duke, G. Giambasu, M.K. Gilson, H. Gohlke, A.W. Goetz, R. Harris, S. Izadi, S.A. Izmailov, C. Jin, K. Kasavajhala, M.C. Kaymak, E. King, A. Kovalenko, T. Kurtzman, T.S. Lee, S. LeGrand, P. Li, C. Lin, J. Liu, T. Luchko, R. Luo, M. Machado, V. Man, M. Manathunga, K.M. Merz, Y. Miao, O. Mikhailovskii, G. Monard, H. Nguyen, K.A. O'Hearn, A. Onufriev, F. Pan, S. Pantano, R. Qi, A. Rahnamoun, D.R. Roe, A. Roitberg, C. Sagui, S. Schott-Verdugo, J. Shen, C.L. Simmerling, N.R. Skrynnikov, J. Smith, J. Swails, R.C. Walker, J. Wang, H. Wei, R.M. Wolf, X. Wu, Y. Xue, D.M. York, S. Zhao, and P.A. Kollman. Amber20. *University of California, San Francisco.* (2020).

200 Ryckaert, J.-P., Ciccotti, G. & Berendsen, H. J. Numerical integration of the cartesian equations of motion of a system with constraints: molecular dynamics of n-alkanes. *Journal of computational physics* **23**, 327-341 (1977).

201 Gotz, A. W. *et al.* Routine Microsecond Molecular Dynamics Simulations with AMBER on GPUs. 1. Generalized Born. *J Chem Theory Comput* **8**, 1542-1555 (2012). https://doi.org:10.1021/ct200909j

202 Chlebek, J. L., Denise, R., Craig, L. & Dalia, A. B. Motor-independent retraction of type IV pili is governed by an inherent property of the pilus filament. *Proceedings of the National Academy of Sciences* **118** (2021).

203 Wang, F. *et al.* Structure of Microbial Nanowires Reveals Stacked Hemes that Transport Electrons over Micrometers. *Cell* **177**, 361-369. e310 (2019).

204 Zheng, S. Q. *et al.* MotionCor2: anisotropic correction of beam-induced motion for improved cryo-electron microscopy. *Nature methods* **14**, 331-332 (2017).

205 He, S. & Scheres, S. H. Helical reconstruction in RELION. *Journal of structural biology* **198**, 163-176 (2017).

206 Gray, H. B. & Winkler, J. R. Electron tunneling through proteins. *Q Rev Biophys* **36**, 341-372 (2003). https://doi.org:10.1017/s0033583503003913

207 Reguera, G. Biological electron transport goes the extra mile. *Proc Natl Acad Sci U S A* **115**, 5632-5634 (2018). https://doi.org:10.1073/pnas.1806580115

208 Dempsey, J. L. & Hartings, M. R. Hop to It. *Biochemistry* **56**, 5623-5624 (2017). https://doi.org:10.1021/acs.biochem.7b00950

209 Gorby, Y. A. *et al.* Electrically conductive bacterial nanowires produced by *Shewanella oneidensis* strain MR-1 and other microorganisms. *Proc Natl Acad Sci U S A* **103**, 11358-11363 (2006). https://doi.org:10.1073/pnas.0604517103

210 El-Naggar, M. Y. *et al.* Electrical transport along bacterial nanowires from Shewanella oneidensis MR-1. *Proc Natl Acad Sci U S A* **107**, 18127-18131 (2010). https://doi.org:10.1073/pnas.1004880107

211 Bjerg, J. T. *et al.* Long-distance electron transport in individual, living cable bacteria. *Proceedings of the National Academy of Sciences* **115**, 5786-5791 (2018).

212 Meysman, F. J. *et al.* A highly conductive fibre network enables centimetre-scale electron transport in multicellular cable bacteria. *Nature communications* **10**, 1-8 (2019).

213 Kjeldsen, K. U. *et al.* On the evolution and physiology of cable bacteria. *Proceedings of the National Academy of Sciences* **116**, 19116-19125 (2019).

214 Pfeffer, C. *et al.* Filamentous bacteria transport electrons over centimetre distances. *Nature* **491**, 218-221 (2012). https://doi.org:10.1038/nature11586

215 Myers, C. R. & Nealson, K. H. Bacterial manganese reduction and growth with manganese oxide as the sole electron acceptor. *Science* **240**, 1319-1321 (1988). https://doi.org:10.1126/science.240.4857.1319

216 Nealson, K. H., Belz, A. & McKee, B. Breathing metals as a way of life: geobiology in action. *Antonie Van Leeuwenhoek* **81**, 215-222 (2002). https://doi.org:10.1023/a:1020518818647

217 Gralnick, J. A. & Newman, D. K. Extracellular respiration. *Mol Microbiol* **65**, 1-11 (2007). https://doi.org:10.1111/j.1365-2958.2007.05778.x

218 Kowalchuk, G. A., Jones, S. E. & Blackall, L. L. Microbes orchestrate life on Earth. *ISME J* **2**, 795-796 (2008). https://doi.org:10.1038/ismej.2008.61

219 Shi, L. *et al.* Extracellular electron transfer mechanisms between microorganisms and minerals. *Nat Rev Microbiol* **14**, 651-662 (2016). https://doi.org:10.1038/nrmicro.2016.93

220 Malvankar, N. S., Tuominen, M. T. & Lovley, D. R. Lack of cytochrome involvement in long-range electron transport through conductive biofilms and nanowires of *Geobacter sulfurreducens*. *Energy & Environmental Science* **5**, 8651-8659 (2012). https://doi.org:10.1039/c2ee22330a

221 Malvankar, N. S., Tuominen, M. T. & Lovley, D. R. Comment on “On electrical conductivity of microbial nanowires and biofilms” by S. M. Strycharz-Glaven, R.

M. Snider, A. Guiseppi-Elie and L. M. Tender, Energy Environ. Sci., 2011, 4, 4366. *Energy & Environmental Science* **5**, 6247-6249 (2012). https://doi.org:10.1039/c2ee02613a

222 Strycharz-Glaven, S. M., Snider, R. M., Guiseppi-Elie, A. & Tender, L. M. On the electrical conductivity of microbial nanowires and biofilms. *Energy & Environmental Science* **4**, 4366-4379 (2011). https://doi.org:10.1039/c1ee01753e

223 Snider, R. M., Strycharz-Glaven, S. M., Tsoi, S. D., Erickson, J. S. & Tender, L. M. Long-range electron transport in Geobacter sulfurreducens biofilms is redox gradient-driven. *Proc Natl Acad Sci U S A* **109**, 15467-15472 (2012).

224 Filman, D. J. *et al.* Cryo-EM reveals the structural basis of long-range electron transport in a cytochrome-based bacterial nanowire. *Commun Biol* **2**, 219 (2019). https://doi.org:10.1038/s42003-019-0448-9

225 Lovley, D. R. & Walker, D. J. F. *Geobacter* Protein Nanowires. *Front Microbiol* **10**, 2078 (2019). https://doi.org:10.3389/fmicb.2019.02078

226 Yalcin, S. E. & Malvankar, N. S. The blind men and the filament: Understanding structures and functions of microbial nanowires. *Curr Opin Chem Biol* **59**, 193-201 (2020). https://doi.org:10.1016/j.cbpa.2020.08.004

227 Clarke, T. A. & Edwards, M. J. Uncovering nature's electronics. *Nat Chem Biol* **16**, 1041-1042 (2020). https://doi.org:10.1038/s41589-020-00655-9

228 Jiang, X. *et al.* Which Multi-Heme Protein Complex Transfers Electrons More Efficiently? Comparing MtrCAB from *Shewanella* with OmcS from *Geobacter*. *J Phys Chem Lett* **11**, 9421-9425 (2020). https://doi.org:10.1021/acs.jpclett.0c02842

229 Someya, T., Bao, Z. & Malliaras, G. G. The rise of plastic bioelectronics. *Nature* **540**, 379-385 (2016). https://doi.org:10.1038/nature21004

230 Waleed Shinwari, M., Jamal Deen, M., Starikov, E. B. & Cuniberti, G. Electrical conductance in biological molecules. *Advanced Functional Materials* **20**, 1865-1883 (2010). https://doi.org:10.1002/adfm.200902066

231 Balakrishnan, G., Hu, Y. & Spiro, T. G. His26 protonation in cytochrome c triggers microsecond β-sheet formation and heme exposure: implications for apoptosis. *Journal of the American Chemical Society* **134**, 19061-19069 (2012).

232 Wallace, C. & Clark-Lewis, I. Functional role of heme ligation in cytochrome c. Effects of replacement of methionine 80 with natural and non-natural residues by semisynthesis. *Journal of Biological Chemistry* **267**, 3852-3861 (1992).

233 Margoliash, E. & Lustgarten, J. Interconversion of horse heart cytochrome *c* monomer and polymers. *J Biol Chem* **237**, 3397-3405 (1962).

234 Hirota, S. *et al.* Cytochrome polymerization by successive domain swapping at the C-terminal helix. *Proceedings of the National Academy of Sciences* **107**, 12854 (2010).

235 Hayashi, Y. *et al.* Domain swapping oligomerization of thermostable *c*-type cytochrome in *E. coli* cells. *Sci Rep* **6**, 19334 (2016). https://doi.org:10.1038/srep19334

236 Hirota, S. Oligomerization of cytochrome *c*, myoglobin, and related heme proteins by 3D domain swapping. *J Inorg Biochem* **194**, 170-179 (2019). https://doi.org:10.1016/j.jinorgbio.2019.03.002

237 Coelho, A. V. *et al.* Desulfoferrodoxin structure determined by MAD phasing and refinement to 1.9-Å resolution reveals a unique combination of a tetrahedral FeS4 centre with a square pyramidal FeSN4 centre. *JBIC Journal of Biological Inorganic Chemistry* **2**, 680-689 (1997). https://doi.org:10.1007/s007750050184

238 Abreu, I. A. *et al.* A novel iron centre in the split-Soret cytochrome c from *Desulfovibrio desulfuricans* ATCC 27774. *J Biol Inorg Chem* **8**, 360-370 (2003). https://doi.org:10.1007/s00775-002-0426-3

239 Qian, X. *et al.* Biochemical characterization of purified OmcS, a c-type cytochrome required for insoluble Fe(III) reduction in *Geobacter sulfurreducens*. *Biochim Biophys Acta* **1807**, 404-412 (2011). https://doi.org:10.1016/j.bbabio.2011.01.003

240 Kolks, G., Frihart, C. R., Coughlin, P. K. & Lippard, S. J. Synthetic, spectroscopic, and solution studies of imidazolate-bridged dicopper(II)

complexes. *Inorganic Chemistry* **20**, 2933-2940 (1981). https://doi.org:10.1021/ic50223a037

241 Strothkamp, K. G. & Lippard, S. J. Chemistry of the imidazolate-bridged bimetallic center in the copper-zinc superoxide dismutase and its model compounds. *Accounts of Chemical Research* **15**, 318-326 (1982). https://doi.org:10.1021/ar00082a004

242 Ikezaki, A. & Nakamura, M. Models for cytochromes c': spin states of mono(imidazole)-ligated (meso-tetramesitylporphyrinato)iron(III) complexes as studied by UV-Vis, 13C NMR, 1H NMR, and EPR spectroscopy. *Inorg Chem* **41**, 6225-6236 (2002). https://doi.org:10.1021/ic020378t

243 Gu, Y. *et al.* Structure of *Geobacter* pili reveals secretory rather than nanowire behaviour. *Nature*, In press (2021).

244 Liu, X. *et al.* Power generation from ambient humidity using protein nanowires. *Nature* **578**, 550-554 (2020). https://doi.org:10.1038/s41586-020-2010-9

245 Lovley, D. R. & Holmes, D. E. Protein Nanowires: the Electrification of the Microbial World and Maybe Our Own. *J Bacteriol* **202**, e00331-00320 (2020). https://doi.org:10.1128/JB.00331-20

246 Liu, X., Walker, D. J. F., Nonnenmann, S. S., Sun, D. & Lovley, D. R. Direct Observation of Electrically Conductive Pili Emanating from *Geobacter sulfurreducens*. *mBio* **12**, e0220921 (2021). https://doi.org:10.1128/mBio.02209-21

247 Sun, Y. L. *et al.* Solvent-Induced Assembly of Microbial Protein Nanowires into Superstructured Bundles. *Biomacromolecules* **22**, 1305-1311 (2021). https://doi.org:10.1021/acs.biomac.0c01790

248 Liu, Y., Fredrickson, J. K., Zachara, J. M. & Shi, L. Direct involvement of ombB, omaB, and omcB genes in extracellular reduction of Fe(III) by Geobacter sulfurreducens PCA. *Front Microbiol* **6**, 1075 (2015). https://doi.org:10.3389/fmicb.2015.01075

249 Shrestha, P. M. *et al.* Transcriptomic and genetic analysis of direct interspecies electron transfer. *Appl Environ Microbiol* **79**, 2397-2404 (2013). https://doi.org:10.1128/AEM.03837-12

250 Lovley, D. R., Phillips, E.J.P. Organic Matter Mineralization with Reduction of Ferric Iron in Anaerobic Seidments *Appl Environ Microbiol* (1986).

251 Ueki, T., DiDonato, L. N. & Lovley, D. R. Toward establishing minimum requirements for extracellular electron transfer in Geobacter sulfurreducens. *FEMS Microbiol Lett* **364** (2017). https://doi.org:10.1093/femsle/fnx093